CALIFORNIA INSTITUTE OF TECHNOLOGY

EARTHQUAKE ENGINEERING RESEARCH LABORATORY

TWO-STEP BAYESIAN STRUCTURAL HEALTH MONITORING APPROACH FOR IASC-ASCE PHASE II SIMULATED AND EXPERIMENTAL BENCHMARK STUDIES

by

JIANYE CHING AND JAMES L. BECK

Report No. EERL 2003-02

A Report on Research Supported by
California Institute of Technology

Pasadena, California

FEBRUARY 2003

ACKNOWLEDGEMENTS

The authors wish to acknowledge the efforts of the IASC-ASCE Task Group on Structural Health Monitoring in establishing the benchmarks studied in this report; in particular, members Dennis Bernal (Northeastern University), Shirley Dyke (Washington University in St. Louis), Carlos Ventura (University of British Columbia), along with some graduate students and the second author, performed the experiments on the UBC test structure that constitute the Phase II experimental benchmark. Also, the ASCE Engineering Mechanics Division provided partial travel support for the meetings of the Task Group and this support is gratefully acknowledged. J. Ching wishes to acknowledge the financial support of the George W. Housner Postdoctoral Fellowship from the California Institute of Technology.

ABSTRACT

This report uses a two-step probabilistic structural health monitoring approach to analyze the Phase II simulated and experimental benchmark studies sponsored by the IASC-ASCE Task Group on Structural Health Monitoring. The studies involve damage detection and assessment of the test structure using simulated ambient-vibration data and experimental data generated by various excitations. The two-step approach involves modal identification followed by damage assessment using the pre- and post-damage modal parameters based on the Bayesian updating methodology. An Expectation-Maximization algorithm is proposed to find the most probable values of the parameters. The results of the analysis show that the probabilistic approach is able to detect and assess most damage locations involving stiffness losses of braces in the braced frame cases, while the success of the approach in detecting rotational stiffness losses of the beam-column connections in the unbraced cases may rely on sufficient prior information for the column stiffness.

TABLE OF CONTENTS

1 Introduction

Structural health monitoring (SHM) techniques [1-6] are methodologies that detect and locate damage in structures and quantitatively assess its severity via measured responses. In recent years, civil engineers have paid much attention to SHM techniques since they have the potential to monitor the safety of civil infrastructures. The basic idea is to detect and assess damage by comparing the response of the structure under investigation before and after possible damage, e.g. earthquake damage or long-term deterioration.

Numerous SHM techniques have been developed, but there is a difficulty of comparing the merits of different techniques. In view of this situation, a series of benchmark studies were sponsored by the IASC (International Association for Structural Control) – ASCE Task Group on Structural Health Monitoring, beginning with a relatively simple benchmark problem and proceeding on to more realistic problems, to provide a common basis for comparison of different techniques [7].

The benchmark studies currently consist of two simulated and two experimental benchmark problems. The benchmark structure is a 4-story, 2-bay by 2-bay steel-frame scale-model structure (Figure 1) built in the Earthquake Engineering Research Laboratory at the University of British Columbia, Canada. A diagram for the analytical model for the benchmark structure is shown in Figure 2, in which x-direction is the strong direction of the columns. Phase I of the simulated benchmark studies [8] has been completed, and several conference sessions, e.g. 14th ASCE Engineering Mechanics Specialty Conference in 2000, ASME-ASCE Joint Mechanics and Materials Conference in 2001, 3rd International Workshop on Structural Health Monitoring in 2001, were held for the discussions of the results. Phase I of the experimental benchmark [9] was performed on July 19-21, 2000 by some members of the IASC-ASCE Task Group.

This report focuses on Phase II of the simulated and experimental benchmark studies (we will call them simulated and experimental Phase II, respectively). Simulated Phase II is defined in Bernal et al [10]. These case studies involve detection and assessment of damage with different severities and at different locations. Compared to simulated Phase I, simulated Phase II is more realistic and difficult in the following aspects: 1) There is more modeling error because in simulated Phase II the structural parameter values are randomly chosen in the benchmark structural model. 2) Unlike simulated Phase I which has major damage, e.g. complete loss of stiffness of one or more braces, simulated Phase II considers moderate damage, e.g. partial stiffness reduction in a brace. 3) Loss of rotational stiffness of the beam-column connections is considered in simulated Phase II.

Due to some issues with the data for experimental Phase I, experimental Phase II was performed on Aug 4-7, 2002 to gather higher quality and more extensive data. Various damage configurations were investigated by removing bracing and loosening beam-column connections within the test structure. In addition, asymmetrical floor mass was considered in experimental Phase II.

1.1 Simulated Phase II Benchmark

Simulated Phase II Benchmark consists of two reference cases, braced (RB) and unbraced (RU) cases. For the braced structure, only brace damage is studied while for the unbraced structure, loss of rotational stiffness of the beam-column connections is considered. In the benchmark structural model used to generate the simulated data, mass and brace stiffness uncertainties are modeled by randomly selecting all floor mass from a uniform distribution over [0.9 1.1] of the nominal value; the center of the floor mass deviates from the geometrical floor center by randomly selecting a factor from a uniform distribution over [-0.05 0.05] of the floor width;

and the brace stiffnesses are randomized uniformly over [0.95 1.05] of the nominal value. We denote a structural member using its type: 'br', 'bm', and 'cl' stand for brace, beam, and column, respectively and the node numbers of its two ends, e.g. $br_{1\text{-}11}$ is the brace whose two ends are nodes 1 and 11 in Figure 2.

Four damage cases are considered for the braced structure: 1) DP1B: 50% stiffness reduction in $br_{1\text{-}11}$ and $br_{7\text{-}17}$ (the dashed lines in Figure 3a indicate the corresponding damaged locations). 2) DP2B: 25% stiffness reduction in $br_{1\text{-}11}$ and $br_{7\text{-}17}$. 3) DP3B: same as DP1B, but in addition 25% stiffness reduction in $br_{19\text{-}29}$ and $br_{25\text{-}35}$ (dashed lines in Figure 3b). 4) DP3Bu: 50% and 25% stiffness reduction in $br_{1\text{-}11}$ and $br_{19\text{-}29}$ (dashed lines in Figure 3c). Thus, the damage cases DP1B, DP2B, and DP3B are symmetric and DP3Bu is an asymmetric case.

For the unbraced cases, in addition to the mass and mass center uncertainties, rotational stiffness uncertainties are considered in such a way that the rotational stiffness of the beam-column connections is randomized uniformly over [0.75 1.25] of the nominal value. Three damage cases are considered for the unbraced case: 1) DP1U: Loss of rotational stiffness at both ends of $bm_{11\text{-}12}$, $bm_{20\text{-}21}$, $bm_{17\text{-}18}$, $bm_{26\text{-}27}$ and the right ends of $bm_{10\text{-}11}$ and $bm_{16\text{-}17}$ (the circles in Figure 4a indicate the loosened connections). 2) DP2U: Loss of rotational stiffness at both ends of $bm_{11\text{-}12}$ and $bm_{17\text{-}18}$ (the circles in Figure 4b). 3) DP1Uu: Loss of rotational stiffness at both ends of $bm_{11\text{-}12}$, $bm_{20\text{-}21}$ and the right end of $bm_{10\text{-}11}$ (the circles in Figure 4c). The damage cases DP1U and DP2U are symmetric, while DP1Uu is asymmetric.

Simulated Phase II also contains two blind tests (Blind1 and Blind2). It is given that the two damage cases have no beam-column connection failure but only brace damage, and there is only one brace that is damaged for Blind1 [7].

The simulated data for all cases is generated by broadband ambient-vibration excitation of the HKUST 120-DOF model [10] at each floor that is unknown to the investigator. The 120-DOF model is a reduced-order version of a 216-DOF model with the constraint that the floors are rigid in translation along the x- and y-axes and rotation along the z-axis. Two instrumentation scenarios, the full-sensor and partial-sensor scenarios, are considered. For the full-sensor scenario, four sensor measurements are available at the center of each side at each floor (e.g. nodes 11, 13, 15, and 17 at the second floor) with the directions parallel to the side in either the positive x- or y-direction, as indicated in Figure 2. For the partial-sensor scenario, only measurements at the third floor and the roof are available.

1.2 Experimental Phase II Benchmark

Experimental Phase II Benchmark consists of nine configurations, in which Configs 1-6 are braced cases with Config 1 the reference (undamaged) case, and Configs 7-9 are unbraced cases with Config 7 the reference case. For the braced cases, loss of rotational stiffness of the beam-column connections is not considered. In all configurations, the centers of the floor mass deviate slightly from the floor centers to simulate typical situations in real buildings. Five damage cases are considered for the braced structure: 1) Config 2: removal of all braces on the –y face (the face whose outward normal is the –y direction; the dashed lines in Figure 5a indicate the removed braces). 2) Config 3: removal of the left-hand-side brace in each story on the –y face (the dashed lines in Figure 5b). 3) Config 4: removal of the left-hand-side brace in the first and fourth stories on the –y face (the dashed lines in Figure 5c). 4) Config 5: removal of the left-hand-side brace in the first story on the –y face (the dashed lines in Figure 5d). 5) Config 6: removal of two braces in the second story on the +x face (the dashed lines in Figure 5e). Two damage cases are considered for the unbraced case: 1) Config 8: loosen both ends of the right-hand-

side beam at each floor on the –y face (the circles in Figure 6a indicate the loosened connections). 2) Config 9: loosen both ends of the right-hand-side beam at the first and second floors on the –y face (the circles in Figure 6b).

For each configuration, experimental data was generated by three types of excitation: 1) Impacts of a sledge hammer: For each configuration, the structure was hit three times in each direction by the hammer at a location corresponding to node 10 (Figure 2); 2) Ambient vibration: The duration of the recorded data was 300s for each configuration. 3) Electrodynamic shaker: The shaker was placed roughly at the center of one of the four bays on the roof. The shaker force input excited the benchmark structure for 120s for each configuration. A mass was attached to the end of the shaker to increase the vibration input. The direction of the shaker force was perpendicular to a diagonal line of the roof. Two types of shaker force, random and sinusoidal sweep input, were used.

Two sensor systems were mounted on the structure: Kinemetrics EPI and FBA force-balance accelerometers. All sensors were clamped to the steel masses or structural members that they were mounted on. Five EPI sensors were mounted near the base and floor centers (nodes 5, 14, 23, 32, and 41 in Figure 2) to measure the accelerations in the +y direction, and ten FBA sensors were mounted near nodes 2, 8, 11, 17, 20, 26, 29, 35, 38, and 44 in Figure 2 to measure the accelerations in the +x direction. Additionally, for the loosened beam tests (Configs 7-9), some of the sensors were moved to nearby locations so that they were not resting on a loose beam.

Results using a two-step probabilistic SHM approach [4,11] are presented: the modal parameters and their uncertainties are identified in the first step and are then used in a subsequent step to determine the probability that stiffness reductions exceed a prescribed damage threshold. This approach was also used to analyze simulated Phase I [12] but in this work a more reliable

Bayesian updating algorithm (Expectation-Maximization) is proposed to find the most probable values of the model parameters.

2 Model updating methodology

The primary purpose of the model updating methodology is to update the probability density function (PDF) of stiffness parameters of the identification model based on measured data from the undamaged and potentially damaged structure. The detection of damage is based on the probability that each substructure stiffness parameter has a fractional decrease of more than d from the undamaged to the potentially damaged structure, where the damage severity d is specified. The methodology consists of two steps where the first step involves identification of modal parameters and the associated uncertainties based on measured time-domain data, and the second step utilizes the outcome from the first step to compute the updated PDF of the stiffness parameters.

2.1 Modal parameter identification

In the first step of the damage detection procedure, 'experimental modal parameters' are extracted from the time-domain measured data using the modal identification procedure called MODE-ID [13,14]. It is a nonlinear least-squares method based on a linear dynamical model with classical normal modes of vibration.

In the case of known excitation forces, MODE-ID estimates modal parameters of the structure by minimizing the Euclidean norm of the difference between the measured response of the structure and the model output at the measured degrees of freedom (DOF). The identified modal parameters are modal frequencies, damping ratios, participation factors, and modeshape components at the measured DOF for N_m dominant modes of vibration. The identified modal parameters are then used for damage detection in the second step.

In the case of ambient-vibration input, extracting modal parameters is a challenging task because of the poor signal-to-noise ratio and the fact that the excitation forces are not known. In the approach used here [14], the excitation and structural responses are modeled as weakly stationary stochastic processes where the current excitation is assumed to be uncorrelated from the past response. It can be shown that the cross-correlation function matrix $R_x(\tau)$ of the model responses satisfy the original equation of motion for the structure in free vibration where the time lag serves as a pseudo-time [14]:

$$M\ddot{R}_x(\tau) + C\dot{R}_x(\tau) + KR_x(\tau) = 0\,, \tag{1}$$

where

$$R_x(\tau) = E[x(t)x^T(t-\tau)]\,. \tag{2}$$

Here the derivatives are with respect to the time lag τ. Each column vector of the cross-correlation function matrix $R_x(\tau)$ is a free-vibration solution of the structure. Thus, modal identification is carried out by using the cross-correlation functions as free-vibration responses for MODE-ID. The identified modal parameters are the modal frequencies, damping ratios, and modeshape components at the measured DOF for N_m dominant modes of vibration.

The measured time histories of the structural response are partitioned temporally into N_s time segments, which are analyzed individually by the modal identification procedure to yield N_s sets of the modal parameters for the N_m modes. The identified modal parameters are then used for damage detection in the second step.

2.2 Damage detection and assessment

In the Bayesian framework, both mass and stiffness matrices are updated. A prior PDF is specified for the mass and stiffness parameters to reflect the relative plausibilities of their values in the absence of any measurement data. A general Bayesian statistical approach is employed to

construct an updated PDF for the parameters using the prior PDF and the experimental modal parameters [15].

To define the identification model class $\boldsymbol{M}$, we first choose a set of linear structural models with the mass matrix *M* and stiffness matrix *K* parameterized in an affine manner as follows:

$$M(\rho) = M_0 + \sum_{i=1}^{N_M} \rho_i M_i \qquad K(\theta) = K_0 + \sum_{i=1}^{N_K} \theta_i K_i \,, \tag{3}$$

where $M_i \in R^{N_d \times N_d}$ and $K_i \in R^{N_d \times N_d}$ (N_d is the number of DOF of the identification model) are prescribed nominal contributions of the i-th substructure to the global mass and stiffness matrices, and the uncertain parameters ρ_i and θ_i scale these contributions. We assume classical normal modes and thus the damping matrix *C* is not explicitly used.

2.2.1 Partial modeshape information

In the situation that the full DOF of the identification model are not measured, 'system modeshapes' [11,16] may be introduced and the connection between the experimental modal parameters from the first step and the model parameters becomes:

$$\hat{\omega}_{r,j}^2 = \tilde{\omega}_r^2 + \varepsilon_{r,j} \qquad \hat{\psi}_{r,j} = a_r \Gamma \phi_r + e_{r,j}, \tag{4}$$

where $\hat{\omega}_{r,j}$ and $\hat{\psi}_{r,j} \in R^{N_o}$ are the experimental modal frequency and modeshapes of the r-th mode from the j-th data segment ($r = 1...N_m$, $j = 1...N_s$), N_o is the number of measured DOF, $\phi_r \in R^{N_d}$ is the system modeshape of the r-th mode, Γ is the matrix that picks the measured DOF from the system modeshape ϕ_r, a_r is a scaling parameter [11,16] and

$$\tilde{\omega}_r^2 = \phi_r^T K(\theta) \phi_r \big/ \phi_r^T M(\rho) \phi_r \,. \tag{5}$$

In the partial-modeshape case, the modeshapes are normalized so that their Euclidean norm $\left\| \hat{\psi}_{r,j} \right\|^2 = 1$. We denote the set of experimental modal frequencies by

$\hat{\omega} = \{\hat{\omega}_{r,j}, r = 1...N_m, j = 1...N_s\}$, the set of experimental modeshape components at the measured DOF by $\hat{\psi} = \{\hat{\psi}_{r,j}, r = 1...N_m, j = 1...N_s\}$ and the system modeshapes by $\phi = \{\phi_r, r = 1...N_m\}$ to facilitate future discussion. For conciseness, the symbol $\boldsymbol{M}$ will be omitted in all derivations although all the PDFs are obviously conditional on the choice of $\boldsymbol{M}$.

The system modeshapes ϕ can be regarded as a bridge connecting the identification problem with full modeshape information to the one with partial modeshape information. There are, however, several other advantages to expanding the identification model class $\boldsymbol{M}$ by introducing the system modeshapes: 1) Because of the constraints of the assumed mathematical structure built into $\boldsymbol{M}$, it might not be possible for any structural model in this class to produce theoretical modeshapes that will give a good match of the experimental modeshapes. The system modeshapes provide extra flexibility in this aspect. 2) Their introduction also turns out to remove any need to match system and model modes during the identification, thereby avoiding a common difficulty in applications. 3) Finally, we will show that it is computationally beneficial to expand the model class $\boldsymbol{M}$ by using the system modeshapes.

The PDF of the two uncertainty terms in (4) are assumed to be independent Gaussian justified by the maximum differential entropy principle [17]:

$$\varepsilon_{r,j} \sim N(0, \sigma_r^2) \qquad e_{r,j} \sim N(\underline{0}, \delta_r^2 \cdot I), \tag{6}$$

The prior PDF of ρ, θ and $\{\phi_r : r = 1...N_m\}$ is also assumed to be independent Gaussian with

$$\phi_r \sim N(\phi_r^0, Q_r) \qquad \rho \sim N(\rho^0, P_\rho^0) \qquad \theta \sim N(\theta^0, P_\theta^0) \tag{7}$$

subject to affine constraints $A_\rho \rho + A_\theta \theta < b$, and we have assumed that the variances of the prior PDFs of ϕ_r, σ_r^2, δ_r^2 and a_r are so large that the PDFs are essentially flat over the range of interest. It was reported in [12] that explicitly treating the uncertainties in the mass parameters ρ

makes the identification more robust. However, to avoid making the identification problem ill-posed when simultaneously treating ρ and θ as uncertain variables, we assume the variances of the prior PDF of ρ are small.

The full set of model parameters is $\lambda = \{\rho, \theta, \phi_r, a_r, \sigma_r^2, \delta_r^2 : r = 1...N_m\}$. The updated PDF of λ, i.e. $p(\lambda \mid \hat{\omega}, \hat{\psi})$, is of central concern in the Bayesian framework; in particular, the most probable values (MPV) of the parameters based on the modal data are given by maximizing $p(\lambda \mid \hat{\omega}, \hat{\psi})$. For this optimization problem, it is more convenient to work with the logarithm of $p(\lambda \mid \hat{\omega}, \hat{\psi})$, which is

$$
\begin{aligned}
&\log p(\lambda \mid \hat{\omega}, \hat{\psi}) \\
&= -(1/2)\sum_{r=1}^{N_m}\sum_{j=1}^{N_s}\left[\left\{\log(\sigma_r^2) + (\hat{\omega}_{r,j}^2 - \tilde{\omega}_r^2)^2 / \sigma_r^2\right\} + \left\{N_o \log(\delta_r^2) + \left\|\hat{\psi}_{r,j} - a_r \Gamma \phi_r\right\|^2 / \delta_r^2\right\}\right] \\
&\quad - (1/2)\left\{\log[\det(P_\rho^0)] + (\rho - \rho^0)^T (P_\rho^0)^{-1}(\rho - \rho^0)\right\} \\
&\quad - (1/2)\left\{\log[\det(P_\theta^0)] + (\theta - \theta^0)^T (P_\theta^0)^{-1}(\theta - \theta^0)\right\} + c\,, \qquad (8)
\end{aligned}
$$

where *c* is a constant. Note that if we impose the normalization condition $\phi_r^T M \phi_r = 1$, we have

$$
\begin{aligned}
&(\hat{\omega}_{r,j}^2 - \tilde{\omega}_r^2)^2 = (\hat{\omega}_{r,j}^2)^2 - 2\hat{\omega}_{r,j}^2 \tilde{\omega}_r^2 + (\tilde{\omega}_r^2)^2 \\
&= \frac{[\phi_r^T K M^{-1} K \phi_r + (\hat{\omega}_{r,j}^2)^2 \phi_r^T M \phi_r - 2 \cdot \hat{\omega}_{r,j}^2 \phi_r^T K \phi_r] - [\phi_r^T K M^{-1} K \phi_r + (\tilde{\omega}_r^2)^2 \phi_r^T M \phi_r - 2 \cdot \tilde{\omega}_r^2 \phi_r^T K \phi_r]}{\phi_r^T M \phi_r} \\
&= [(K - \hat{\omega}_{r,j}^2 M)\phi_r]^T M^{-1} [(K - \hat{\omega}_{r,j}^2 M)\phi_r] - [(K - \tilde{\omega}_r^2 M)\phi_r]^T M^{-1} [(K - \tilde{\omega}_r^2 M)\phi_r] \\
&= \left\|(K - \hat{\omega}_{r,j}^2 M)\phi_r\right\|_{M^{-1}}^2 - \left\|(K - \tilde{\omega}_r^2 M)\phi_r\right\|_{M^{-1}}^2 . \qquad (9)
\end{aligned}
$$

Among the terms in (9), $\left\|(K - \tilde{\omega}_r^2 M)\phi_r\right\|_{M^{-1}}^2$ is significantly less than $\left\|(K - \hat{\omega}_{r,j}^2 M)\phi_r\right\|_{M^{-1}}^2$ if ϕ_r is close to a theoretical modeshape ϕ_r^{Th} of the structural model. Indeed, if ϕ_r is equal to ϕ_r^{Th}, $\tilde{\omega}_r$ will be simply the theoretical modal frequency; therefore $\left\|(K - \tilde{\omega}_r^2 M)\phi_r\right\|_{M^{-1}}^2$ vanishes. Furthermore, if ϕ_r is close to ϕ_r^{Th} with a small perturbation $\delta\phi_r$,

$$\left\|(K-\tilde{\omega}_r^2 M)\phi_r\right\|_{M^{-1}}\Big|_{\phi_r=\phi_r^{Th}+\delta\phi_r} = \left\|(K-\tilde{\omega}_r^2 M)\phi_r\right\|_{M^{-1}}\Big|_{\phi_r=\phi_r^{Th}} + \nabla_{\phi_r}\left\|(K-\tilde{\omega}_r^2 M)\phi_r\right\|_{M^{-1}}\Big|_{\phi_r=\phi_r^{Th}}\cdot\delta\phi_r$$
$$+1/2\cdot\delta\phi_r^T\cdot\nabla_{\phi_r}^2\left\|(K-\tilde{\omega}_r^2 M)\phi_r\right\|_{M^{-1}}\Big|_{\phi_r=\phi_r^{Th}}\cdot\delta\phi_r + O(\left\|\delta\phi_r\right\|^3). \quad (10)$$

Since we know that

$$\left\|(K-\tilde{\omega}_r^2 M)\phi_r\right\|_{M^{-1}}\Big|_{\phi_r=\phi_r^{Th}} = 0 \quad (11)$$

and that

$$\nabla_{\phi_r}\left\|(K-\tilde{\omega}_r^2 M)\phi_r\right\|_{M^{-1}}\Big|_{\phi_r=\phi_r^{Th}}\cdot\delta\phi_r = 0, \quad (12)$$

i.e. $\left\|(K-\tilde{\omega}_r^2 M)\phi_r\right\|_{M^{-1}}$ is stationary with respect to ϕ_r at ϕ_r^{Th}, we conclude that $\left\|(K-\tilde{\omega}_r^2 M)\phi_r\right\|_{M^{-1}}^2$ is at the order of $O(\left\|\delta\phi_r\right\|^4)$. However, $\left\|(K-\hat{\omega}_{r,j}^2 M)\phi_r\right\|_{M^{-1}}^2$ does not have these properties and so is not small. Therefore, in the case that ϕ_r is close to ϕ_r^{Th}, we approximate (8) using (9) with the second term neglected, so that

$$\begin{aligned}&\log p(\lambda\,|\,\hat{\omega},\hat{\psi})\\ &= -(1/2)\sum_{r=1}^{N_m}\sum_{j=1}^{N_s}\left[\left\{\log(\sigma_r^2)+\left\|[K-\hat{\omega}_{r,j}^2 M]\phi_r\right\|_{M^{-1}}^2/\sigma_r^2\right\}+\left\{N_o\log(\delta_r^2)+\left\|\hat{\psi}_{r,j}-a_r\Gamma\phi_r\right\|^2/\delta_r^2\right\}\right]\\ &\quad-(1/2)\left\{\log[\det(P_\rho^0)]+(\rho-\rho^0)^T(P_\rho^0)^{-1}(\rho-\rho^0)\right\}\\ &\quad-(1/2)\left\{\log[\det(P_\theta^0)]+(\theta-\theta^0)^T(P_\theta^0)^{-1}(\theta-\theta^0)\right\}+c, \end{aligned}\quad (13)$$

The advantage of converting (8) to (13) is that $\log p(\lambda\,|\,\hat{\omega},\hat{\psi})$ is not quadratic in ϕ in (8), but it is quadratic in ϕ in (13). Being quadratic in ϕ has certain computational benefits.

The optimization problem associated with (13) generally has more than one local maximum since $\log p(\lambda\,|\,\hat{\omega},\hat{\psi})$ is not a concave function of λ. Also, $\log p(\lambda\,|\,\hat{\omega},\hat{\psi})$ does not fall into certain functional forms that are easy to optimize, e.g. linear or quadratic functions. Such a problem is usually handled using a generic local search optimization algorithm based on Newton's or

descent methods. However, due to the high dimensionality of λ, the use of such local search methods, which often require evaluation of gradients or Hessians with respect to λ, is prohibitive. Notice that given $\{\rho, \theta, a_r, \sigma_r^2, \delta_r^2 : r = 1...N_m\}$, $\log p(\lambda \mid \hat{\omega}, \hat{\psi})$ is concave in ϕ. Also, given ϕ and ρ (and so the mass matrix *M*), and that the system is locally identifiable based on the modal data [15], finding the MPV of $\{\theta, a_r, \sigma_r^2, \delta_r^2 : r = 1...N_m\}$ is equivalent to estimating the mean and covariance matrix of a Gaussian PDF based on sampled data, which is a well-known concave optimization problem with a unique local maximum. Moreover, given ϕ, $\log p(\lambda \mid \hat{\omega}, \hat{\psi})$ (Equation 13) is quadratic in θ and roughly quadratic in ρ (this is because the prior PDF of ρ has small variances). Later, we will show that it is possible to transform the optimization problem into two coupled concave programming problems using the Expectation-Maximization (EM) algorithm. The detailed derivations for the partial modeshape information case will be pursued in a later section together with the EM algorithm.

If the identification model is globally identifiable [15], the updated PDF $p(\lambda \mid \hat{\omega}, \hat{\psi})$ can be asymptotically approximated by a multi-dimensional Gaussian PDF with mean equal to the most probable value (MPV) of λ, where

$$\hat{\lambda} = \arg\max_{\lambda} \log p(\lambda \mid \hat{\omega}, \hat{\psi}) \tag{14}$$

subject to affine constraints $A_\rho \rho + A_\theta \theta \le b$, and the covariance matrix equal to the negative of the inverse of the Hessian matrix $H(\hat{\lambda} \mid \hat{\omega}, \hat{\psi})$, where

$$H(\lambda \mid \hat{\omega}, \hat{\psi}) = \nabla_\lambda \nabla_\lambda \log p(\lambda \mid \hat{\omega}, \hat{\psi}). \tag{15}$$

Strictly speaking, the Hessian matrix can be evaluated only if the MPV is not on the hyperplane $A_\rho \rho + A_\theta \theta = b$, i.e. the affine constraints $A_\rho \rho + A_\theta \theta \le b$ are not active. However, we use (15)

to calculate the Hessian matrix even if the affine constraints $A_\rho \rho + A_\theta \theta \le b$ are active, and in this situation, we over-estimate the uncertainties associated with the MPV.

2.2.2 Full modeshape information

In the case that all DOF of the identification model are measured, the following equation may be used to connect the experimental modal parameters with *M(ρ)* and *K(θ)*

$$\hat{\omega}_{r,j}^2 = \hat{\psi}_{r,j}^T K(\theta)\hat{\psi}_{r,j} \big/ \hat{\psi}_{r,j}^T M(\rho)\hat{\psi}_{r,j} + \varepsilon_{r,j}, \tag{16}$$

where $\hat{\psi}_{r,j} \in R^{N_d}$. The uncertainty in the prediction error in (16) is modeled by independent Gaussian PDFs:

$$\varepsilon_{r,j} \sim N(0, \sigma_r^2). \tag{17}$$

The prior PDF of ρ and θ are also assumed to be independent Gaussian subject to affine inequality constraints:

$$\rho \sim N(\rho^0, P_\rho^0) \qquad \theta \sim N(\theta^0, P_\theta^0) \qquad A_\rho \rho + A_\theta \theta \le b, \tag{18}$$

and we also assumed that the variance of the prior PDF of σ_r^2 is so large that the PDF is essentially flat over the range of interest. The variances of the prior PDF of ρ are assumed to be small in order to have the problem well-posed.

The full set of model parameters is $\lambda = \{\rho, \theta, \sigma_r^2 : r = 1...N_m\}$. Using Bayes' rule, we have

$$\begin{aligned}
&\log p(\lambda \mid \hat{\omega}, \hat{\psi}) \\
&= -(1/2)\sum_{r=1}^{N_m}\sum_{j=1}^{N_s}\left\{\log(\sigma_r^2) + [\hat{\psi}_{r,j}^T K \hat{\psi}_{r,j} - \hat{\omega}_{r,j}^2 \cdot \hat{\psi}_{r,j}^T M \hat{\psi}_{r,j}]^2 \big/ [\sigma_r^2 \left\|\hat{\psi}_{r,j}\right\|_M^2]\right\} \\
&\quad -(1/2)\left\{\log[\det(P_\rho^0)] + (\rho - \rho^0)^T (P_\rho^0)^{-1}(\rho - \rho^0)\right\} \\
&\quad -(1/2)\left\{\log[\det(P_\theta^0)] + (\theta - \theta^0)^T (P_\theta^0)^{-1}(\theta - \theta^0)\right\} + c,
\end{aligned} \tag{19}$$

where c is a constant. If we normalize the modeshape estimates $\hat{\psi}_{r,j}$ such that $\left\|\hat{\psi}_{r,j}\right\|_M^2 = 1$, we get

$$\begin{aligned}
&\log p(\lambda \mid \hat{\omega}, \hat{\psi}) \\
&= -(1/2)\sum_{r=1}^{N_m}\sum_{j=1}^{N_s}\left\{\log(\sigma_r^2) + [\hat{\psi}_{r,j}^T K(\theta)\hat{\psi}_{r,j} - \hat{\omega}_{r,j}^2 \cdot \hat{\psi}_{r,j}^T M(\rho)\hat{\psi}_{r,j}]^2 \big/ \sigma_r^2\right\} \\
&\quad -(1/2)\left\{\log[\det(P_\rho^0)] + (\rho-\rho^0)^T (P_\rho^0)^{-1}(\rho-\rho^0)\right\} \\
&\quad -(1/2)\left\{\log[\det(P_\theta^0)] + (\theta-\theta^0)^T (P_\theta^0)^{-1}(\theta-\theta^0)\right\} + c\,, \qquad (20)
\end{aligned}$$

which is quadratic with respect to ρ and θ. If the system is locally identifiable, finding the MPV $\hat{\lambda}$ is equivalent to estimating the mean and covariance matrix of a Gaussian PDF based on sampled data, which is a well-known concave optimization problem. Therefore, $\hat{\lambda}$ can be uniquely determined using any local search optimization algorithm. We maximize $\log p(\lambda \mid \hat{\omega}, \hat{\psi})$ using two iterative steps: first with respect to σ_r^2 with (ρ, θ) fixed in order to deduce the conditional optimal value $\tilde{\sigma}_r^2$, and then with respect to (ρ, θ) with $\tilde{\sigma}_r^2$ substituted into (20). The first maximization gives

$$\tilde{\sigma}_r^2 = (1/N_s)\sum_{j=1}^{N_s}\left\{[\hat{\psi}_{r,j}^T K(\theta)\hat{\psi}_{r,j} - \hat{\omega}_{r,j}^2 \cdot \hat{\psi}_{r,j}^T M(\rho)\hat{\psi}_{r,j}]^2\right\}, \qquad (21)$$

and the second one can be solved by a standard quadratic programming algorithm subject to $A_\rho \rho + A_\theta \theta \le b$. The iteration stops when satisfactory convergence is achieved with global maximization guaranteed. The covariance matrix of $\hat{\lambda}$ is equal to the negative of the inverse of the Hessian matrix $H(\hat{\lambda} \mid \hat{\omega}, \hat{\psi})$ given in (15).

For both the full and partial modeshape situations, the marginal updated PDF of θ, $p(\theta \mid \hat{\omega}, \hat{\psi})$, obtained by integrating the joint updated PDF to remove the other parameters in λ, can be used to find the probability that the i-th substructure stiffness parameter has been reduced by more than a specified fraction d_i of the stiffness in the initial undamaged state of the structure.

By using the Gaussian asymptotic approximation (see [14] and [15]) and assuming the stiffness parameters for the undamaged state and possibly damage state are conditionally independent [4], we get:

$$P_i(d_i) = P\{\theta_i^{pd} < (1-d_i)\theta_i^{ud} \mid \hat{\omega}^{pd}, \hat{\psi}^{pd}, \hat{\omega}^{ud}, \hat{\psi}^{ud}\} \approx \Phi\left(\frac{(1-d_i)\hat{\theta}_i^{ud} - \hat{\theta}_i^{pd}}{\sqrt{(1-d_i^2)(\hat{\sigma}_i^{ud})^2 + (\hat{\sigma}_i^{pd})^2}}\right), \qquad (22)$$

where $\Phi(\cdot)$ is the standard Gaussian cumulative distribution function, $\hat{\theta}_i^{ud}$ and $\hat{\theta}_i^{pd}$ denote the MPV of the stiffness parameters for an undamaged and possibly damaged structure, respectively, and $\hat{\sigma}_i^{ud}$ and $\hat{\sigma}_i^{pd}$ are the corresponding standard deviations from the covariance matrix derived from the Hessian matrix in (15).

3 Computational aspects for partial modeshape information

In the case of partial modeshape information, finding the MPV is a difficult task for the following two reasons: 1) The objective function $\log p(\lambda \mid \hat{\omega}, \hat{\psi})$ is not concave in λ. Therefore, there may be more than one local maximum; 2) For the same reason, if a nonlinear programming optimization algorithm is employed to find a local maximum, there may be convergence difficulties because of parameter interactions among the large number of unknowns.

It is true, however, that given $\xi \equiv \{\rho, \theta, a_r, \sigma_r^2, \delta_r^2 : r = 1...N_m\}$, $\log p(\lambda \mid \hat{\omega}, \hat{\psi})$ is concave in ϕ; and given ϕ, $\log p(\lambda \mid \hat{\omega}, \hat{\psi})$ is concave in ξ, although $\log p(\lambda \mid \hat{\omega}, \hat{\psi})$ is not concave in λ. This suggests a strategy to maximize the objective function with respect to ϕ and ξ until satisfactory convergence is achieved. In this way, we decompose the non-concave optimization problem into two coupled concave and quasi-quadratic optimization problems. This strategy solves the second difficulty listed above since the solutions of the two quadratic programming problems

can be computed analytically and rapidly. Moreover, this strategy is, in fact, closely related to the Expectation-Maximization (EM) algorithm [18].

The EM algorithm deals with the problem of probabilistic inference and parameter estimation when some uncertain variables are not observed. In the partial modeshape case, the unobserved variable is the system modeshape ϕ, while the parameters we intend to estimate are ξ based on the observed $\hat{\omega}$ and $\hat{\psi}$, so we require

$$\hat{\xi} = \arg\max_{\xi} \log p(\xi \mid \hat{\omega}, \hat{\psi}) \tag{23}$$

subject to $A_\rho \rho + A_\theta \theta < b$, where

$$\begin{aligned} &\log p(\xi \mid \hat{\omega}, \hat{\psi}) \\ &= \log p(\hat{\omega}, \hat{\psi} \mid \xi) + \log p(\xi) - \log p(\hat{\omega}, \hat{\psi}) \\ &= \log[\int p(\phi, \hat{\omega}, \hat{\psi} \mid \xi) d\phi] + \log p(\xi) - \log p(\hat{\omega}, \hat{\psi}) . \end{aligned} \tag{24}$$

However, it is difficult to evaluate $\log \int p(\phi, \hat{\omega}, \hat{\psi} \mid \rho, \theta) d\phi$ analytically, and so a direct search for the MPV of ξ seems obstructed.

Let $q(\phi)$ be any PDF of ϕ, i.e. any non-negative function with unity integral. Because of the concavity of the logarithm function and Jensen's inequality,

$$\log \int p(\phi, \hat{\omega}, \hat{\psi} \mid \xi) d\phi = \log \int q(\phi)[p(\phi, \hat{\omega}, \hat{\psi} \mid \xi) / q(\phi)] d\phi \geq \int q(\phi) \log[p(\phi, \hat{\omega}, \hat{\psi} \mid \xi) / q(\phi)] d\phi . \tag{25}$$

The last term in (25) can be further expressed as follows

$$\begin{aligned} &\int q(\phi) \log[p(\phi, \hat{\omega}, \hat{\psi} \mid \xi) / q(\phi)] d\phi = \int q(\phi) \log p(\phi, \hat{\omega}, \hat{\psi} \mid \xi) d\phi - \int q(\phi) \log q(\phi) d\phi \\ &= \int q(\phi) \log p(\hat{\omega}, \hat{\psi} \mid \lambda) d\phi + \int q(\phi) \log p(\phi \mid \xi) d\phi - \int q(\phi) \log q(\phi) d\phi \\ &= \int q(\phi) \log p(\hat{\omega}, \hat{\psi} \mid \lambda) d\phi + \int q(\phi) \log p(\phi) d\phi - \int q(\phi) \log q(\phi) d\phi \\ &= \int q(\phi) \log p(\hat{\omega}, \hat{\psi} \mid \lambda) d\phi + C(q) = E_q[\log p(\hat{\omega}, \hat{\psi} \mid \lambda)] + C(q), \end{aligned} \tag{26}$$

where $C(q) = \int q(\phi) \log p(\phi) d\phi - \int q(\phi) \log q(\phi) d\phi$, and $E_q[h(\phi)] = \int h(\phi) q(\phi) d\phi$.

In this derivation, we used the fact that $p(\phi \mid \xi)$ is not a function of ξ because for the prior PDF, ϕ and ξ are independent. Combining (24), (25) and (26), we conclude that $E_q[\log p(\hat{\omega}, \hat{\psi} \mid \lambda)] + \log p(\xi) - \log p(\hat{\omega}, \hat{\psi}) + C(q)$ is a lower bound of $\log p(\xi \mid \hat{\omega}, \hat{\psi})$ for any PDF *q(ϕ)*. This lower bound depends on *q(ϕ)* and ξ, and we denote it by $L(q, \xi)$, that is:

$$L(q, \xi) \equiv E_q[\log p(\hat{\omega}, \hat{\psi} \mid \lambda)] + \log p(\xi) - \log p(\hat{\omega}, \hat{\psi}) + C(q). \quad (27)$$

Although it is difficult to optimize $\log p(\xi \mid \hat{\omega}, \hat{\psi})$ with respect to ξ subject to $A_\rho \rho + A_\theta \theta \le b$ due to the fact that $\log \int p(\phi, \hat{\omega}, \hat{\psi} \mid \xi) d\phi$ is hard to evaluate, it is relatively easy to optimize $L(q, \xi)$ with respect to ξ subject to $A_\rho \rho + A_\theta \theta \le b$ (later we will show that $L(q, \xi)$ is quadratic in ξ so that this optimization is a standard quadratic programming problem).

When *q(ϕ)* is fixed, the lower bound $L(q, \xi)$ can be improved by evaluating $\max_{\xi}[L(q, \xi)]$. The values of ξ that achieve this maximization subject to $A_\rho \rho + A_\theta \theta \le b$ are approximations of the MPV $\hat{\xi}$. The quality of this approximation depends the choice of *q(ϕ)*. The EM algorithm is an algorithm that iteratively chooses a 'good' *q(ϕ)* to improve the estimate of $\hat{\xi}$, then, in turn, takes the improved estimate of $\hat{\xi}$ to find a better *q(ϕ)*.

The procedure of the EM algorithm can be summarized by the following steps:

1) Initialize $\xi^{(0)}$ and $q^{(0)}(\phi)$.

2) At the i-th iteration:

(E-step) From $\xi^{(i)}$, derive a good $q^{(i)}(\phi)$. Compute $L[q^{(i)}(\phi), \xi]$.

(M-step) Find $\xi^{(i+1)} = \arg\max_{\xi} L[q^{(i)}(\phi), \xi]$ subject to $A_\rho \rho + A_\theta \theta \le b$.

3) Go back to step 2 for the (i+1)-th iteration and continue cycling until $\xi^{(i)}$ converge.

Let us first consider the E-step. It is critical to derive a good $q^{(i)}(\phi)$ from $\xi^{(i)}$. A bad choice of $q^{(i)}(\phi)$ may cause $L[q^{(i)}(\phi),\xi]$ to be a loose lower bound of $\log p(\xi \mid \hat{\omega},\hat{\psi})$, and $\xi^{(i+1)}$ will not be a good approximation for the MPV $\hat{\xi}$. On the other hand, if we let $q^{(i)}(\phi)$ be $p(\phi \mid \xi^{(i)},\hat{\omega},\hat{\psi})$, we have

$$
\begin{aligned}
& L[q^{(i)}(\phi),\xi^{(i)}] \\
&= E_{q^{(i)}}[\log p(\hat{\omega},\hat{\psi} \mid \phi,\xi^{(i)})] + \log p(\xi^{(i)}) - \log p(\hat{\omega},\hat{\psi}) + C[q^{(i)}(\phi)] \\
&= \int \log p(\hat{\omega},\hat{\psi} \mid \phi,\xi^{(i)})\, p(\phi \mid \hat{\omega},\hat{\psi},\xi^{(i)}) d\phi + \log p(\xi^{(i)}) - \log p(\hat{\omega},\hat{\psi}) \\
&\qquad + \int p(\phi \mid \hat{\omega},\hat{\psi},\xi^{(i)}) \log p(\phi \mid \xi^{(i)}) d\phi \\
&\qquad - \int p(\phi \mid \hat{\omega},\hat{\psi},\xi^{(i)}) \log p(\phi \mid \hat{\omega},\hat{\psi},\xi^{(i)}) d\phi \\
&= \int \log\left[p(\hat{\omega},\hat{\psi} \mid \phi,\xi^{(i)})\, p(\phi \mid \xi^{(i)}) / p(\phi \mid \hat{\omega},\hat{\psi},\xi^{(i)})\right] p(\phi \mid \hat{\omega},\hat{\psi},\xi^{(i)}) d\phi \\
&\qquad + \log p(\xi^{(i)}) - \log p(\hat{\omega},\hat{\psi}) \\
&= \int \log p(\hat{\omega},\hat{\psi} \mid \xi^{(i)})\, p(\phi \mid \hat{\omega},\hat{\psi},\xi^{(i)}) d\phi + \log p(\xi^{(i)}) - \log p(\hat{\omega},\hat{\psi}) \\
&= \log p(\hat{\omega},\hat{\psi} \mid \xi^{(i)}) + \log p(\xi^{(i)}) - \log p(\hat{\omega},\hat{\psi}) \\
&= \log p(\xi^{(i)} \mid \hat{\omega},\hat{\psi}). \qquad (28)
\end{aligned}
$$

Therefore, the choice of $q^{(i)}(\phi)$ being $p(\phi \mid \xi^{(i)},\hat{\omega},\hat{\psi})$ makes $L[q^{(i)}(\phi),\xi]$ exactly equal to $\log p(\xi \mid \hat{\omega},\hat{\psi})$ at $\xi^{(i)}$, and this is true for all iterations. This choice makes $\xi^{(i)}$ be able to actually converge to the MPV $\hat{\xi}$, which maximizes $\log p(\xi \mid \hat{\omega},\hat{\psi})$.

In order to compute $L[q^{(i)}(\phi),\xi]$, we only need to compute the first and second moments of $q^{(i)}(\phi)$, i.e. $E_{q^{(i)}}(\phi_r)$ and $E_{q^{(i)}}(\phi_r \phi_r^T)$, $r = 1 \ldots N_m$, since

$$
\begin{aligned}
& L[q^{(i)}(\phi),\xi] \\
&= E_{q^{(i)}}[\log p(\hat{\omega},\hat{\psi} \mid \lambda)] + \log p(\xi) - \log p(\hat{\omega},\hat{\psi}) + C[q^{(i)}(\phi)] \\
&= d - (1/2)\sum_{r=1}^{N_m}\sum_{j=1}^{N_s}\left[\log(\sigma_r^2) + E_{q^{(i)}}\left\{\left\|K\phi_r - \hat{\omega}_{r,j}^2 \cdot M\phi_r\right\|_{M^{-1}}^2 \Big/ \sigma_r^2\right\}\right. \\
&\qquad \left. + N_o \log(\delta_r^2) + E_{q^{(i)}}\left\{\left\|\hat{\psi}_{r,j} - a_r \Gamma \phi_r\right\|^2 \Big/ \delta_r^2\right\}\right] \\
&\qquad - (1/2)(\rho - \rho^0)^T (P_\rho^0)^{-1}(\rho - \rho^0) - (1/2)(\theta - \theta^0)^T (P_\theta^0)^{-1}(\theta - \theta^0), \qquad (29)
\end{aligned}
$$

where d is a quantity not depending on ξ. Using the fact that for the trace, *TR(AB) = TR(BA)*, we have

$$
\begin{aligned}
&L[q^{(i)}(\phi),\xi] \\
&= d-(1/2)\sum_{r=1}^{N_m}\sum_{j=1}^{N_s}\Big[\log(\sigma_r^2)+E_{q^{(i)}}\left\{TR\left\{M^{-1}[K\phi_r-\hat{\omega}_{r,j}^2\cdot M\phi_r][K\phi_r-\hat{\omega}_{r,j}^2\cdot M\phi_r]^T\right\}/\sigma_r^2\right\} \\
&\qquad +N_o\log(\delta_r^2)+E_{q^{(i)}}\left\{TR\left\{[\hat{\psi}_{r,j}-a_r\Gamma\phi_r][\hat{\psi}_{r,j}-a_r\Gamma\phi_r]^T/\delta_r^2\right\}\right\}\Big] \\
&\qquad -(1/2)(\rho-\rho^0)^T(P_\rho^0)^{-1}(\rho-\rho^0)-(1/2)(\theta-\theta^0)^T(P_\theta^0)^{-1}(\theta-\theta^0) \\
&= d-(1/2)\sum_{r=1}^{N_m}\sum_{j=1}^{N_s}\Big[\log(\sigma_r^2)+E_{q^{(i)}}\left\{TR\left\{M^{-1}K\phi_r\phi_r^TK+\hat{\omega}_{r,j}^4\cdot\phi_r\phi_r^TM-2\hat{\omega}_{r,j}^2\cdot M^{-1}K\phi_r\phi_r^TM\right\}/\sigma_r^2\right\} \\
&\qquad +N_o\log(\delta_r^2)+E_{q^{(i)}}\left\{TR\left\{[\hat{\psi}_{r,j}\hat{\psi}_{r,j}^T+a_r^2\Gamma\phi_r\phi_r^T\Gamma^T-2a_r\Gamma\phi_r\hat{\psi}_{r,j}^T]\right\}/\delta_r^2\right\}\Big] \\
&\qquad -(1/2)(\rho-\rho^0)^T(P_\rho^0)^{-1}(\rho-\rho^0)-(1/2)(\theta-\theta^0)^T(P_\theta^0)^{-1}(\theta-\theta^0) \\
&= d-(1/2)\sum_{r=1}^{N_m}\sum_{j=1}^{N_s}\Big[\log(\sigma_r^2) \\
&\qquad +TR\left\{M^{-1}KE_{q^{(i)}}(\phi_r\phi_r^T)K+\hat{\omega}_{r,j}^4\cdot E_{q^{(i)}}(\phi_r\phi_r^T)M-2\hat{\omega}_{r,j}^2\cdot M^{-1}KE_{q^{(i)}}(\phi_r\phi_r^T)M\right\}/\sigma_r^2 \\
&\qquad +N_o\log(\delta_r^2)+TR\left\{\hat{\psi}_{r,j}\hat{\psi}_{r,j}^T+a_r^2\Gamma E_{q^{(i)}}(\phi_r\phi_r^T)\Gamma^T-2a_r\Gamma E_{q^{(i)}}(\phi_r)\hat{\psi}_{r,j}^T]\right\}/\delta_r^2\Big] \\
&\qquad -(1/2)(\rho-\rho^0)^T(P_\rho^0)^{-1}(\rho-\rho^0)-(1/2)(\theta-\theta^0)^T(P_\theta^0)^{-1}(\theta-\theta^0)\,. \qquad (30)
\end{aligned}
$$

Moreover, $E_{q^{(i)}}(\phi_r)$ and $E_{q^{(i)}}(\phi_r\phi_r^T)$ can be evaluated analytically since $q^{(i)}(\phi)=p(\phi\,|\,\xi^{(i)},\hat{\omega},\hat{\psi})$ is a Gaussian PDF of ϕ, which is, in turn, due to the fact that $\log p(\phi\,|\,\xi^{(i)},\hat{\omega},\hat{\psi})$ is quadratic in ϕ by our model assumption:

$$
\begin{aligned}
&\log p(\phi\,|\,\xi^{(i)},\hat{\omega},\hat{\psi}) \\
&= d+\log p(\hat{\omega}\,|\,\phi,\xi^{(i)})+\log p(\hat{\psi}\,|\,\phi)+\log p(\phi) \\
&= d-(1/2)\sum_{r=1}^{N_m}\sum_{j=1}^{N_s}\left\{\left\|K^{(i)}\phi_r-\hat{\omega}_{r,j}^2M^{(i)}\phi_r\right\|_{M^{(i)^{-1}}}^2/\sigma_r^{(i)^2}+\left\|\hat{\psi}_{r,j}-a_r^{(i)}\Gamma\phi_r\right\|^2/\delta_r^{(i)^2}\right\}. \qquad (31)
\end{aligned}
$$

The exact values of $E_{q^{(i)}}(\phi_r)$ and $E_{q^{(i)}}(\phi_r\phi_r^T)$ are as follows:

$$
\begin{aligned}
&E_{q^{(i)}}(\phi_r)=E(\phi_r\,|\,\xi^{(i)},\hat{\omega},\hat{\psi}) \\
&=\arg\max_{\phi_r}\log p(\phi_r\,|\,\xi^{(i)},\hat{\omega},\hat{\psi}) \\
&=\left[\sum_{j=1}^{N_s}\left\{[K^{(i)}-\hat{\omega}_{r,j}^2M^{(i)}]^TM^{(i)^{-1}}[K^{(i)}-\hat{\omega}_{r,j}^2M^{(i)}]/\sigma_r^{(i)^2}+a_r^{(i)^2}\Gamma^T\Gamma/\delta_r^{(i)^2}\right\}\right]^{-1}\cdot\left[\sum_{j=1}^{N_s}a_r^{(i)}\Gamma^T\hat{\psi}_{r,j}/\delta_r^{(i)^2}\right] \qquad (32)
\end{aligned}
$$

and

$$E_{q^{(i)}}(\phi_r\phi_r^T) = E(\phi_r\phi_r^T \mid \xi^{(i)}, \hat{\omega}, \hat{\psi}) = Cov(\phi_r \mid \xi^{(i)}, \hat{\omega}, \hat{\psi}) + E(\phi_r \mid \xi^{(i)}, \hat{\omega}, \hat{\psi})E(\phi_r \mid \xi^{(i)}, \hat{\omega}, \hat{\psi})^T, \quad (33)$$

where

$$Cov(\phi_r \mid \xi^{(i)}, \hat{\omega}, \hat{\psi}) = \left[\sum_{j=1}^{N_s}\left\{[K^{(i)} - \hat{\omega}_{r,j}^2 M^{(i)}]^T M^{(i)-1}[K^{(i)} - \hat{\omega}_{r,j}^2 M^{(i)}]\Big/\sigma_r^{(i)2} + a_r^{(i)2}\,\Gamma^T\Gamma\Big/\delta_r^{(i)2}\right\}\right]^{-1}. \quad (34)$$

For the M-step, since $L[q^{(i)}(\phi), \xi]$ is concave in ξ, the optimization with respect to ξ subject to $A_\rho\rho + A_\theta\theta \le b$ can be also done with global maximization guaranteed. We maximize $L[q^{(i)}(\phi), \xi]$ using two iterative steps: first with respect to $\{\sigma_r^2, \delta_r^2 : r = 1...N_m\}$ with $\{\rho, \theta, a_r : r = 1...N_m\}$ fixed in order to deduce the conditional optimal value $\{\tilde{\sigma}_r^2, \tilde{\delta}_r^2 : r = 1...N_m\}$, and then with respect to $\{\rho, \theta, a_r : r = 1...N_m\}$ with $\{\tilde{\sigma}_r^2, \tilde{\delta}_r^2 : r = 1...N_m\}$ substituted into (30). The first maximization gives

$$\begin{aligned}
\tilde{\sigma}_r^2 &= (1/N_s)\sum_{j=1}^{N_s} TR\left\{M^{-1}KE_{q^{(i)}}(\phi_r\phi_r^T)K + \hat{\omega}_{r,j}^4 \cdot E_{q^{(i)}}(\phi_r\phi_r^T)M - 2\hat{\omega}_{r,j}^2 \cdot M^{-1}KE_{q^{(i)}}(\phi_r\phi_r^T)M\right\} \\
\tilde{\delta}_r^2 &= 1/(N_s N_o)\sum_{j=1}^{N_s} TR\left\{\hat{\psi}_{r,j}\hat{\psi}_{r,j}^T + a_r^2\Gamma E_{q^{(i)}}(\phi_r\phi_r^T)\Gamma^T - 2a_r\Gamma E_{q^{(i)}}(\phi_r)\hat{\psi}_{r,j}^T\right\}.
\end{aligned} \quad (35)$$

The second maximization can be solved by a standard quadratic programming algorithm subject to $A_\rho\rho + A_\theta\theta \le b$. The inner iteration for the M-step stops when satisfactory convergence is achieved with global maximization guaranteed.

We can restate this special EM algorithm, which chooses $q^{(i)}(\phi) = p(\phi \mid \xi^{(i)}, \hat{\omega}, \hat{\psi})$, as following:

1) Initialize $\xi^{(0)}$ and $q^{(0)}(\phi)$.

2) At the i-th iteration:

(E-step) Compute the first and second moments $E_{q^{(i)}}(\phi_r)$ and $E_{q^{(i)}}(\phi_r\phi_r^T)$, $r = 1…N_m$, and substitute them into (30) to compute $L[q^{(i)}(\phi), \xi]$ analytically.

(M-step) Solve the concave optimization problem

$$\xi^{(i+1)} = \arg\max_{\xi} L[q^{(i)}(\phi), \xi] \text{ subject to } A_\rho \rho + A_\theta \theta \le b$$

by an inner iteration:

2a) Fix $\{\rho, \theta, a_r : r = 1...N_m\}$, optimize $L[q^{(i)}(\phi), \xi]$ with respect to $\{\sigma_r^2, \delta_r^2 : r = 1...N_m\}$.

2b) Fix $\{\sigma_r^2, \delta_r^2 : r = 1...N_m\}$, optimize $L[q^{(i)}(\phi), \xi]$ with respect to $\{\rho, \theta, a_r : r = 1...N_m\}$.

3c) Go back to step 2a until convergence of the inner iteration.

3) Go back to step 2 for the (i+1)-th iteration and continue cycling until $\xi^{(i)}$ converge.

After convergence to satisfactory accuracy, $\hat{\xi}$ is found, and $\hat{\phi}$ is simply the first moment of $p(\phi | \hat{\xi}, \hat{\omega}, \hat{\psi})$ since

$$p(\phi, \hat{\xi} | \hat{\omega}, \hat{\psi}) = p(\phi | \hat{\xi}, \hat{\omega}, \hat{\psi}) p(\hat{\xi} | \hat{\omega}, \hat{\psi}), \tag{36}$$

and note that

$$\begin{aligned}
\hat{\phi} &= \arg\max_{\phi} p(\phi, \hat{\xi} | \hat{\omega}, \hat{\psi}) \\
&= \arg\max_{\phi} p(\phi | \hat{\xi}, \hat{\omega}, \hat{\psi}) p(\hat{\xi} | \hat{\omega}, \hat{\psi}) \\
&= \arg\max_{\phi} p(\phi | \hat{\xi}, \hat{\omega}, \hat{\psi}) \\
&= E(\phi | \hat{\xi}, \hat{\omega}, \hat{\psi}).
\end{aligned} \tag{37}$$

The last equality in (37) is due to the fact that $p(\phi | \hat{\xi}, \hat{\omega}, \hat{\psi})$ is Gaussian. We call this special EM algorithm the Tight EM (TEM) algorithm since the tight lower bound of $\log p(\xi | \hat{\omega}, \hat{\psi})$ is achieved for each iteration. The TEM algorithm is an ascent optimization algorithm for $\log p(\xi | \hat{\omega}, \hat{\psi})$, i.e. $\log p(\xi^{(i)} | \hat{\omega}, \hat{\psi})$ always increases during iterations. Indeed, during the M-step, we let

$$\xi^{(i+1)} = \arg\max_{\xi} L[q^{(i)}(\phi), \xi], \tag{38}$$

therefore,

$$L[q^{(i)}(\phi),\xi^{(i+1)}] \geq L[q^{(i)}(\phi),\xi^{(i)}] = \log p(\xi^{(i)} \mid \hat{\omega},\hat{\psi}). \tag{39}$$

Furthermore, after the next E-step,

$$\begin{aligned} &\log p(\xi^{(i+1)} \mid \hat{\omega},\hat{\psi}) \\ &= L[q^{(i+1)}(\phi),\xi^{(i+1)}] \\ &= \max_{q} L[q,\xi^{(i+1)}] \geq L[q^{(i)}(\phi),\xi^{(i+1)}] = \log p(\xi^{(i)} \mid \hat{\omega},\hat{\psi}). \end{aligned} \tag{40}$$

The strategy mentioned in the second paragraph of this section is actually another special case of the EM algorithm. It is equivalent to the case that we choose $q^{(i)}(\phi)$ to be a unit delta function centered at $E(\phi \mid \xi^{(i)},\hat{\omega},\hat{\psi})$. In this case, $L[q^{(i)}(\phi),\xi]$ will not be a tight lower bound of $\log p(\xi \mid \hat{\omega},\hat{\psi})$ at any ξ, and $\xi^{(i)}$ will only converge to an approximate value of the MPV $\hat{\xi}$. It is, in general, hard to evaluate the error between this approximate value and the MPV. However, based on our experience, this special EM algorithm performs roughly the same as the TEM algorithm.

The EM algorithm solves the second difficulty listed in the beginning of this section since it decomposes the high-dimensional non-concave optimization problem into two coupled concave optimization problems with analytical solutions. In our experience, when a nonlinear programming algorithm, e.g. a quasi-Newton or steepest descent algorithm, is used to find the MPV, the solution can be sometimes trapped in a local minimum away from the MPV even when the initial search point is close to the MPV. We find that the EM algorithm is robust in the sense that the initial point does not have to be close to the MPV in order to converge to the MPV. Nevertheless, the EM algorithm can be sometimes quite slow.

4 Results of simulated Phase II benchmark

Time histories of sampling interval 0.002s and total duration 210s were generated for all damage cases by the Matlab program for the simulated Phase II benchmark that was downloaded

from the ASCE benchmark website [7]. They are partitioned temporally into ten sets (N_s = 10) of equal duration of 20s to yield ten sets of independent estimates of the experimental modal parameters for each damage case. The first ten seconds is ignored since it contains transient responses due to the stationary excitation being started at t = 0 during the generation of the simulated data. When generating the time histories, we assume damping ratios equal to 1% for all modes and measurement noise equal to 10% RMS of the actual acceleration at the measured DOF. We will mention a damage case using its damage pattern symbol augmented by the sensor setup symbol, e.g. RB.ps means the reference braced case with partial-sensor measurement.

4.1 Modal identification

Eight modes (N_m = 8), four in the strong (x) direction and four in the weak (y) direction, of the structure are identified for all cases. Tables 1 and 2 show the average value of the modal frequencies and damping ratios identified from the ten sets of time histories for the braced cases in the full-sensor and partial-sensor scenarios, respectively, and those of the unbraced cases are shown in Tables 3 and 4. The corresponding values of the coefficient of variation (c.o.v.), defined as the ratio of the standard error to the mean value, are shown in percent in these tables. Table 5 shows the actual modal parameters of each case, calculated using the HKUST 120-DOF model. The mean values in Tables 1-4 are close to the actual values. The modal frequencies in the weak direction are expected to be unchanged because of the damage patterns, except for the Blind2 case.

For the full-sensor (partial-sensor) scenario, the sixteen (eight) response measurements, four (two) on each face of the structure, are used to identify the Euclidean-normalized modeshape components at the ‘+x’ ‘-x’ ‘+y’ ‘-y’ faces of the structure (‘+x’ ‘-x’ ‘+y’ ‘-y’ represent the directions of the outward normal of the faces), which are plotted in Figures 7-28 for each

damage case. In these plots, the identified modeshape components are joined by straight line segments so that, in the partial-sensor cases, the full modeshape of each higher mode is not revealed. Notice that the identified modeshapes for the unbraced cases show larger variability than those of the braced cases. Also notice that there is some modeshape migration phenomenon between two modes whose modal frequencies are close, i.e. some modeshape components of one mode migrates to another mode, e.g. the first two modes in DP1B and DP3B. There is no imposition of modeshape orthogonality since not all components of the modeshape are identified, only those components at the observed DOF.

For damping ratios, significantly larger values of c.o.v. are observed, although the damping ratios are not used for damage detection. This suggests that, as far as the current study is concerned, although the modal frequencies and modeshapes can be identified reasonably well, more information, especially about the excitation, is needed to identify the damping ratios more precisely.

4.2 Damage detection and assessment

4.2.1 Braced cases

A 3-D 12-DOF shear building model is used for damage detection for the braced cases. The model assumes rigid floors, and three DOF, translations along the x- and y-axes and rotation along the z-axis, are assigned to each story to give 12 DOF. In order to locate the faces sustaining damage, four stiffness parameters are used for each story to give sixteen stiffness parameters:

$$K(\theta) = \sum_i \sum_j \theta_{ij} \overline{K}_{ij} \,, \tag{41}$$

where $i = 1, \ldots, 4$, $j =$ '$+x$' '$-x$' '$+y$' '$-y$', and the indices i and j denote the story number and the direction of the outward normal of a face, respectively. The $\overline{K}_{ij}$ are the 'nominal' stiffness matrices computed based on shear building assumptions for the original undamaged structure. The

stiffness model was originally proposed in [12] and yielded satisfactory damage detection results for the Phase I simulated benchmark studies. For the reference cases (RB), the prior PDF on the sixteen stiffness parameters is taken to be independent Gaussian with mean and c.o.v. both equal to unity and with the affine constraints that all parameters are above zero. For other cases, it is taken to be independent Gaussian with mean and c.o.v. both equal to unity and with the following affine constraints

$$0 \le \theta_i \le (1+2\hat{\zeta}_i^{RB})\hat{\theta}_i^{RB} \qquad i = 1...N_\theta, \tag{42}$$

where $\hat{\theta}_i^{RB}$ is the MPV of θ_i from the reference case, and $\hat{\zeta}_i^{RB}$ is the corresponding c.o.v. This prior PDF reflects the fact that the stiffness parameters for damaged cases can only be less than those of the reference cases.

In calculating the nominal story masses, the mass of the columns is lumped at the floors that they are connected to. One mass parameter is used for each story to give four mass parameters:

$$M(\rho) = \sum_i \rho_i \overline{M}_i, \tag{43}$$

where $i = 1, \ldots, 4$ represents the story number and the $\overline{M}_i$ are the nominal mass matrices computed based on the original undamaged structure (the nominal mass from the first to the fourth story is 3242 kg, 2652 kg, 2652 kg, and 1809 kg). The prior PDF for the uncertain mass parameters is assumed to be independent Gaussian with mean equal to unity and c.o.v. equal to 0.1%. Assuming the story masses to be uncertain in the Bayesian updating methodology improves the robustness of the damage detection process to modeling assumptions that are possibly incompatible with the properties of the actual structure [12].

In all the cases considered, the stiffness and mass parameters are found to be globally identifiable, so the updated PDF can be well-approximated in the neighborhood of the MPV by a

multi-dimensional Gaussian PDF with mean equal to the MPV of the stiffness and mass parameters and covariance matrix equal to the negative of the inverse of the Hessian matrix of the logarithm of the updated PDF. For full-sensor scenarios, all of the twelve DOF are measured, so the algorithm for full modeshape information is used to find the MPV of the stiffness parameters. For partial-sensor scenarios, the TEM algorithm is used to find the MPV of the stiffness parameters. It is found that the initial values of the system parameters do not have to be close to the MPV in order to finally converge to the MPV.

The stiffness ratios for the MPV of the stiffness parameters for DP1B, DP2B, DP3B, DP3Bu, Blind1, Blind2 with respect to those for the undamaged (RB) case are tabulated in Tables 6 and 7 for the full-sensor and partial-sensor scenarios, respectively, with the corresponding c.o.v. shown. Using shear building assumptions, the actual stiffness ratio for a particular face with 25% and 50% stiffness loss in one brace is computed to be 94.3% and 88.7%, respectively.

For the full-sensor scenarios (Table 6), the identified stiffness ratios for the DP1B.fs, DP2B.fs, and DP3B.fs cases are close to their actual values. The stiffness parameters whose values decline by amount significantly larger than their c.o.v. are considered possibly damaged and marked with asterisks. For most stiffness parameters in the DP1B.fs, DP2B.fs, DP3B.fs, and DP3Bu.fs cases, the damage patterns are reliably detected in both qualitative and quantitative ways. For example, all damage patterns of the DP1B.fs, DP2B.fs, DP3B.fs, and DP3Bu.fs cases are detected, but one false damage detection is found for the DP3Bu.fs case due to a slightly biased estimate of $\theta_{4,+y}$. Nevertheless, the identified stiffness reduction for the false detection is small (less than 4%). Also, for the DP3Bu.fs case, the estimate of $\theta_{1,-y}$ is noticeably biased (0.80 as opposed to its actual value 0.89, while the c.o.v. is only 1.55%).

The results for the partial-sensor scenarios (Table 7) are similar to those for the full-sensor scenarios except that two extra slightly biased estimates are found for $\theta_{1,+x}$ of the DP3B.ps case and $\theta_{4,-x}$ of the DP3Bu.ps case; therefore, three false damage detections, $\theta_{1,+x}$ of the DP3B.ps case and $\theta_{4,+y}$ and $\theta_{4,-x}$ of the DP3Bu.ps case, are found to be due to the biased estimates. Nevertheless, the identified stiffness reductions for the three false detections are small (less than 8%).

The results for Blind1 indicate that the damage should have occurred at either $\theta_{1,-y}$ or $\theta_{2,-y}$ (it has been given a priori that there is only one brace failure). Using the Blind1 results, the reduction in $\theta_{1,-y}$ and $\theta_{2,-y}$ roughly corresponds to 25% and 20% reduction in stiffness, respectively, at the corresponding locations. The actual damage location is $\theta_{2,-y}$ and the actual stiffness reduction is 32% [19]. The results for Blind2 indicate that the $\theta_{4,+x}$, $\theta_{1,-x}$, $\theta_{3,-x}$, and $\theta_{1,-y}$ locations are likely to be damaged. Using the Blind2.fs results, the 18%, 4.9%, 8.6%, and 5.2% reduction in $\theta_{4,+x}$, $\theta_{1,-x}$, $\theta_{3,-x}$, and $\theta_{1,-y}$ corresponds to 76.7%, 21.7%, 37.9%, and 23.1% reduction in the stiffnesses, respectively, at the corresponding locations. The actual damage locations are $\theta_{4,+x}$, $\theta_{3,-x}$, and $\theta_{1,-y}$, and the corresponding actual stiffness reductions are 47.48%, 39.32%, and 23.79%. In conclusion, the results on the blind tests show that the methodology can detect all actual damage with one false detection in each of the two tests.

Using the marginal PDFs for the stiffness parameters, the probability of damage, $P_{ij}(d)$, equal to the probability that the decrease of θ_{ij} is more than a fraction of d compared to the undamaged state, is computed. The results are shown in Figures 29-34 for the full-sensor scenario and in Figures 35-40 for the partial sensor scenario. The Euclidean-normalized identified system modeshapes are shown in Figures 41-47 for the partial-sensor scenario, in which the projections of the lateral components of the system modeshapes onto the +x, -x, +y, and –y faces are shown. The torsional modeshape components of the eight identified

The torsional modeshape components of the eight identified translational modes are not shown since they are close to zeros. These modeshapes may be compared with the corresponding modeshapes identified directly from the dynamic response and shown in Figures 14-20.

4.2.2 Unbraced cases

For the unbraced cases, a 3-D 36-DOF model that assumes rigid floors in the x-y plane and allows rotation along the x- and y-axes is proposed. All nodes at the same story are assumed to have identical x- and y-direction translations, and the floor is assumed to be rigid with respect to rotation along the z-axis to give 3 of the 9 DOF for each story. Nodes are allowed to rotate along the x- and y-axes in a constrained way: nodes in each story with the same x-coordinates or same y-coordinates are assumed to have the same amount of rotation along the y-axis and x-axis, respectively, to give the remaining 6 DOF for each floor. Translation along the z-direction is not allowed in this model.

Two parameters are used for the rotational stiffness in each story: it is assumed that the rotational stiffness of all beam-column connections in the same story along the x-axis (or along the y-axis) is identical. This assumption is imposed since the experimentally identified modeshapes for the unbraced cases (Figures 21-28) indicate that the modeshape components in the x and y directions are mostly decoupled; therefore, in practice it is unlikely that the face sustaining the damage can be distinguished. Besides the rotational stiffness, two parameters are used for the strong (x)-direction and weak (y)-direction column stiffness to give ten stiffness parameters in total:

$$K(\theta) = \theta_{c,x}\overline{K}_{c,x} + \theta_{c,y}\overline{K}_{c,y} + \sum_i \sum_j \theta_{ij}\overline{K}_{ij} \ , \qquad (44)$$

where $i = 1, \ldots, 4$, $j =$ *'x'* and *'y'*, and the indices i and j denote the story number and the axis along which the rotational stiffness is active, respectively; $\overline{K}_{ij}$ are the nominal rotational stiff-

ness matrices computed based on the model assumptions for the original undamaged structure; $\overline{K}_{c,x}$ and $\overline{K}_{c,y}$ are the x-direction and y-direction, respectively, nominal stiffness matrices contributed by the columns.

Due to the fact that the stiffness matrix of the unbraced benchmark structure is dominated by the columns and the fact that the columns also provide rotational stiffness, slight errors in the identified column stiffness parameters will significantly influence the values of the identified rotational stiffness parameters. This indicates that in order to reliably detect and assess rotational stiffness damage, sufficient prior information about the column stiffness is needed. Therefore, the prior PDF on the two column stiffness parameters is taken to be independent Gaussian with mean and c.o.v. equal to 1 and 1%. The prior PDF of the eight rotational stiffness parameters is taken to be independent Gaussian with mean and c.o.v. equal to 1 and 20%. Similar to the braced cases, the mass of the columns is lumped at the floors that they are connected to, and one mass parameter is used for each story to give four mass parameters. The prior PDF for the uncertain mass parameters is assumed to be independent Gaussian with mean and c.o.v. equal to 1 and 0.1%.

In all the cases considered, the stiffness and mass parameters are found to be globally identifiable. For both full-sensor and partial-sensor scenarios, the TEM algorithm is used to find the MPV of the stiffness parameters. The initial values of the system parameters do not have to be close to the MPV in order to finally converge to the MPV. The stiffness ratios for the MPV of the stiffness parameters for DP1U, DP2U, and DP1Uu with respect to those of the undamaged (RU) case are tabulated in Tables 8 and 9 for the full-sensor and partial-sensor cases, respectively, with the corresponding c.o.v. shown.

For the full-sensor scenario (Table 8), all damage patterns in the DP1U.fs, DP2U.fs, and DP1Uu.fs cases can be reliably detected. Slightly biased estimates are found for $\theta_{3,y}$ of the DP1U.fs and DP1Uu.fs cases, and therefore two false damage detections are found due to the biased estimates. Similar results are found for the partial-sensor scenario (Table 9) except that the two false detections are now $\theta_{2,y}$ and $\theta_{3,y}$ of the DP2U.ps. Notice that all false detections indicate minor damage (less than 10% of stiffness loss), while most correct detections indicate major damage (higher than 25% of stiffness loss) at the corresponding locations. Because the experimental modeshapes contain little information about the rotational stiffness, the damage detection results for the full-sensor and partial-sensor scenarios are similar.

Using the marginal PDFs for the rotational stiffness parameters, the probability of damage, $P_{ij}(d)$, is computed and shown in Figures 48-50 for the full-sensor scenario and in Figures 51-53 for the partial sensor scenario. The Euclidean-normalized identified system modeshapes are shown in Figures 54-57 and Figures 58-61 for the full-sensor and partial-sensor scenario, respectively, in which the symbols +x, -x, +y, and –y indicate the lateral components of the system modeshapes projected onto the corresponding faces, and symbols Rx, Ry, and Rz indicate the system modeshape components for rotations along the x, y, and z axes, respectively.

5 Results of experimental Phase II benchmark

For each configuration (Configs 1-9) and each type of excitation (hammer, ambient vibration, and shaker), the experimental time histories are divided into three segments to yield three sets of independent estimates of the experimental modal parameters. All acceleration data is filtered by a Butterworth high-pass filter with cut-off frequency equal to 0.1Hz to eliminate the mean and drift. We will mention a configuration using its configuration number augmented by

the excitation type (‘h’, ‘a’, and ’s’ stand for hammer, ambient vibration, and shaker, respectively), e.g. Config2.h denotes Configuration 2 with the hammer excitation.

The input force time history of the shaker (proportional to the measured acceleration at the attached mass) is provided in the experimental Phase II dataset. However, the force data was contaminated by the structural response which is shown by its Fourier spectrum having resonant peaks at the natural frequencies of the benchmark structure. Therefore, the input force data are not used in the analysis, and the shaker cases are treated as if they are subject to unknown excitation. As a result, only the shaker cases with random input are analyzed.

5.1 Modal identification

For the braced cases (Configs 1-6), five modes, including the first and second translation modes in the x and y directions and the first torsion mode, are identified. For the unbraced cases (Configs 7-9), only the hammer excitation is studied, and eight modes, including the first, second, and third translation modes in the x and y directions and the first and second torsion modes, are identified. Tables 10, 11, and 12 show the average values and the c.o.v. of the modal frequencies and damping ratios for all excitation types. The variability for the ambient-vibration and shaker excitations is significantly larger than that for the hammer excitation. This is due to the fact that the input excitations for the former two cases are unknown, while it is known that the input excitation for the hammer is zero after the impulsive force.

The fifteen acceleration measurements, ten on the +y and –y faces of the structure sensing the x (strong) direction and five at the floor centers sensing the y (weak) direction, are used to identify the modeshape components at the ‘+y’ ‘-y’ faces and the center of the structure, which are plotted in Figures 62-82 for each configuration. Notice that for the ambient-vibration cases (Figures 71-76), there are unusual kinks in many of the modeshape components measured

at the floor centers, and for the shaker cases (Figures 77-82), many experimental modeshapes have irregular appearances. The experimental modeshapes for the hammer excitation have smaller variability than those for the ambient-vibration and shaker excitations. Significantly larger values of c.o.v. are observed for damping ratios in all cases.

5.2 Damage detection and assessment

5.2.1 Braced cases (Configs 1-6)

The 3-D 12-DOF shear building model that was used for the braced cases in simulated Phase II is adapted. The nominal stiffness matrices $\overline{K}_{ij}$ are identical to those used in simulated Phase II. It is expected that the uncertainties with experimental Phase II are significantly larger than those with simulated Phase II; therefore, it is decided that more prior information for the stiffness parameters should be imposed to regularize the possibly ill-posed identification problem. The prior PDF on the sixteen stiffness parameters is taken to be independent Gaussian with mean and c.o.v. equal to 1 and 20% with the following affine constraints to reflect the fact that the stiffness parameters for damaged cases can only be less than those of the reference case.

$$0 \le \theta_i \le (1+2\hat{\varsigma}_i^{Config1})\hat{\theta}_i^{Config1}, \tag{45}$$

where $\hat{\theta}_i^{Config1}$ is the MPV of θ_i from Config 1, and $\hat{\varsigma}_i^{Config1}$ is the corresponding c.o.v. The prior c.o.v. is chosen to be 20% since if we know a priori that the damage is on braces only, the largest possible reduction in the stiffness parameter is roughly 40% (computed based on shear building assumptions). But the prior with 20% c.o.v. does not prevent the identified stiffness ratios from dropping below 60% to accommodate the modeling errors.

The calculation of the mass matrix is identical to that in simulated Phase II except that $\overline{M}_i$ is computed based on the mass distribution of the test structure, i.e. the floor mass is 1000kg,

1000kg, 1000kg, 750kg for the first, second, third, and fourth floors. The prior PDF for the uncertain mass parameters is assumed to be independent Gaussian with mean and c.o.v. equal to 1 and 0.1%.

Since there are three accelerometers in each story, the measurements at all DOF of the identification model can be deduced from the data, so the algorithm for full modeshape information is used to find the MPV of the stiffness parameters. The stiffness ratios for the MPV of the stiffness parameters for Configs 2-6 with respect to those for the undamaged (Config 1) case are tabulated in Tables 13, 14, and 15 for the three excitation types with the corresponding c.o.v. shown. The stiffness parameters whose reductions are significantly greater than their c.o.v. are marked with asterisks.

For the hammer excitation, all brace damage is detected, and no false detection is found. Using shear building assumptions, the stiffness ratios for a particular face with removal of one and two braces are 77.4% and 54.87%, respectively. However, the identified stiffness ratios for faces with removal of one and two braces are around 60% and 20%, respectively, which are not consistent with the computed ratios. Despite this inconsistency, the estimates for the stiffness losses are internally consistent, i.e. removal of one and two braces corresponds to 40% and 80% reduction in stiffness, respectively. The probabilities of damage, $P_{ij}(d)$, for the hammer cases are plotted in Figures 83-87 for all braced configurations.

For the ambient-vibration excitation, all damage is also detected. The identified stiffness ratios are close to those for the hammer cases. Several false detections are found, and the false detections in $\theta_{2,+x}$ and $\theta_{2,-x}$ indicate significant stiffness reduction. These are probably due to the unusual kinks exhibited in the experimental modeshape components measured at the floor centers. For other false detections, the identified stiffness reductions are not significant (all less than

26%). The probabilities of damage, $P_{ij}(d)$, for the ambient-vibration cases are plotted in Figures 88-92 for all braced configurations.

For the shaker cases, reliable damage detection cannot be achieved, probably due to the irregular experimental modeshapes. Although most damage is detected, two locations were missed; moreover, many false detections are found, and most of them indicate significant stiffness reduction.

5.2.2 Unbraced cases (Configs 7-9)

The 3-D 36-DOF model that is used for the unbraced cases in simulated Phase II is adapted. The nominal stiffness matrices are computed based on the model assumptions for the original undamaged structure. The prior PDF on the two column stiffness parameters is taken to be independent Gaussian with mean and c.o.v. equal to 1 and 1%. The prior PDF of the eight rotational stiffness parameters is taken to be independent Gaussian with mean and c.o.v. equal to 1 and 20%. The affine inequality constraints are identical to (45) except that $\hat{\theta}_i^{Config1}$ and $\hat{\varsigma}_i^{Config1}$ are replaced by $\hat{\theta}_i^{Config7}$ and $\hat{\varsigma}_i^{Config7}$. The mass of the columns is lumped at the floors that they are connected to, and one mass parameter is used for each story to give four mass parameters. The prior PDF for the uncertain mass parameters is assumed to be independent Gaussian with mean and c.o.v. equal to 1 and 0.1%.

Only the hammer cases are considered for the unbraced cases since the corresponding experimental modeshapes have the best quality. Because all DOF of the identification model are not fully measured, the TEM algorithm is used to find the MPV of the stiffness parameters. In all the cases considered, the stiffness and mass parameters are found to be globally identifiable. The stiffness ratios between the MPV of the stiffness parameters for Config8.h and Config9.h with respect to those for Config.7h are tabulated in Tables 16 with the corresponding c.o.v. shown.

Although most damage except $\theta_{4,y}$ of Config8.h is detected, many false detections are found, and some of them indicate significant stiffness reduction. It is believed that the poor performance is due to the fact that the stiffness matrix of the structure is dominated by the columns, rendering the identification of rotational stiffness difficult. In the simulated Phase II benchmark, the rotational stiffness damage was successfully detected probably because the modeling error is relatively small. For the experimental Phase II benchmark, the modeling error may be too large to have the rotational stiffness damage reliably detected. Since the results of damage detection are poor, the plots for the probability of damage as well as the identified system modeshapes are not shown.

6 Conclusion

This report examines the use of a two-step Bayesian probabilistic structural health monitoring approach on the IASC-ASCE Phase II simulated and experimental benchmark studies. For the braced cases, all the brace damage can be reliably detected for the simulated benchmark studies, and the identified stiffness reduction is accurate. For the experimental Phase II benchmark, the damage can be detected reliably for the hammer and ambient-vibration excitations, while this is not the case for the shaker excitation. This is partly due to the fact that the shaker force input data is contaminated by the structural response and therefore is not used in the analysis. For the unbraced cases in the simulated Phase II benchmark, all rotational stiffness damage of the beam-column connections is detected and assessed reliably if sufficient prior information on the column stiffness is available. For the experimental Phase II benchmark, reliable damage detection for the unbraced cases cannot be achieved, probably due to the dominance of the column stiffness and the large modeling errors. The proposed Expectation-Maximization algorithm for

searching for the most probable values of the stiffness parameters is found to be robust compared to standard nonlinear programming algorithms.

References

[1] H. G. Natke and J. T. P. Yao (Eds). *Proceedings of the Workshop on Structural Safety Evaluation Based on System Identification Approaches*, Wiesbaden: Vieweg and Sons, 1988.

[2] F. K. Chang (Eds). *Proceedings of the 2nd International Workshop on Structural Health Monitoring*, Stanford University, 1999.

[3] H. M. Kim, T. J. Bartkowicz, S. W. Smith, and D. Zimmerman. Health monitoring of large structures. *Journal of Sound and Vibration*, **27**(6): 12-17, 1995.

[4] J. L. Beck, S. K. Au, and M. W. Vanik. Monitoring structural health using a probabilistic measure. *Computer-Aided Civil and Infrastructure Engineering*, **16**: 1-11, 2001.

[5] D. Bernal. Load vectors for damage localization. *Journal of Engineering Mechanics*, **128**(1), 7-14, 2002.

[6] L. S. Katafygiotis, C. Papadimitriou, and H. F. Lam. A probabilistic approach to structural model updating. *Soil Dynamics and Earthquake Engineering*, **17**(7-8), 495-507, 1998.

[7] ASCE SHM benchmark website http://wusceel.cive.wustl.edu/asce.shm/benchmarks.htm.

[8] E. A. Johnson, H. F. Lam, L. S. Katafygiotis, and J. L. Beck. A benchmark problem for structural health monitoring and damage detection. *Proceedings of the 14th Engineering MechanicsConferenc*e, Austin, Texas, May, 2000. ASCE.

[9] S. J. Dyke, D. Bernal, J. L. Beck, C. Ventura. An experimental benchmark problem in structural health monitoring. *Proceedings of the 3rd International Workshop on Structural Health Monitoring*, Stanford, September 12-14, 2001.

[10] D. Bernal, S. J. Dyke, J. L. Beck, and H. F. Lam. Phase II of the ASCE benchmark study on structural health monitoring, *Proceedings of the 15th Engineering Mechanics Division Conference of the American Society of Civil Engineer*s, New York, NY, June, 2002.

[11] Vanik MW, Beck JL, Au SK. A Bayesian probabilistic approach to structural health monitoring. *Journal of Engineering Mechanic*s, **126**, 738-745, 2000.

[12] K. V. Yuen, S. K. Au, and J. L. Beck. Two-stage structural health monitoring approach for Phase I benchmark studies. Accepted by *Journal of Engineering Mechanics*, 2002.

[13] J. L. Beck. Determining models of structures from earthquake records. Technical Report EERL 78-01, Earthquake Engineering Research Laboratory, California Institute of Technology, Pasadena, California, 1978.

[14] J. L. Beck, B. S. May, and D. C. Polidori. Determination of modal parameters from ambient vibration data for structural health monitoring. In *First World Conference on Structural Contro*l, pages TA3:3–TA3:12, Pasadena, California, 1994.

[15] J. L. Beck and L. S. Katafygiotis. Updating models and their uncertainties – Bayesian statistical framework. *Journal of Engineering Mechanic*s, 124(4):455–461, 1998.

[16] M. W. Vanik. A Bayesian probabilistic approach to structural health monitoring. Technical Report EERL 97-07, Earthquake Engineering Research Laboratory, California Institute of Technology, Pasadena, California, 1997.

[17] R. D. Rosenkrantz (Ed). E. T. Jaynes: *Papers on probability, statistics and statistical physics*, Dordrecht, Holland: D. Reidel Publishing Co., 1982.

[18] R. H. Shumway and D. S. Stoffer. An approach to time series smoothing and forecasting using the EM algorithm. *Journal of Time Series Analysis*, 4: 253-263, 1982.

[19] H. F. Lam. Phase IIe of the IASC-ASCE benchmark study on structural health monitoring. *Proceedings of IMAC-XXI*, Orlando, FL, February, 2003.

Table 1. Experimental modal parameters for the braced cases of the full-sensor scenario in simulated Phase II.

	Frequency (Hz)								Damping ratio (%)							
	W1*	S1*	W2	S2	W3	S3	W4	S4	W1	S1	W2	S2	W3	S3	W4	S4
RB.fs	8.33	8.75	23.14	25.33	36.11	40.82	46.34	55.45	0.99	1.23	0.93	0.93	0.63	0.70	0.84	0.80
c.o.v (%)	0.76	0.49	0.44	0.37	0.45	0.25	0.40	0.23	51.74	41.69	64.05	42.40	55.64	50.35	38.08	34.16
DP1B.fs	8.33	8.44	23.14	24.56	36.11	40.40	46.34	55.35	1.20	0.85	0.94	0.84	0.63	0.98	0.84	0.81
c.o.v (%)	0.75	0.57	0.43	0.19	0.45	0.33	0.40	0.23	39.21	80.57	62.48	63.46	56.02	31.61	38.41	27.69
DP2B.fs	8.33	8.59	23.14	24.94	36.11	40.63	46.34	55.41	1.12	0.95	0.93	1.01	0.63	0.74	0.84	0.81
c.o.v (%)	0.75	0.68	0.43	0.51	0.45	0.23	0.40	0.23	47.35	79.58	62.75	49.69	55.60	53.36	38.48	31.63
DP3B.fs	8.32	8.37	23.14	24.11	36.11	40.31	46.34	54.65	1.27	1.31	0.94	1.08	0.64	1.04	0.84	1.01
c.o.v (%)	0.64	0.49	0.43	0.36	0.45	0.30	0.40	0.39	35.99	61.00	62.54	43.56	55.87	33.96	38.51	26.58
DP3Bu.fs	8.33	8.54	23.14	24.75	36.11	39.99	46.34	55.05	0.99	1.24	0.91	1.00	0.65	1.28	0.85	0.91
c.o.v (%)	0.74	0.67	0.45	0.55	0.44	0.34	0.39	0.20	53.41	59.75	68.83	60.05	57.33	31.31	40.17	32.02
Blind1.fs	8.33	8.61	23.14	25.34	36.11	40.49	46.34	55.15	1.11	0.85	0.93	0.95	0.63	0.81	0.84	0.81
c.o.v (%)	0.73	0.61	0.43	0.36	0.45	0.34	0.40	0.23	46.06	81.33	63.41	43.71	55.50	47.62	38.22	30.42
Blind2.fs	8.28	8.68	22.56	25.15	35.18	40.76	45.00	55.43	1.00	1.28	0.62	1.11	0.88	0.89	0.80	0.83
c.o.v (%)	0.80	0.57	0.52	0.42	0.17	0.17	0.34	0.21	50.75	53.90	74.60	41.76	42.61	53.58	50.19	29.60

* W1 and S1 mean the corresponding values for the first mode in the weak and strong directions, respectively.

Table 2. Experimental modal parameters for the braced cases of the partial-sensor scenario in simulated Phase II.

	Frequency (Hz)								Damping ratio (%)							
	W1	S1	W2	S2	W3	S3	W4	S4	W1	S1	W2	S2	W3	S3	W4	S4
RB.ps	8.33	8.75	23.13	25.33	36.12	40.82	46.34	55.44	0.94	1.19	0.90	0.94	0.62	0.67	0.84	0.79
c.o.v (%)	0.82	0.52	0.46	0.37	0.45	0.27	0.40	0.24	55.93	43.84	70.39	42.92	56.99	55.01	37.96	35.77
DP1B.ps	8.33	8.44	23.13	24.56	36.12	40.40	46.33	55.35	1.00	0.76	0.89	0.82	0.62	0.98	0.84	0.82
c.o.v (%)	0.80	0.60	0.46	0.20	0.45	0.34	0.39	0.23	45.84	88.93	71.73	65.29	57.64	33.02	38.32	27.59
DP2B.ps	8.33	8.60	23.13	24.93	36.12	40.62	46.34	55.40	0.95	0.90	0.89	0.94	0.62	0.63	0.84	0.81
c.o.v (%)	0.79	0.73	0.46	0.56	0.45	0.27	0.39	0.22	55.50	80.67	71.08	46.33	57.44	66.58	37.82	29.78
DP3B.ps	8.32	8.37	23.13	24.11	36.11	40.32	46.34	54.65	1.09	1.17	0.89	1.04	0.62	1.04	0.84	1.01
c.o.v (%)	0.69	0.51	0.47	0.37	0.45	0.33	0.39	0.39	43.72	58.70	73.06	46.84	58.27	36.64	38.36	27.47
DP3Bu.ps	8.33	8.54	23.13	24.74	36.11	40.00	46.33	55.06	0.97	1.20	0.90	0.98	0.64	1.34	0.87	0.83
c.o.v (%)	0.77	0.76	0.46	0.49	0.44	0.37	0.38	0.20	58.37	63.30	72.53	59.60	58.18	32.54	39.73	32.44
Blind1.ps	8.33	8.61	23.13	25.34	36.12	40.49	46.34	55.16	0.94	0.76	0.89	0.94	0.62	0.81	0.85	0.80
c.o.v (%)	0.79	0.58	0.46	0.35	0.45	0.34	0.39	0.23	54.92	87.33	71.54	43.97	56.80	49.82	38.06	30.81
Blind2.ps	8.28	8.68	22.57	25.15	35.19	40.76	45.01	55.44	0.95	1.20	0.61	1.09	0.88	0.83	0.82	0.84
c.o.v (%)	0.79	0.61	0.51	0.44	0.17	0.16	0.31	0.21	53.35	55.25	74.40	40.37	45.73	65.57	50.67	32.90

Table 3. Experimental modal parameters for the unbraced cases of the full-sensor scenario in simulated Phase II.

	Frequency (Hz)								Damping ratio (%)							
	W1	S1	W2	S2	W3	S3	W4	S4	W1	S1	W2	S2	W3	S3	W4	S4
RU.fs	3.19	3.98	9.79	13.41	16.66	25.15	23.72	39.28	2.41	1.92	1.39	0.98	1.79	0.94	0.87	1.10
c.o.v (%)	1.72	0.33	0.46	0.29	1.08	0.34	0.37	0.20	51.20	80.09	54.66	67.77	63.64	57.79	43.67	26.13
DP1U.fs	3.20	3.42	9.78	12.91	16.69	24.68	23.72	39.11	2.50	2.09	1.32	1.25	1.05	1.09	0.88	1.07
c.o.v (%)	2.45	0.91	0.60	0.57	0.41	0.39	0.38	0.30	57.46	53.18	49.71	45.05	38.86	47.06	44.56	20.91
DP2U.fs	3.19	3.79	9.79	13.13	16.72	25.15	23.72	39.17	2.89	1.99	1.34	1.37	1.09	0.96	0.87	1.15
c.o.v (%)	2.02	0.57	0.53	0.58	0.45	0.30	0.38	0.28	79.22	69.58	50.21	39.86	41.70	54.61	44.07	20.46
DP1Uu.fs	3.20	3.65	9.79	13.12	16.71	24.88	23.72	39.16	2.88	3.03	1.35	1.66	0.99	1.17	0.88	1.12
c.o.v (%)	2.47	1.03	0.50	0.65	0.53	0.30	0.37	0.32	79.09	51.10	51.05	32.28	46.62	29.82	44.69	18.46

Table 4. Experimental modal parameters for the unbraced cases of the partial-sensor scenario in simulated Phase II.

	Frequency (Hz)								Damping ratio (%)							
	W1	S1	W2	S2	W3	S3	W4	S4	W1	S1	W2	S2	W3	S3	W4	S4
RU.ps	3.18	3.98	9.78	13.40	16.62	25.15	23.72	39.28	2.27	1.74	1.33	0.95	1.61	0.73	0.80	1.09
c.o.v (%)	1.32	0.32	0.56	0.30	1.16	0.38	0.37	0.20	53.94	79.05	60.47	69.79	79.16	81.74	42.73	30.53
DP1U.ps	3.20	3.42	9.78	12.91	16.69	24.67	23.73	39.12	2.26	1.80	1.31	1.19	0.93	0.96	0.81	1.05
c.o.v (%)	2.37	0.99	0.70	0.59	0.43	0.47	0.39	0.33	59.64	47.09	56.20	47.27	63.23	60.44	43.94	23.19
DP2U.ps	3.19	3.79	9.79	13.13	16.72	25.14	23.72	39.19	2.37	1.83	1.35	1.33	0.91	0.81	0.80	1.17
c.o.v (%)	1.91	0.60	0.55	0.59	0.57	0.37	0.39	0.25	62.27	71.39	60.02	38.94	61.11	66.23	43.74	23.30
DP1Uu.ps	3.20	3.65	9.79	13.12	16.71	24.87	23.72	39.15	2.46	2.71	1.34	1.65	0.79	1.00	0.82	1.10
c.o.v (%)	2.26	0.95	0.52	0.66	0.63	0.37	0.38	0.38	66.86	52.52	58.52	32.51	63.24	30.13	44.44	21.41

Table 5. The actual modal parameters for all cases in simulated Phase II.

	Frequency (Hz)								Damping ratio (%)							
	W1	S1	W2	S2	W3	S3	W4	S4	W1	S1	W2	S2	W3	S3	W4	S4
Braced cases																
RB	8.35	8.74	23.15	25.29	36.09	40.78	46.27	55.50	1.00	1.00	1.00	1.00	1.00	1.00	1.00	1.00
DP1B	8.35	8.44	23.15	24.55	36.08	40.33	46.27	55.37	1.00	1.00	1.00	1.00	1.00	1.00	1.00	1.00
DP2B	8.35	8.60	23.15	24.93	36.08	40.55	46.27	55.44	1.00	1.00	1.00	1.00	1.00	1.00	1.00	1.00
DP3B	8.35	8.36	23.15	24.16	36.07	40.30	46.27	54.56	1.00	1.00	1.00	1.00	1.00	1.00	1.00	1.00
DP3Bu	8.35	8.55	23.15	24.72	36.08	40.74	46.27	55.00	1.00	1.00	1.00	1.00	1.00	1.00	1.00	1.00
Unbraced cases																
RU	3.18	3.98	9.79	13.37	16.70	25.12	23.72	39.26	1.00	1.00	1.00	1.00	1.00	1.00	1.00	1.00
DP1U	3.18	3.44	9.79	12.91	16.69	24.67	23.72	39.13	1.00	1.00	1.00	1.00	1.00	1.00	1.00	1.00
DP2U	3.18	3.80	9.79	13.16	16.69	25.11	23.72	39.19	1.00	1.00	1.00	1.00	1.00	1.00	1.00	1.00
DP1Uu	3.18	3.63	9.79	13.13	16.69	24.87	23.72	39.19	1.00	1.00	1.00	1.00	1.00	1.00	1.00	1.00

Table 6. Stiffness ratios for the braced cases of the full-sensor scenario in simulated Phase II.

	$\theta_{1,+x}$	$\theta_{2,+x}$	$\theta_{3,+x}$	$\theta_{4,+x}$	$\theta_{1,+y}$	$\theta_{2,+y}$	$\theta_{3,+y}$	$\theta_{4,+y}$	$\theta_{1,-x}$	$\theta_{2,-x}$	$\theta_{3,-x}$	$\theta_{4,-x}$	$\theta_{1,-y}$	$\theta_{2,-y}$	$\theta_{3,-y}$	$\theta_{4,-y}$	ρ_1	ρ_2	ρ_3	ρ_4
RB.fs	1.00	1.00	1.00	1.00	1.00	1.00	1.00	1.00	1.00	1.00	1.00	1.00	1.00	1.00	1.00	1.00	1.00	1.00	1.00	1.00
c.o.v. (%)	1.28	0.58	1.17	0.45	1.12	0.86	2.20	0.53	1.19	0.59	1.15	0.44	1.11	0.88	2.21	0.54	0.10	0.10	0.10	0.10
DP1B.fs	0.99	1.00	1.01	1.01	**0.89***	1.01	1.01	1.00	1.02	1.00	1.02	1.00	**0.88***	1.01	0.97	1.00	1.00	1.00	1.00	1.00
c.o.v. (%)	1.51	0.68	1.29	0.53	1.38	0.83	2.62	0.53	1.41	0.70	1.27	0.51	1.36	0.86	2.66	0.55	0.10	0.10	0.10	0.10
DP2B.fs	1.00	1.00	1.01	1.00	**0.94***	1.02	1.00	0.99	1.01	1.00	1.02	1.00	**0.92***	1.02	1.00	1.00	1.00	1.00	1.00	1.00
c.o.v. (%)	1.41	0.63	1.28	0.49	1.36	0.93	2.38	0.58	1.32	0.65	1.25	0.47	1.35	0.95	2.37	0.60	0.10	0.10	0.10	0.10
DP3B.fs	0.98	1.00	1.02	1.01	**0.89***	1.01	**0.94***	1.00	1.02	1.01	1.02	0.99	**0.89***	1.00	**0.88***	1.00	1.00	1.00	1.00	1.00
c.o.v. (%)	1.65	0.73	1.33	0.57	1.22	0.76	2.61	0.45	1.54	0.75	1.31	0.55	1.19	0.80	2.67	0.47	0.10	0.10	0.10	0.10
DP3Bu.fs	0.96	1.01	1.01	1.00	0.96	1.02	0.97	0.96*	1.00	1.01	1.02	1.01	**0.80***	0.97	**0.91***	0.97	1.00	1.00	1.00	1.00
c.o.v. (%)	1.97	0.92	1.33	0.75	1.86	1.08	2.62	0.69	1.82	0.94	1.30	0.71	1.66	1.21	2.20	0.83	0.10	0.10	0.10	0.10
Blind1.fs	1.00	1.00	1.02	1.00	0.98	1.02	1.04	0.99	1.00	1.01	1.02	1.00	0.95*	**0.95***	1.05	0.98	1.00	1.00	1.00	1.00
c.o.v. (%)	1.48	0.67	1.25	0.52	1.38	0.97	2.38	0.63	1.38	0.68	1.22	0.50	1.33	1.01	2.37	0.65	0.10	0.10	0.10	0.10
Blind2.fs	1.03	1.01	1.02	**0.82***	0.98	1.02	0.98	1.01	0.94*	1.00	**0.91***	1.00	**0.95***	0.99	1.01	0.99	1.00	1.00	1.00	1.00
c.o.v. (%)	2.15	0.94	1.32	0.80	1.23	0.93	2.35	0.56	1.89	0.99	1.54	0.75	1.26	0.89	2.36	0.54	0.10	0.10	0.10	0.10

Table 7. Stiffness ratios for the braced cases of the partial-sensor scenario in simulated Phase II.

	$\theta_{1,+x}$	$\theta_{2,+x}$	$\theta_{3,+x}$	$\theta_{4,+x}$	$\theta_{1,+y}$	$\theta_{2,+y}$	$\theta_{3,+y}$	$\theta_{4,+y}$	$\theta_{1,-x}$	$\theta_{2,-x}$	$\theta_{3,-x}$	$\theta_{4,-x}$	$\theta_{1,-y}$	$\theta_{2,-y}$	$\theta_{3,-y}$	$\theta_{4,-y}$	ρ_1	ρ_2	ρ_3	ρ_4
RB.ps	1.00	1.00	1.00	1.00	1.00	1.00	1.00	1.00	1.00	1.00	1.00	1.00	1.00	1.00	1.00	1.00	1.00	1.00	1.00	1.00
c.o.v. (%)	1.45	1.13	0.49	0.74	1.48	0.72	0.93	2.78	1.46	1.12	0.48	0.75	1.54	0.81	1.06	2.73	0.10	0.10	0.10	0.10
DP1B.ps	0.98	0.99	0.99	1.01	**0.90***	0.99	1.00	1.01	1.02	1.02	1.01	0.99	**0.92***	1.00	0.98	1.01	1.00	1.00	1.00	1.00
c.o.v. (%)	1.22	0.98	0.51	0.72	1.50	0.75	0.90	2.60	1.25	0.97	0.49	0.72	1.55	0.82	1.06	2.50	0.10	0.10	0.10	0.10
DP2B.ps	0.99	0.99	0.99	1.00	**0.93***	1.02	0.98	1.02	1.00	1.02	1.01	0.99	**0.96***	1.02	0.97	1.02	1.00	1.00	1.00	1.00
c.o.v. (%)	1.28	1.04	0.48	0.71	1.25	0.63	0.88	2.30	1.30	1.02	0.47	0.71	1.30	0.72	1.03	2.24	0.10	0.10	0.10	0.10
DP3B.ps	0.96*	1.02	0.99	1.00	**0.85***	1.02	**0.94***	0.99	0.99	1.02	1.00	0.97	**0.89***	1.02	**0.91***	1.00	1.00	1.00	1.00	1.00
c.o.v. (%)	1.01	0.97	0.57	0.71	1.07	0.63	0.99	2.58	1.03	0.97	0.55	0.68	1.10	0.70	1.16	2.47	0.10	0.10	0.10	0.10
DP3Bu.ps	0.98	1.02	0.99	1.02	1.02	1.02	1.02	0.92*	0.97	1.02	0.99	0.95*	**0.83***	1.02	**0.92***	1.02	1.00	1.00	1.00	1.00
c.o.v. (%)	1.15	1.23	0.75	0.81	1.29	0.86	1.08	2.46	1.17	1.23	0.72	0.75	1.23	0.62	1.23	2.40	0.10	0.10	0.10	0.10
Blind1.ps	1.00	1.00	1.00	1.00	0.99	0.99	1.00	0.98	1.00	1.01	1.00	1.00	0.93*	**0.95***	0.99	1.01	1.00	1.00	1.00	1.00
c.o.v. (%)	1.39	1.08	0.51	0.72	1.57	0.80	0.99	2.66	1.41	1.07	0.49	0.72	1.59	0.86	1.03	2.70	0.10	0.10	0.10	0.10
Blind2.ps	1.02	0.99	0.98	**0.78***	1.02	1.02	1.00	0.98	0.96*	1.02	**0.88***	1.02	**0.90***	1.02	0.97	1.02	1.00	1.00	1.00	1.00
c.o.v. (%)	1.31	1.30	0.61	0.78	1.16	0.83	1.12	2.35	1.27	1.25	0.74	0.82	1.15	0.75	1.18	2.23	0.10	0.10	0.10	0.10

Table 8. Stiffness ratios for the unbraced cases of the full-sensor scenario in simulated Phase II.

	$\theta_{c,x}$	$\theta_{c,y}$	$\theta_{1,x}$	$\theta_{2,x}$	$\theta_{3,x}$	$\theta_{4,x}$	$\theta_{1,y}$	$\theta_{2,y}$	$\theta_{3,y}$	$\theta_{4,y}$	ρ_1	ρ_2	ρ_3	ρ_4
RU.fs	1.00	1.00	1.00	1.00	1.00	1.00	1.00	1.00	1.00	1.00	1.00	1.00	1.00	1.00
c.o.v.(%)	0.13	0.28	3.15	3.27	1.54	4.14	3.06	1.93	1.75	0.10	0.10	0.10	0.10	0.10
DP1U.fs	1.00	1.00	1.03	1.02	0.97	1.04	**0.35***	**0.60***	0.91*	1.04	1.00	1.00	1.00	1.00
c.o.v.(%)	0.15	0.26	2.92	2.76	1.47	3.75	7.89	3.19	1.97	0.10	0.10	0.10	0.10	0.10
DP2U.fs	1.00	1.00	1.00	1.03	0.98	1.07	**0.68***	0.94	0.90*	1.04	1.00	1.00	1.00	1.00
c.o.v.(%)	0.15	0.28	2.93	2.87	1.44	4.00	4.27	2.28	1.95	0.10	0.10	0.10	0.10	0.10
DP1Uu.fs	1.00	1.00	1.01	1.04	0.98	1.05	**0.60***	**0.74***	0.93	1.04	1.00	1.00	1.00	1.00
c.o.v.(%)	0.18	0.29	3.07	2.96	1.49	4.08	6.42	3.37	2.50	0.10	0.10	0.10	0.10	0.10

Table 9. Stiffness ratios for the unbraced cases of the partial-sensor scenario in simulated Phase II.

	$\theta_{c,x}$	$\theta_{c,y}$	$\theta_{1,x}$	$\theta_{2,x}$	$\theta_{3,x}$	$\theta_{4,x}$	$\theta_{1,y}$	$\theta_{2,y}$	$\theta_{3,y}$	$\theta_{4,y}$	ρ_1	ρ_2	ρ_3	ρ_4
RU.ps	1.00	1.00	1.00	1.00	1.00	1.00	1.00	1.00	1.00	1.00	1.00	1.00	1.00	1.00
c.o.v.(%)	0.14	0.30	3.42	3.21	1.42	4.36	2.76	1.80	1.95	0.10	0.10	0.10	0.10	0.10
DP1U.ps	1.00	1.00	1.01	1.06	0.96	1.09	**0.46***	**0.56***	0.95	1.01	1.00	1.00	1.00	1.00
c.o.v.(%)	0.21	0.30	2.97	2.56	1.37	4.13	6.95	4.56	2.95	0.10	0.10	0.10	0.10	0.10
DP2U.ps	1.00	1.00	0.98	1.06	0.98	1.09	**0.74***	0.92*	0.91*	1.04	1.00	1.00	1.00	1.00
c.o.v.(%)	0.17	0.29	2.85	2.57	1.23	4.03	3.92	2.47	2.43	0.10	0.10	0.10	0.10	0.10
DP1Uu.ps	1.00	1.00	1.00	1.06	0.97	1.09	**0.71***	**0.69***	0.94	1.04	1.00	1.00	1.00	1.00
c.o.v.(%)	0.20	0.30	3.03	2.69	1.29	4.25	4.08	2.82	2.39	0.10	0.10	0.10	0.10	0.10

Table 10. Experimental modal parameters for the hammer cases in experimental Phase II.

	Frequency (Hz)					Damping ratio (%)				
	W1	S1	T1*	W2	S2	W1	S1	T1	W2	S2
Config1.h	7.45	7.67	14.45	19.84	20.87	0.73	0.78	0.46	0.32	0.42
c.o.v (%)	0.02	0.05	0.01	0.01	0.04	7.80	0.87	5.42	7.38	1.44
Config2.h	7.68	5.12	12.69	19.99	14.92	0.66	0.88	0.38	0.37	0.48
c.o.v (%)	0.04	0.06	0.02	0.02	0.03	2.47	2.29	1.78	2.14	0.15
Config3.h	7.56	6.52	13.40	19.91	18.78	0.69	0.79	0.34	0.39	0.46
c.o.v (%)	0.01	0.08	0.00	0.02	0.07	1.57	2.09	1.11	1.96	5.19
Config4.h	7.56	7.26	13.95	20.05	19.67	0.70	0.65	0.37	0.56	0.32
c.o.v (%)	0.02	0.03	0.01	0.10	0.01	0.53	0.72	4.26	25.74	0.51
Config5.h	7.55	7.37	13.99	19.84	20.48	0.64	0.65	0.33	0.31	0.39
c.o.v (%)	0.07	0.01	0.02	0.05	0.01	5.33	1.48	1.75	6.71	4.27
Config6.h	5.93	7.68	13.07	19.81	20.80	0.60	0.82	0.43	0.32	0.47
c.o.v (%)	0.05	0.04	0.02	0.02	0.04	5.14	1.11	1.81	4.44	3.17

*T1 means the corresponding values for the first mode in torsion.

	Frequency (Hz)								Damping ratio (%)							
	W1	S1	T1	W2	S2	T2	W3	S3	W1	S1	T1	W2	S2	T2	W3	S3
Config7.h	2.62	3.60	4.31	8.44	11.94	13.88	16.16	21.58	0.92	0.94	0.77	0.44	0.51	0.51	0.30	0.38
c.o.v (%)	0.08	0.05	0.02	0.02	0.04	0.01	0.01	0.03	6.69	2.78	1.96	0.83	0.18	1.95	3.42	2.03
Config8.h	2.54	3.24	4.10	8.28	11.03	13.28	15.92	20.61	0.90	1.06	0.80	0.45	0.59	0.46	0.31	0.59
c.o.v (%)	0.01	0.06	0.03	0.03	0.16	0.04	0.03	0.06	3.91	1.01	2.01	1.81	2.56	0.68	1.59	1.75
Config9.h	2.56	3.35	4.15	8.38	11.67	13.60	16.05	21.08	0.96	1.09	0.86	0.45	0.55	0.53	0.32	0.65
c.o.v (%)	0.06	0.14	0.04	0.01	0.03	0.02	0.01	0.04	3.13	5.15	1.29	0.31	1.85	0.62	0.30	0.69

Table 11. Experimental modal parameters for the ambient-vibration cases in experimental Phase II.

	Frequency (Hz)					Damping ratio (%)				
	W1	S1	T1	W2	S2	W1	S1	T1	W2	S2
Config1.a	7.48	7.76	14.48	19.89	21.01	0.60	0.37	0.06	0.01	0.01
c.o.v (%)	0.29	0.16	0.04	0.00	0.01	0.25	116.28	59.97	1.19	8.30
Config2.a	7.73	5.19	12.74	20.12	15.02	0.50	0.36	0.11	0.18	0.16
c.o.v (%)	0.11	0.17	0.13	0.25	0.04	47.50	34.48	98.65	51.07	48.86
Config3.a	7.63	6.65	13.44	20.03	18.87	0.32	0.15	0.07	0.17	0.03
c.o.v (%)	0.28	0.03	0.03	0.03	0.02	93.38	90.38	51.06	157.26	28.76
Config4.a	7.60	7.36	13.98	20.11	19.68	0.35	0.29	0.03	0.08	0.39
c.o.v (%)	0.16	0.26	0.07	0.04	0.14	9.96	135.73	20.80	74.71	110.68
Config5.a	7.61	7.46	14.02	19.89	20.00	1.00	0.27	0.08	0.01	2.85
c.o.v (%)	0.27	0.25	0.15	0.02	0.18	0.08	44.45	51.94	1.43	12.71
Config6.a	5.97	7.77	13.20	19.89	21.00	0.10	0.43	0.20	0.02	0.04
c.o.v (%)	0.15	0.53	0.28	0.01	0.00	15.08	28.11	129.57	1.69	52.63

Table 12. Experimental modal parameters for the shaker cases in experimental Phase II.

	Frequency (Hz)					Damping ratio (%)				
	W1	S1	T1	W2	S2	W1	S1	T1	W2	S2
Config1.s	7.45	7.78	14.49	20.97	19.88	1.00	0.10	0.13	0.08	0.14
c.o.v (%)	0.02	0.41	0.15	0.07	0.10	0.08	2.84	58.24	0.36	50.21
Config2.s	7.72	5.17	12.77	20.09	15.02	1.00	1.00	0.22	0.16	0.36
c.o.v (%)	0.02	0.05	0.05	0.24	0.12	0.15	0.22	56.92	59.39	26.23
Config3.s	7.64	6.60	13.46	20.02	18.96	1.06	1.04	0.07	0.08	0.10
c.o.v (%)	0.04	0.05	0.03	0.04	0.04	3.27	2.86	13.35	16.46	51.02
Config4.s	7.56	7.30	13.97	19.72	19.71	1.00	0.10	0.10	0.26	0.22
c.o.v (%)	0.42	0.09	0.12	0.07	0.03	0.15	2.49	22.66	63.82	54.72
Config5.s	7.57	7.44	14.03	20.60	19.90	1.00	1.00	0.13	1.00	0.21
c.o.v (%)	0.13	0.22	0.04	0.00	0.18	0.04	0.42	34.86	0.03	106.87
Config6.s	5.96	7.78	13.14	19.87	20.96	0.12	1.02	0.08	0.18	0.23
c.o.v (%)	0.09	0.39	0.02	0.12	0.05	23.45	21.25	10.48	112.89	128.10

Table 13. Stiffness ratios for the braced hammer cases in experimental Phase II.

	$\theta_{1,+x}$	$\theta_{2,+x}$	$\theta_{3,+x}$	$\theta_{4,+x}$	$\theta_{1,+y}$	$\theta_{2,+y}$	$\theta_{3,+y}$	$\theta_{4,+y}$	$\theta_{1,-x}$	$\theta_{2,-x}$	$\theta_{3,-x}$	$\theta_{4,-x}$	$\theta_{1,-y}$	$\theta_{2,-y}$	$\theta_{3,-y}$	$\theta_{4,-y}$	ρ_1	ρ_2	ρ_3	ρ_4
Config1.h	1.00	1.00	1.00	1.00	1.00	1.00	1.00	1.00	1.00	1.00	1.00	1.00	1.00	1.00	1.00	1.00	1.00	1.00	1.00	1.00
c.o.v. (%)	2.86	8.02	2.37	2.74	9.61	9.36	6.87	8.76	2.79	7.71	2.52	2.95	8.45	10.25	7.93	10.54	0.10	0.10	0.10	0.10
Config2.h	1.03	0.88	0.96	1.03	1.19	0.95	1.03	1.01	1.06	0.90	0.96	0.98	**0.16***	**0.26***	**0.25***	**0.12***	1.00	1.00	1.00	1.00
c.o.v. (%)	1.94	4.78	1.50	1.82	9.36	9.63	9.32	10.63	1.91	4.86	1.60	1.88	43.75	29.71	24.32	47.59	0.10	0.10	0.10	0.10
Config3.h	1.06	0.94	0.95	0.94	1.19	0.95	1.14	1.03	1.06	1.07	0.95	0.92	**0.55***	**0.71***	**0.49***	**0.53***	1.00	1.00	1.00	1.00
c.o.v. (%)	2.50	8.01	1.87	2.02	6.02	8.23	4.24	4.93	2.38	7.18	1.98	2.14	6.84	12.69	5.98	6.65	0.10	0.10	0.10	0.10
Config4.h	1.06	1.12	1.01	1.01	1.19	0.90	1.03	1.08	1.05	1.08	1.01	0.94	**0.57***	1.20	0.98	**0.61***	1.00	1.00	1.00	1.00
c.o.v. (%)	2.51	9.44	1.93	2.17	8.66	9.47	6.54	6.92	2.29	8.29	2.00	2.24	10.37	9.34	6.72	8.55	0.10	0.10	0.10	0.10
Config5.h	1.01	0.92	0.96	1.01	1.19	0.93	1.00	1.01	1.02	1.02	0.96	0.98	**0.59***	0.96	0.97	0.97	1.00	1.00	1.00	1.00
c.o.v. (%)	3.66	9.52	3.09	3.59	8.06	8.82	6.71	8.48	3.57	7.92	3.32	3.97	10.96	9.52	7.06	9.54	0.10	0.10	0.10	0.10
Config6.h	1.06	**0.63***	0.95	0.99	0.97	0.85	0.94	0.92	1.06	1.15	0.92	0.93	1.03	0.89	0.96	0.99	1.00	1.00	1.00	1.00
c.o.v. (%)	2.42	11.94	1.83	2.05	11.26	11.78	8.48	10.43	2.36	8.35	2.08	2.31	10.56	11.96	10.30	14.01	0.10	0.10	0.10	0.10

Table 14. Stiffness ratios for the braced ambient-vibration cases in experimental Phase II.

	$\theta_{1,+x}$	$\theta_{2,+x}$	$\theta_{3,+x}$	$\theta_{4,+x}$	$\theta_{1,+y}$	$\theta_{2,+y}$	$\theta_{3,+y}$	$\theta_{4,+y}$	$\theta_{1,-x}$	$\theta_{2,-x}$	$\theta_{3,-x}$	$\theta_{4,-x}$	$\theta_{1,-y}$	$\theta_{2,-y}$	$\theta_{3,-y}$	$\theta_{4,-y}$	ρ_1	ρ_2	ρ_3	ρ_4
Config1.a	1.00	1.00	1.00	1.00	1.00	1.00	1.00	1.00	1.00	1.00	1.00	1.00	1.00	1.00	1.00	1.00	1.00	1.00	1.00	1.00
c.o.v. (%)	2.56	5.21	2.13	2.39	13.99	13.83	7.08	8.89	2.59	5.14	2.24	2.55	11.17	18.40	8.73	10.12	0.10	0.10	0.10	0.10
Config2.a	1.05	0.89	0.98	0.98	1.28	1.06	1.14	1.18	1.05	0.82*	0.97	0.94	**0.30***	**0.52***	**0.35***	**0.19***	1.00	1.00	1.00	1.00
c.o.v. (%)	2.63	5.08	2.04	2.40	12.17	10.66	10.86	13.97	2.69	5.16	2.12	2.43	34.84	20.49	22.71	34.20	0.10	0.10	0.10	0.10
Config3.a	1.05	0.83*	0.95	0.94	1.28	1.13	1.14	1.18	1.05	0.56*	0.97	0.94	**0.65***	**0.50***	**0.47***	**0.51***	1.00	1.00	1.00	1.00
c.o.v. (%)	3.11	7.25	2.19	2.33	5.87	6.18	3.92	4.93	2.92	8.95	2.14	2.36	6.50	13.17	5.92	6.41	0.10	0.10	0.10	0.10
Config4.a	1.05	0.88	0.96	0.97	1.28	1.08	0.97	1.18	1.05	0.56*	0.97	0.90	**0.66***	1.13	0.93	**0.56***	1.00	1.00	1.00	1.00
c.o.v. (%)	4.00	6.46	2.88	3.28	6.61	7.16	5.02	5.45	3.81	8.60	2.90	3.36	8.32	8.86	5.11	6.60	0.10	0.10	0.10	0.10
Config5.a	1.03	1.10	0.90	0.94	0.97	0.78	0.74*	0.76*	1.05	0.94	1.03	1.04	**0.55***	0.78	1.17	1.13	1.00	1.00	1.00	1.00
c.o.v. (%)	3.07	13.56	2.84	3.03	5.22	7.48	4.16	5.18	3.08	11.50	2.67	3.05	8.43	8.44	4.07	4.74	0.10	0.10	0.10	0.10
Config6.a	1.05	**0.76***	0.96	0.96	1.06	0.81	0.89	0.84	1.05	0.69*	0.99	0.97	1.07	0.94	1.17	0.87	1.00	1.00	1.00	1.00
c.o.v. (%)	2.38	7.89	1.89	2.08	6.61	6.32	6.34	8.74	2.42	9.84	2.05	2.23	6.89	6.59	6.87	10.23	0.10	0.10	0.10	0.10

Table 15. Stiffness ratios for the braced shaker cases in experimental Phase II.

	$\theta_{1,+x}$	$\theta_{2,+x}$	$\theta_{3,+x}$	$\theta_{4,+x}$	$\theta_{1,+y}$	$\theta_{2,+y}$	$\theta_{3,+y}$	$\theta_{4,+y}$	$\theta_{1,-x}$	$\theta_{2,-x}$	$\theta_{3,-x}$	$\theta_{4,-x}$	$\theta_{1,-y}$	$\theta_{2,-y}$	$\theta_{3,-y}$	$\theta_{4,-y}$	ρ_1	ρ_2	ρ_3	ρ_4
Config1.s	1.00	1.00	1.00	1.00	1.00	1.00	1.00	1.00	1.00	1.00	1.00	1.00	1.00	1.00	1.00	1.00	1.00	1.00	1.00	1.00
c.o.v. (%)	2.49	11.12	2.26	2.25	7.90	10.08	4.54	5.54	2.39	11.71	2.12	2.32	6.64	13.69	5.59	6.96	0.10	0.10	0.10	0.10
Config2.s	0.43*	0.82	0.32*	0.10*	1.16	0.98	1.09	0.76*	0.27*	0.36*	0.53*	0.15*	**0.50***	0.97	**0.35***	**0.44***	1.00	1.00	1.00	1.00
c.o.v. (%)	7.81	3.56	18.47	36.36	7.35	4.05	4.80	6.20	13.94	27.71	12.82	30.07	3.90	6.23	6.22	4.12	0.10	0.10	0.10	0.10
Config3.s	0.75*	0.70	0.68*	0.37*	1.16	1.20	1.09	0.86	0.78*	0.64*	0.73*	0.07*	**0.67***	0.73	**0.65***	**0.85***	1.00	1.00	1.00	1.00
c.o.v. (%)	7.69	17.19	9.73	12.17	5.36	8.49	3.46	4.22	12.13	18.96	13.43	70.16	5.52	19.74	4.16	3.62	0.10	0.10	0.10	0.10
Config4.s	0.75*	0.61*	0.73*	0.23*	0.97	1.08	0.83	0.83	0.89	0.75	0.96	0.14*	**0.66***	1.27	1.11	**0.66***	1.00	1.00	1.00	1.00
c.o.v. (%)	10.78	16.78	13.71	14.21	14.37	11.62	12.43	13.85	10.53	15.72	12.21	25.14	18.48	14.94	14.76	15.87	0.10	0.10	0.10	0.10
Config5.s	0.90	0.54*	0.99	0.98	1.00	1.15	0.96	0.97	1.01	0.94	0.99	0.97	**0.59***	1.16	1.11	1.03	1.00	1.00	1.00	1.00
c.o.v. (%)	4.28	19.62	3.89	4.40	9.70	9.10	6.57	8.13	4.24	13.43	3.98	4.79	14.26	12.36	7.80	10.05	0.10	0.10	0.10	0.10
Config6.s	0.97	**0.38***	1.05	1.02	0.89	1.07	1.03	0.86	1.05	0.74	0.96	0.97	0.96	1.19	1.08	0.95	1.00	1.00	1.00	1.00
c.o.v. (%)	2.81	10.87	2.02	2.16	12.40	9.49	7.14	9.30	2.73	8.87	2.36	2.42	11.75	10.26	9.09	12.69	0.10	0.10	0.10	0.10

Table 16. Stiffness ratios for the unbraced hammer cases in experimental Phase II.

Damage Pattern	$\theta_{c,x}$	$\theta_{c,y}$	$\theta_{1,x}$	$\theta_{2,x}$	$\theta_{3,x}$	$\theta_{4,x}$	$\theta_{1,y}$	$\theta_{2,y}$	$\theta_{3,y}$	$\theta_{4,y}$	ρ_1	ρ_2	ρ_3	ρ_4
Config7.h	1.00	1.00	1.00	1.00	1.00	1.00	1.00	1.00	1.00	1.00	1.00	1.00	1.00	1.00
c.o.v.(%)	0.11	0.09	0.40	0.50	0.37	0.79	0.41	0.37	0.33	0.46	0.10	0.10	0.10	0.10
Config8.h	0.99	0.97*	0.87*	1.01	0.78*	0.62*	**0.65***	**0.52***	**0.52***	0.97	1.00	1.00	1.00	1.00
c.o.v.(%)	0.06	0.19	0.09	0.10	0.15	0.40	13.44	2.99	7.77	1.85	0.10	0.10	0.10	0.10
Config9.h	0.97*	0.98*	0.94*	1.01	0.82*	0.86*	**0.84***	**0.72***	0.87*	0.99	1.00	1.00	1.00	1.00
c.o.v.(%)	0.16	0.13	0.40	0.45	0.75	1.88	0.63	0.67	0.98	0.72	0.10	0.10	0.10	0.10

Figure 1. The UBC steel-frame scale-model structure for the benchmark studies.

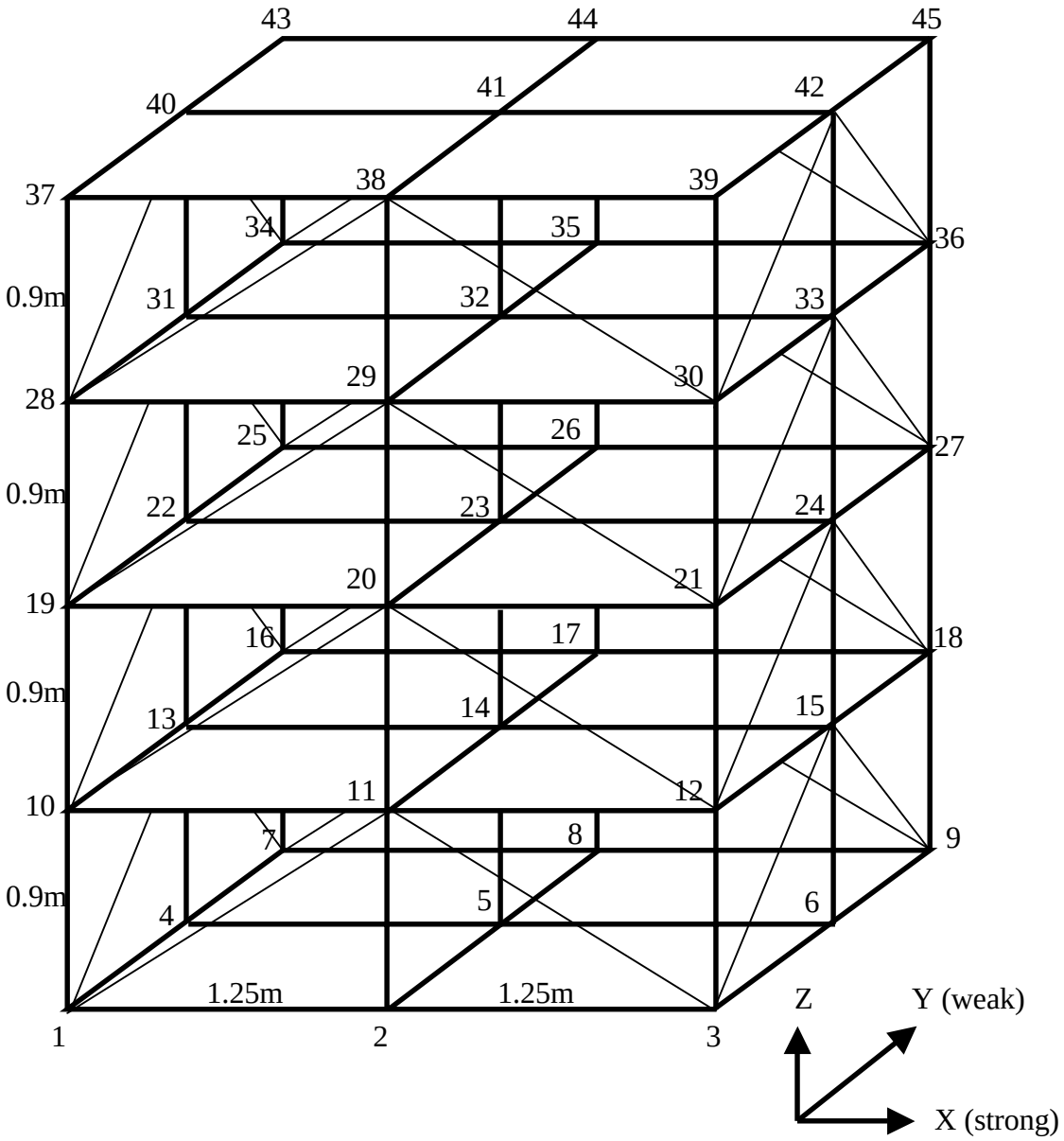

Figure 2. The diagram of the benchmark structure.

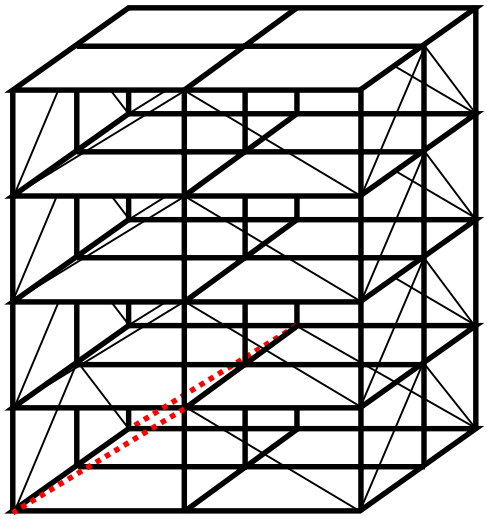

Figure 3a. Damage pattern for DP1B and DP2B.

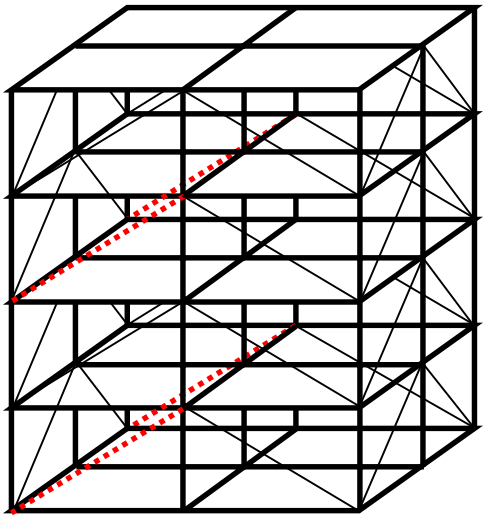

Figure 3b. Damage pattern for DP3B.

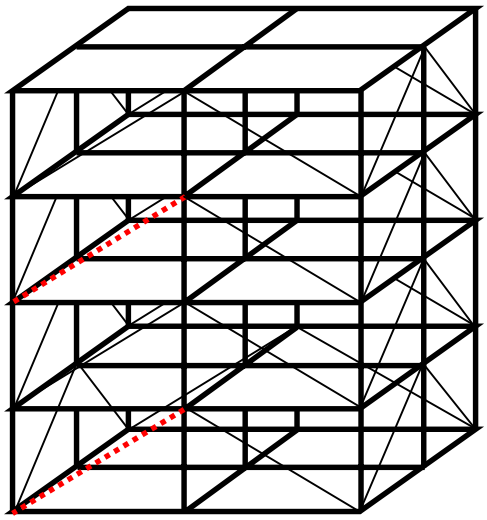

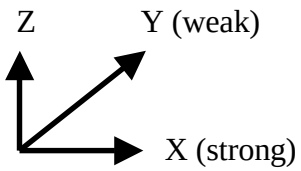

Figure 3c. Damage pattern for DP3Bu.

Figure 3. Damaged braces for DP1B, DP2B, DP3B, and DP3Bu.

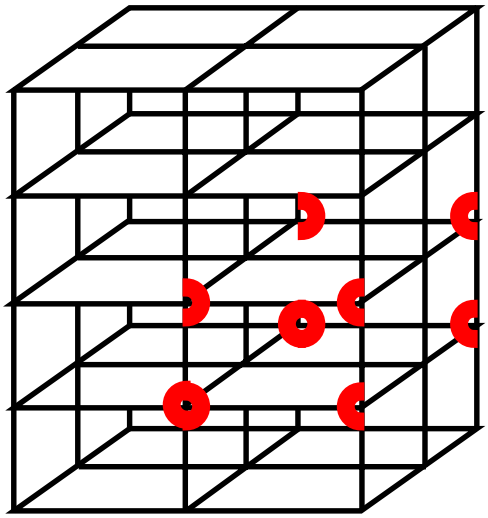

Figure 4a. Damage pattern for DP1U.

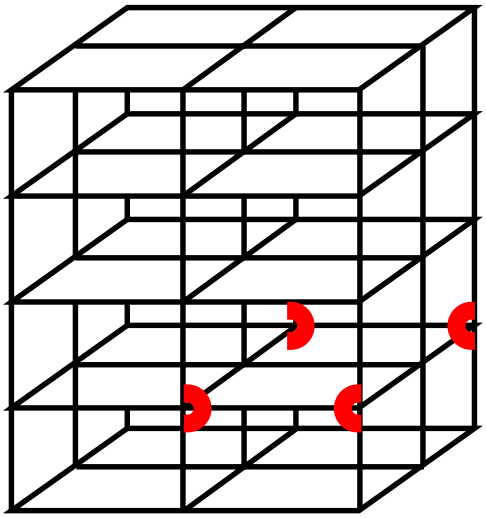

Figure 4b. Damage pattern for DP2U.

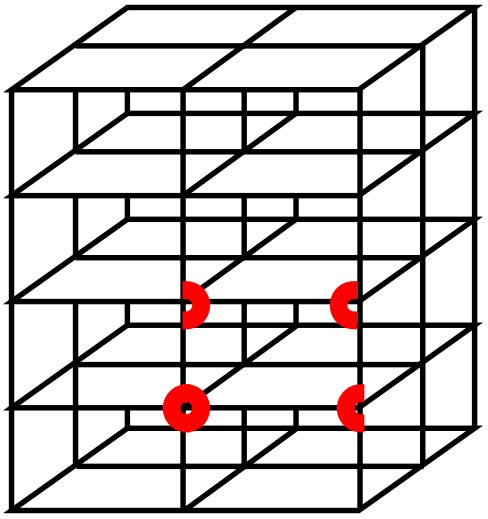

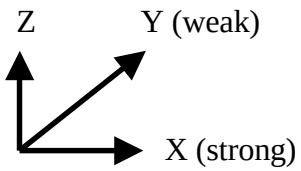

Figure 4c. Damage pattern for DP1Uu.

Figure 4. Damaged patterns for DP1U, DP2U, and DP1Uu.

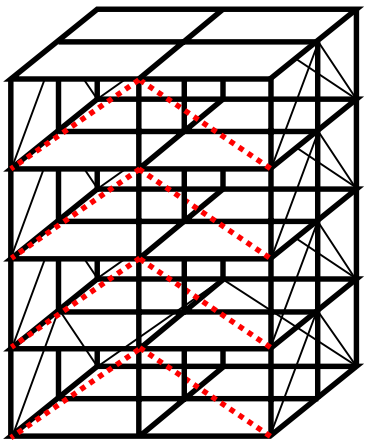

Figure 5a. Config 2.

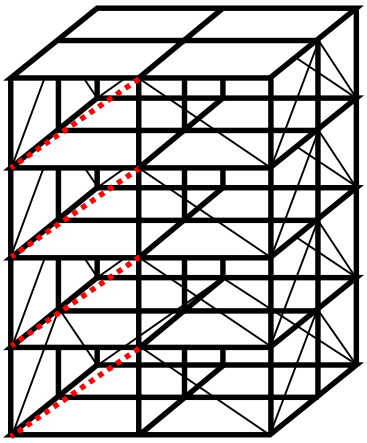

Figure 5b. Config 3.

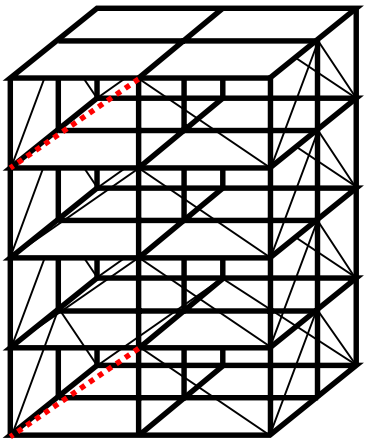

Figure 5c. Config 4.

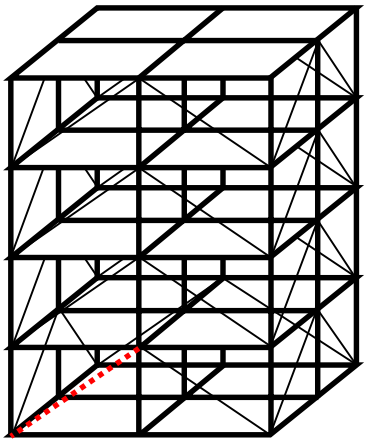

Figure 5d. Config 5.

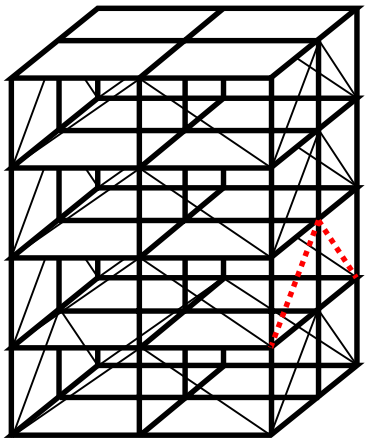

Figure 5e. Config 6.

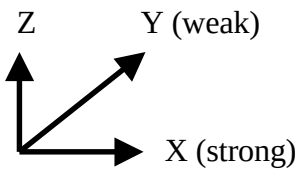

Figure 5. Damaged patterns for Configs 2-6.

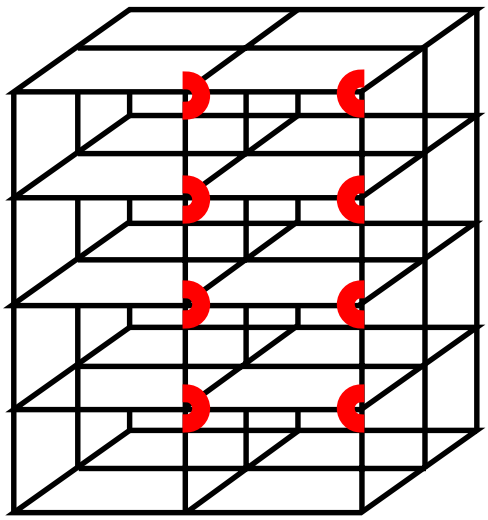

Figure 6a. Damage pattern for Config 8.

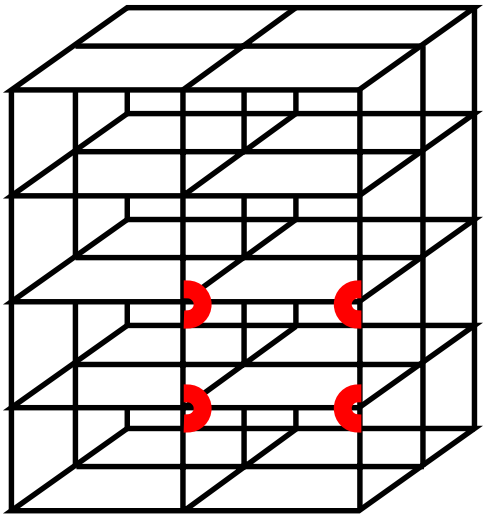

Figure 6b. Damage pattern for Config 9.

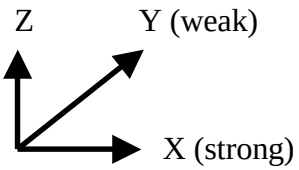

Figure 6. Damaged patterns for Configs 8-9.

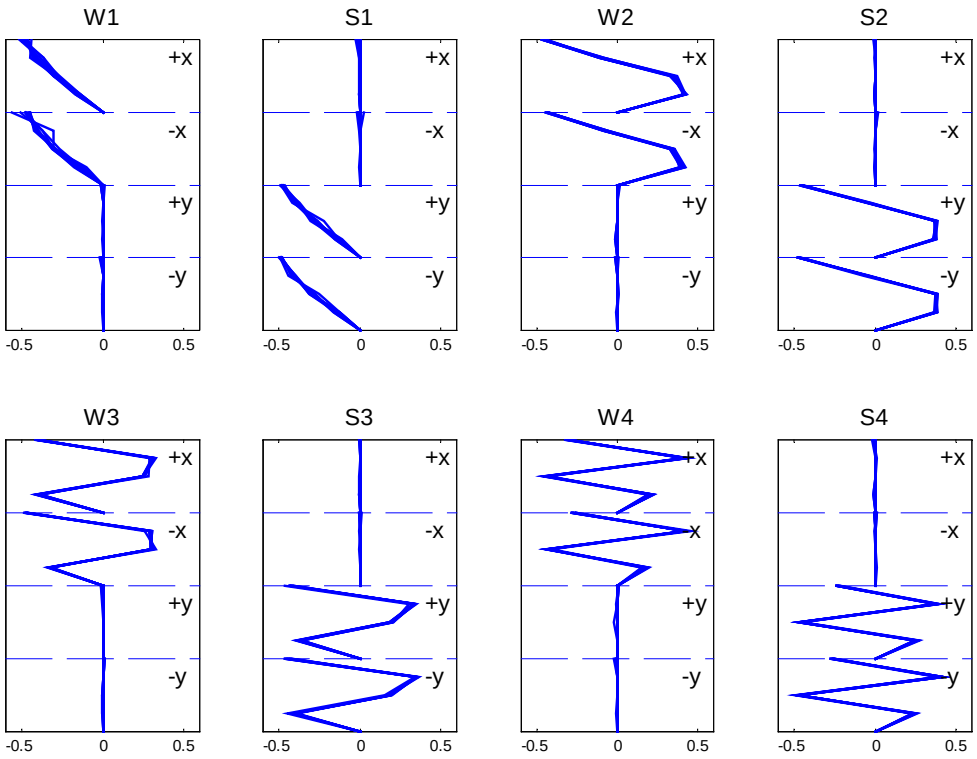

Figure 7. The experimental modeshape components of the structure for the RB.fs case.

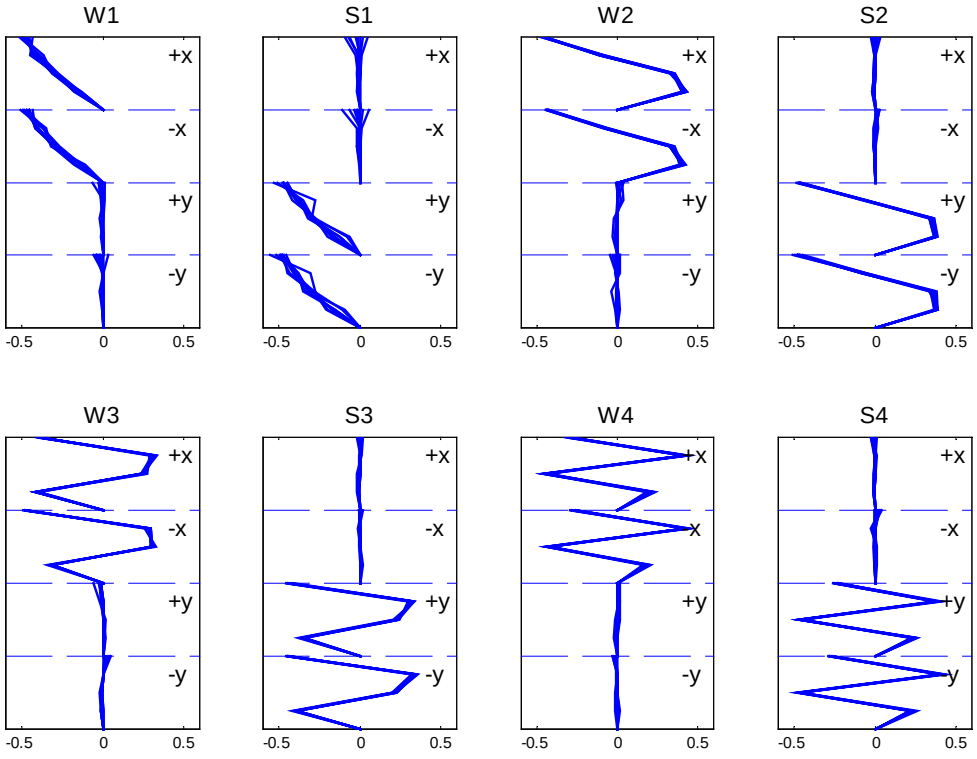

Figure 8. The experimental modeshape components of the structure for the DP1B.fs case.

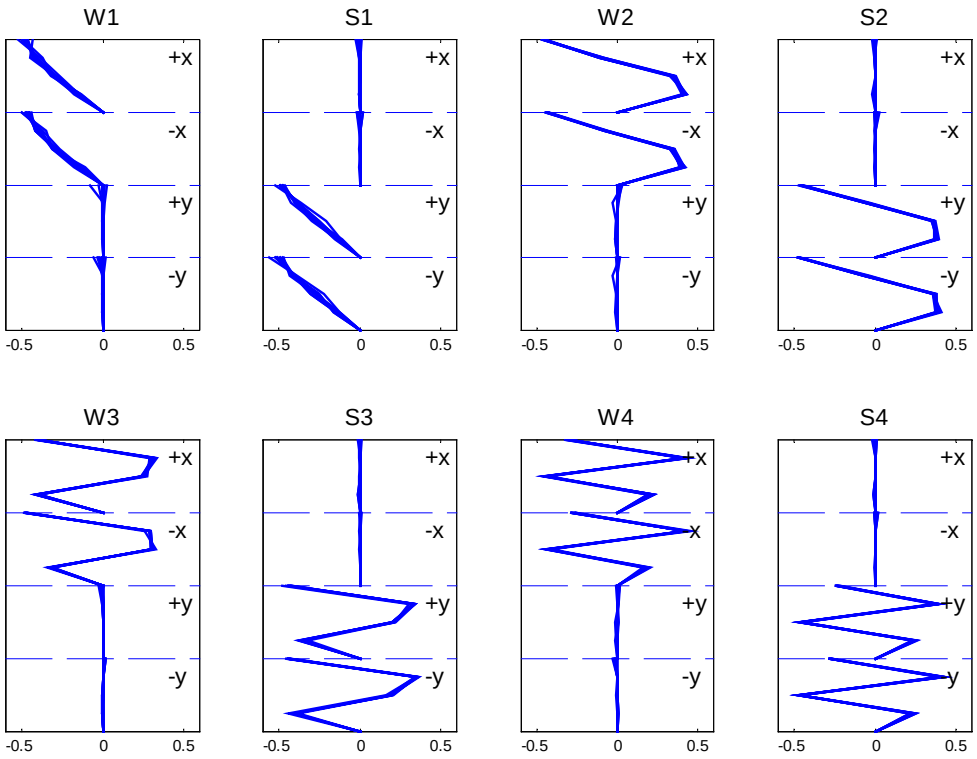

Figure 9. The experimental modeshape components of the structure for the DP2B.fs case.

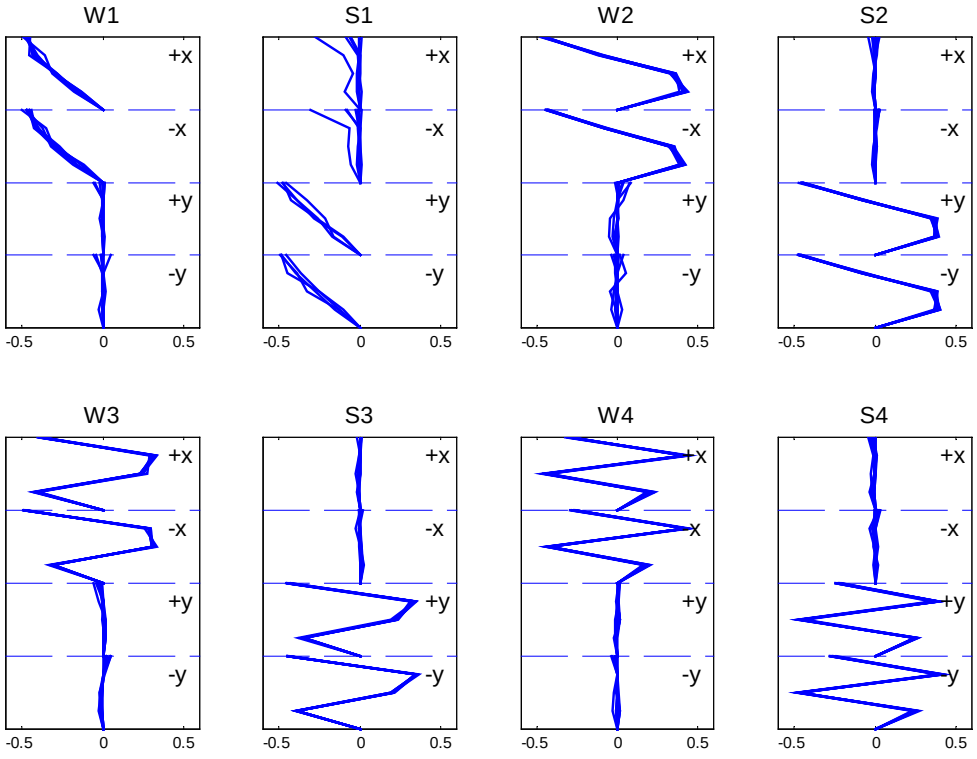

Figure 10. The experimental modeshape components of the structure for the DP3B.fs case.

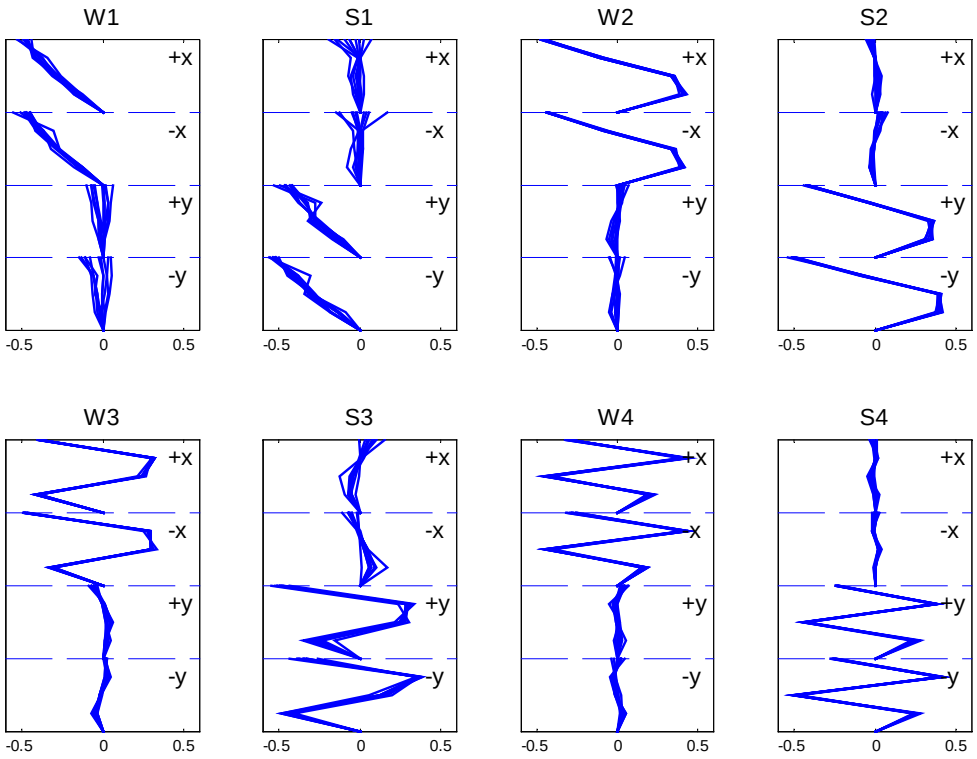

Figure 11. The experimental modeshape components of the structure for the DP3Bu.fs case.

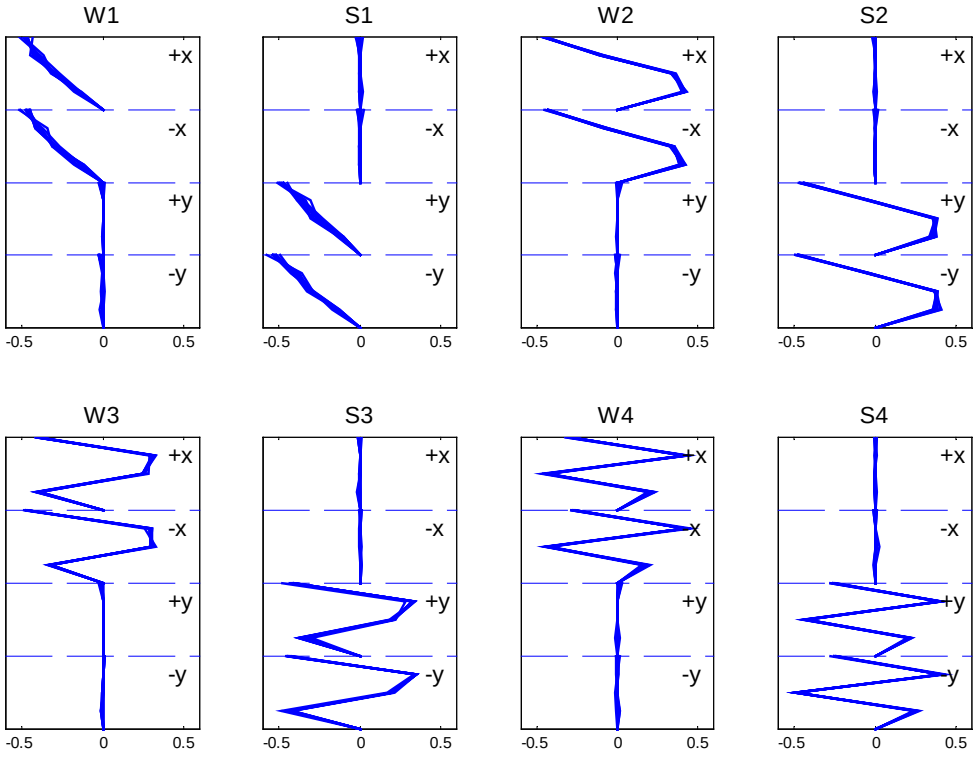

Figure 12. The experimental modeshape components of the structure for the Blind1.fs case.

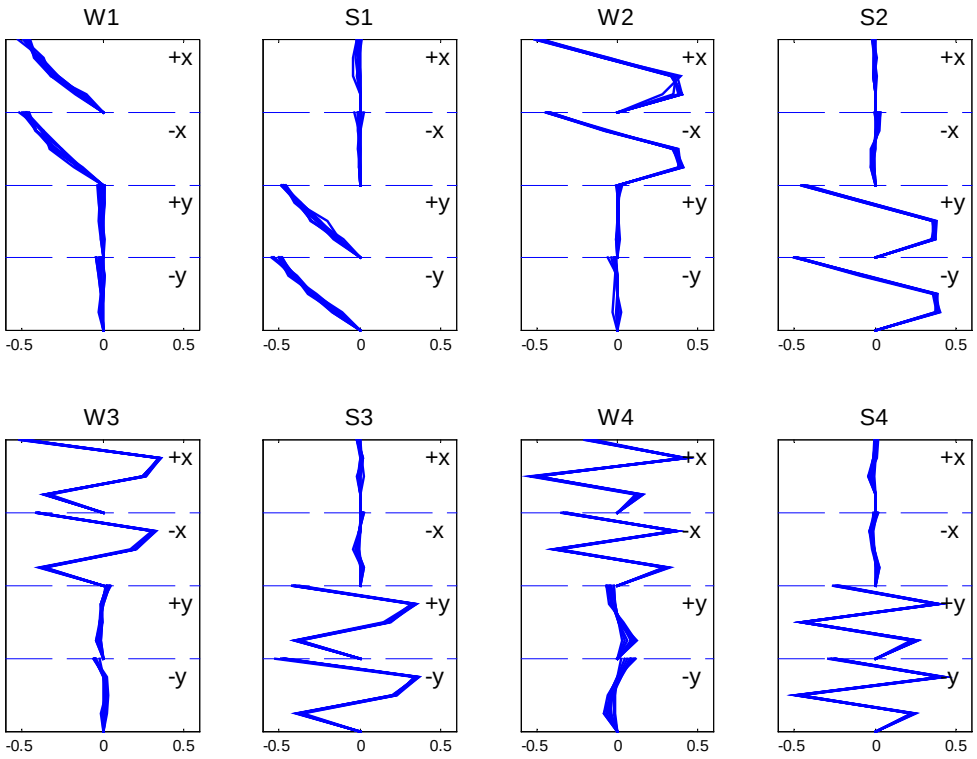

Figure 13. The experimental modeshape components of the structure for the Blind2.fs case.

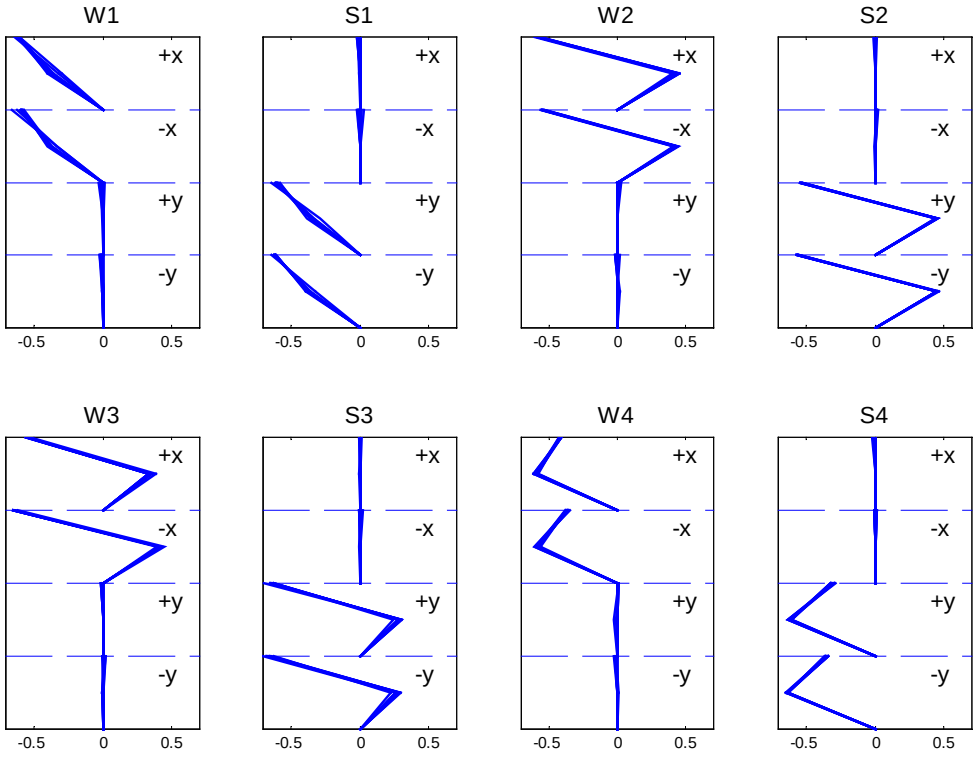

Figure 14. The experimental modeshape components of the structure for the RB.ps case.

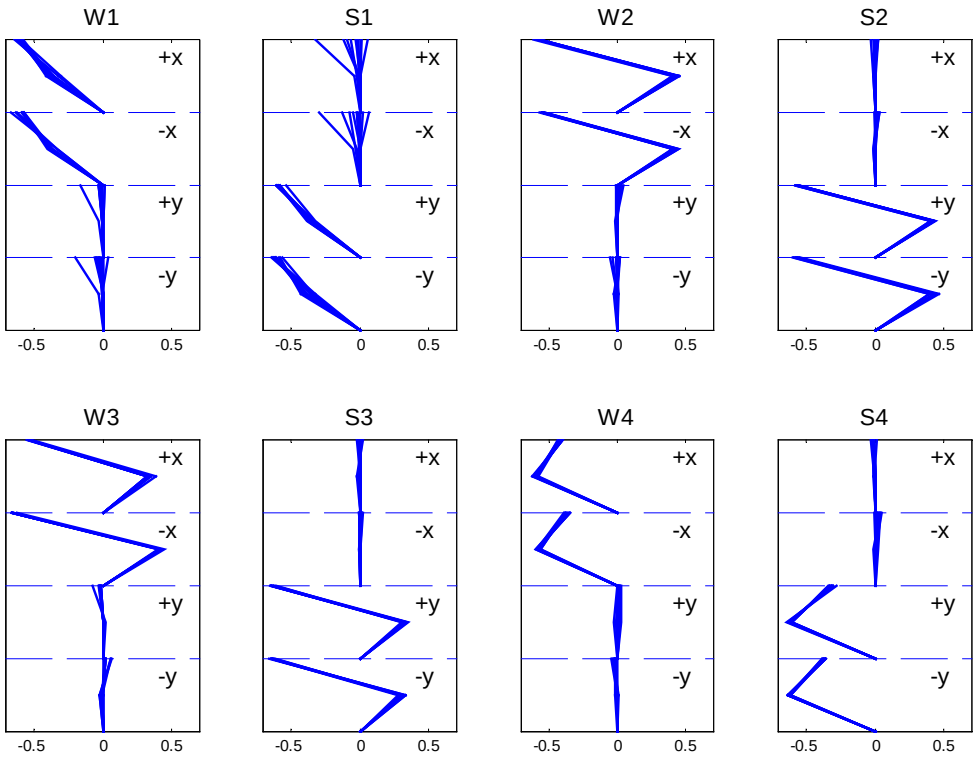

Figure 15. The experimental modeshape components of the structure for the DP1B.ps case.

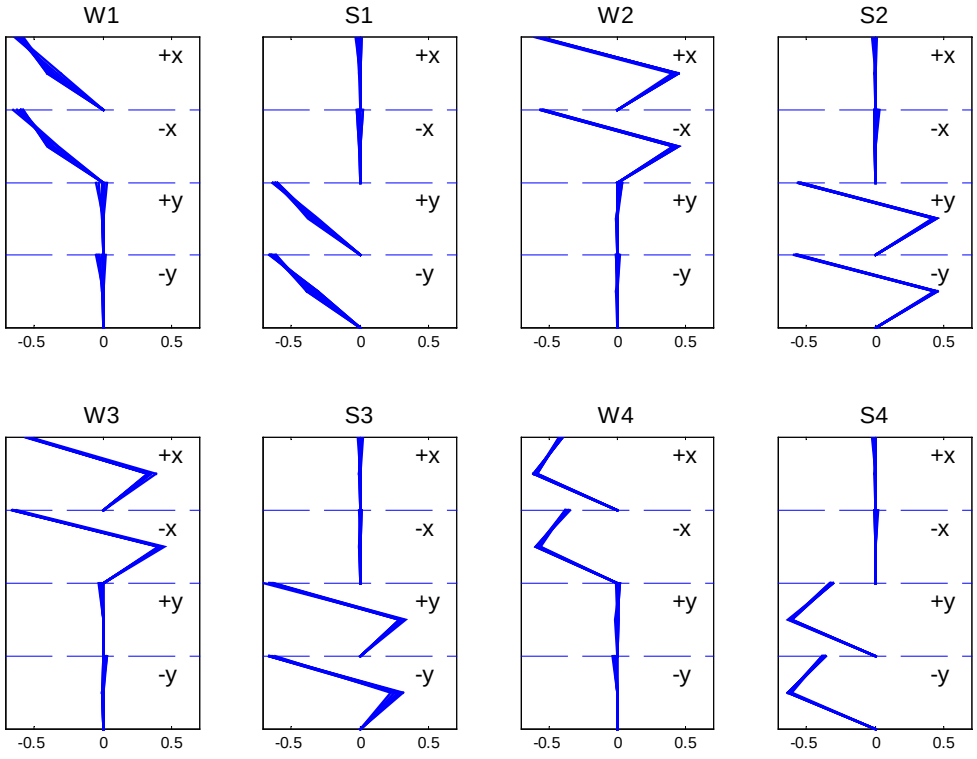

Figure 16. The experimental modeshape components of the structure for the DP2B.ps case.

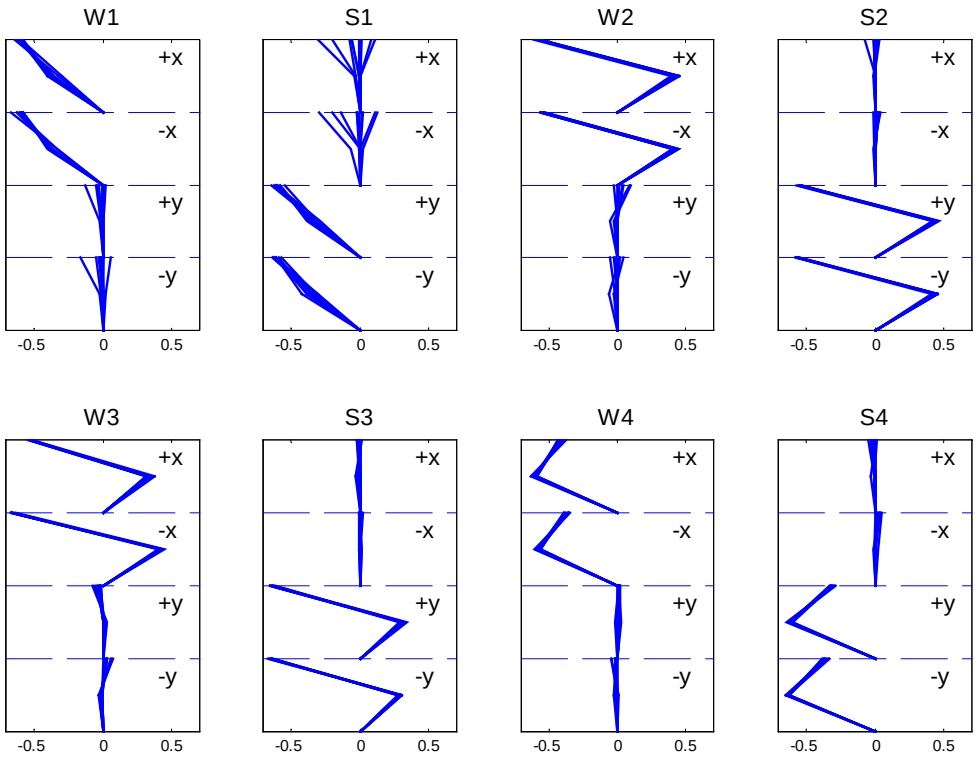

Figure 17. The experimental modeshape components of the structure for the DP3B.ps case.

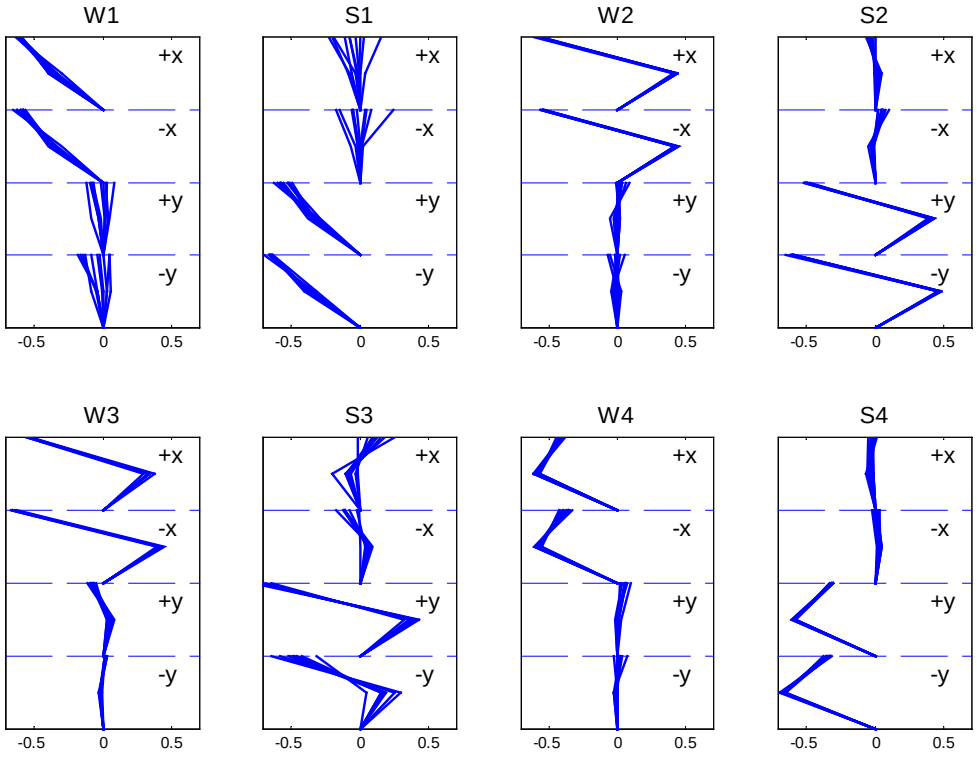

Figure 18. The experimental modeshape components of the structure for the DP3Bu.ps case.

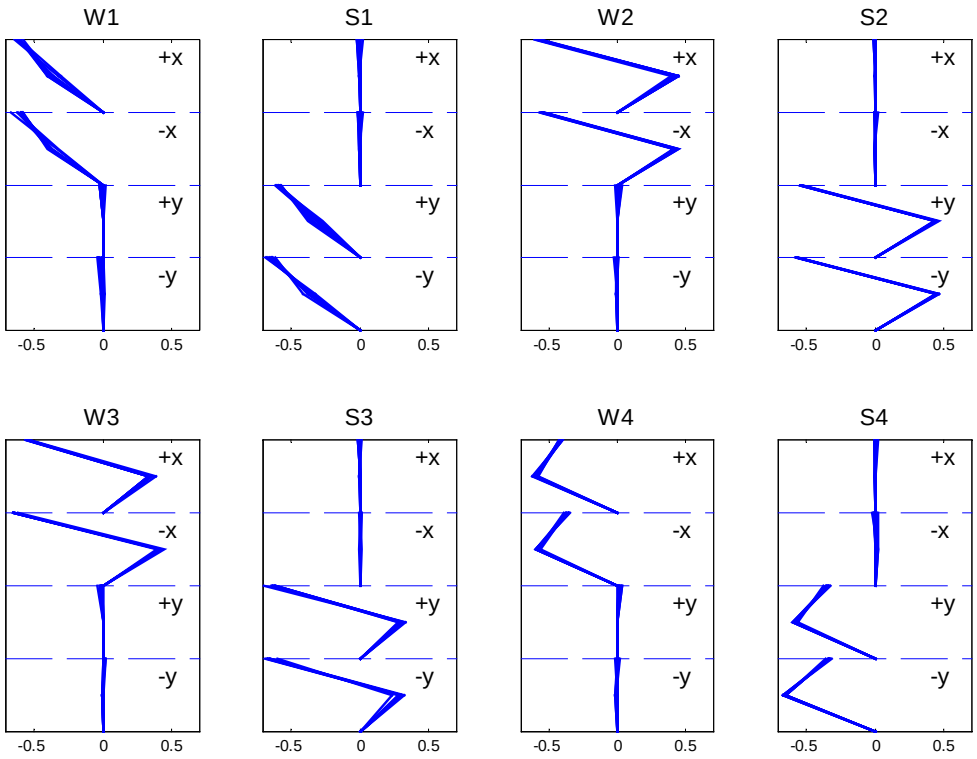

Figure 19. The experimental modeshape components of the structure for the Blind1.ps case.

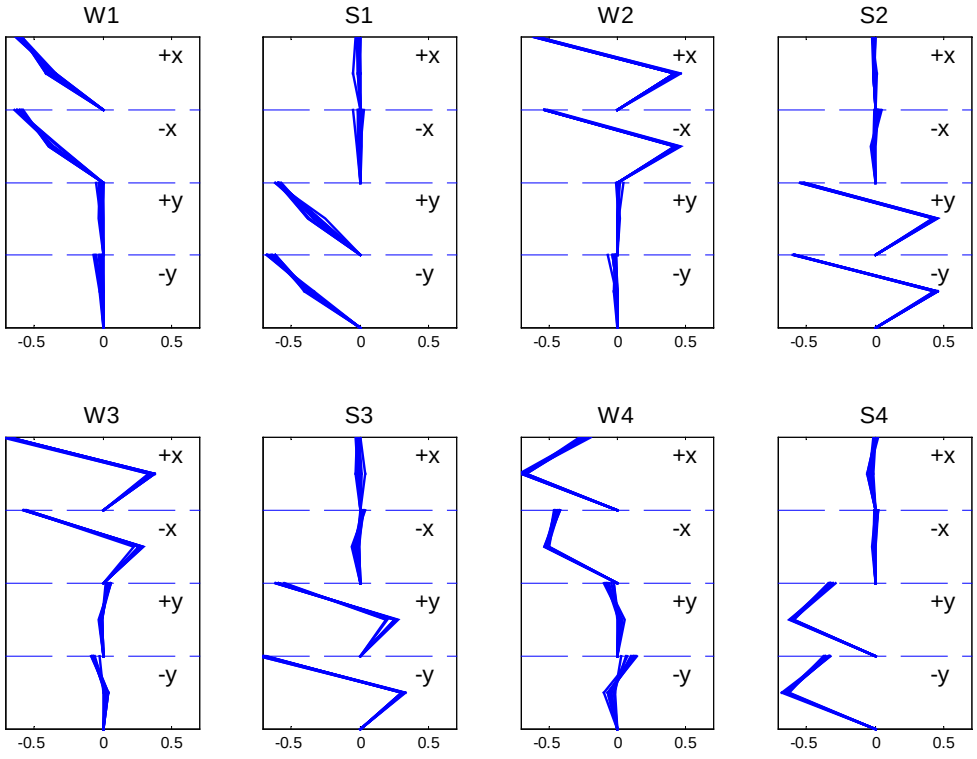

Figure 20. The experimental modeshape components of the structure for the Blind2.ps case.

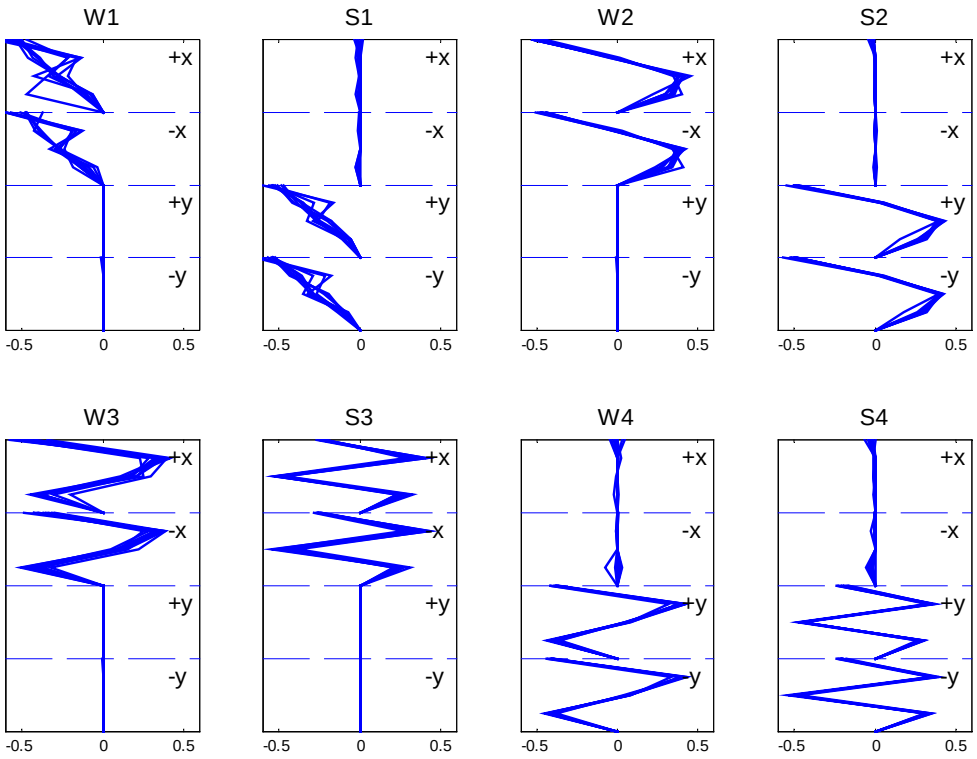

Figure 21. The experimental modeshape components of the structure for the RU.fs case.

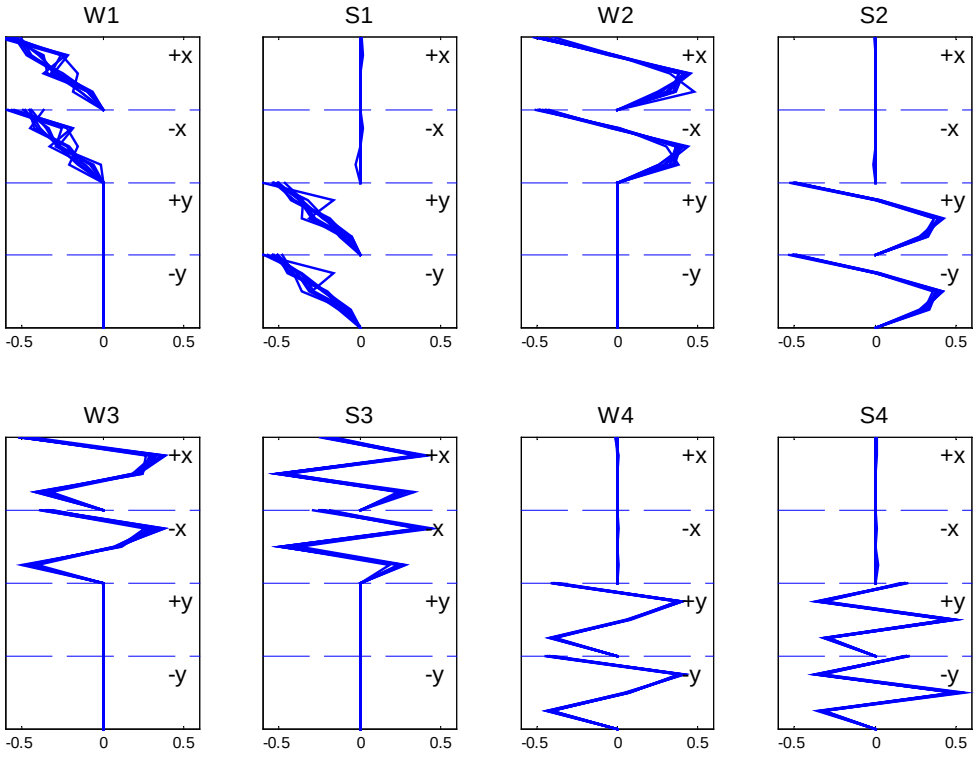

Figure 22. The experimental modeshape components of the structure for the DP1U.fs case.

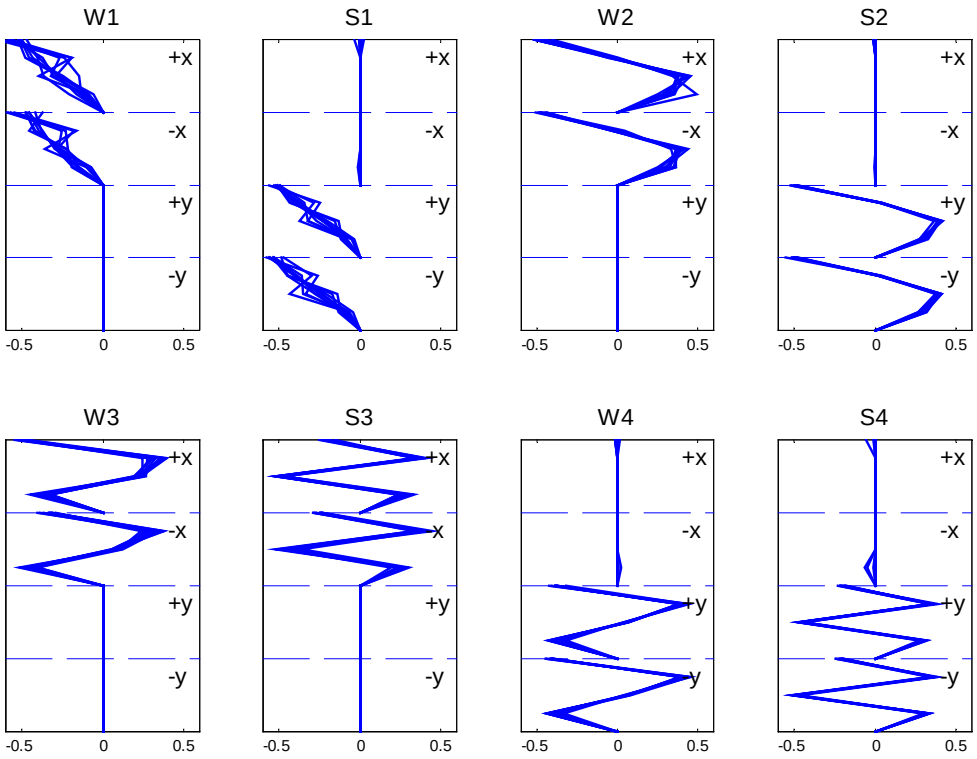

Figure 23. The experimental modeshape components of the structure for the DP2U.fs case.

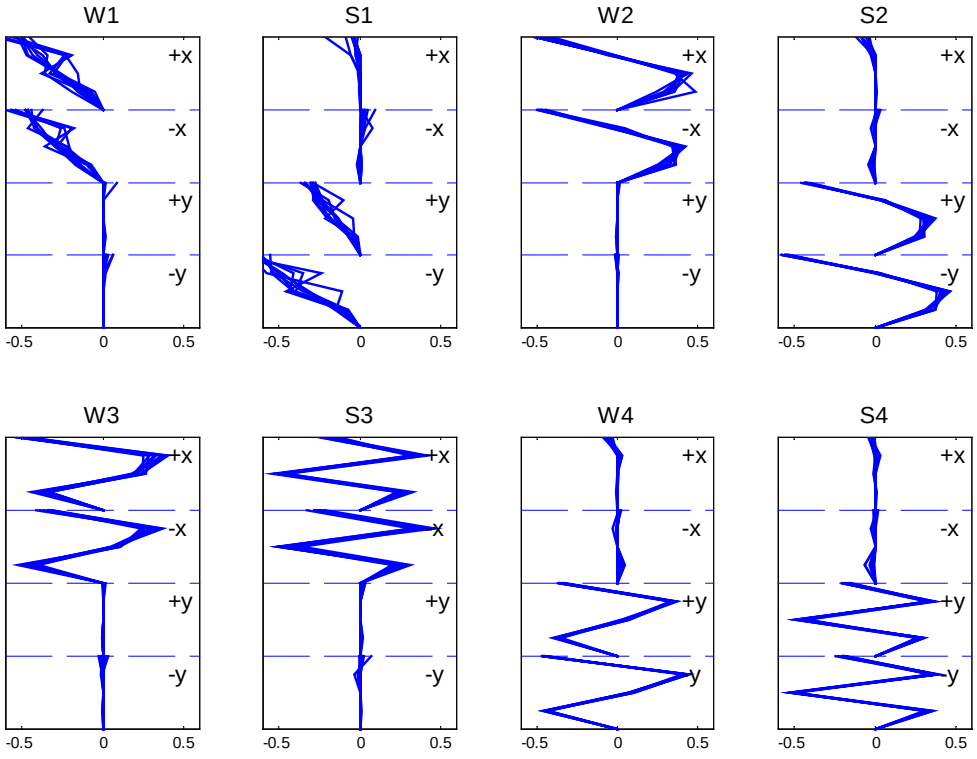

Figure 24. The experimental modeshape components of the structure for the DP1Uu.fs case.

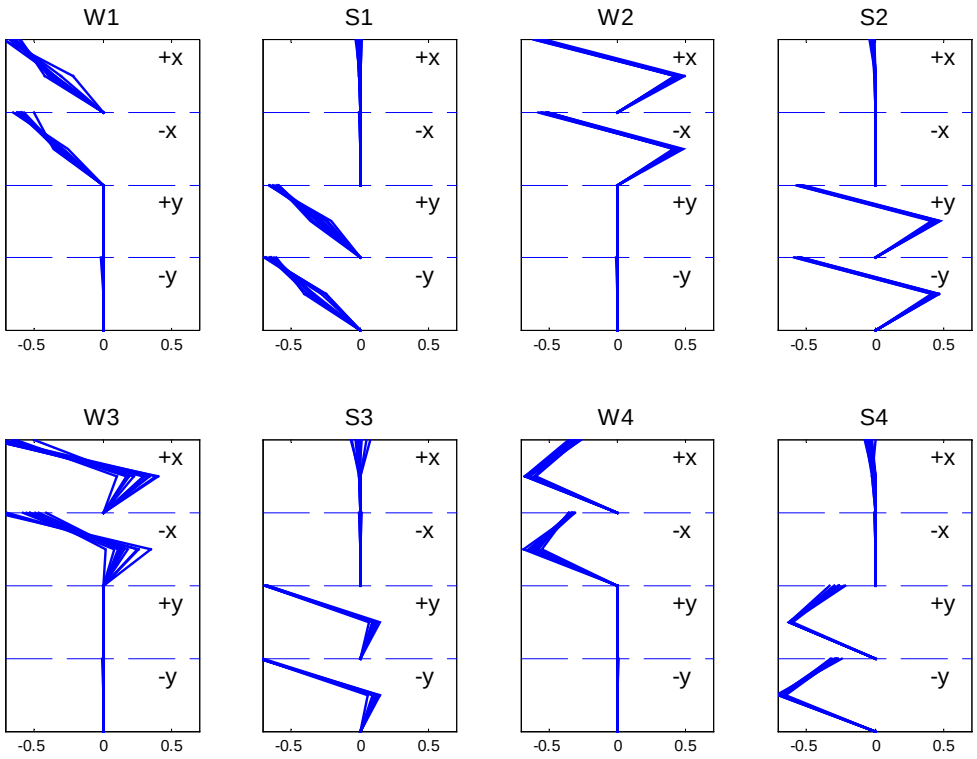

Figure 25. The experimental modeshape components on the four faces of the structure for the RU.ps case.

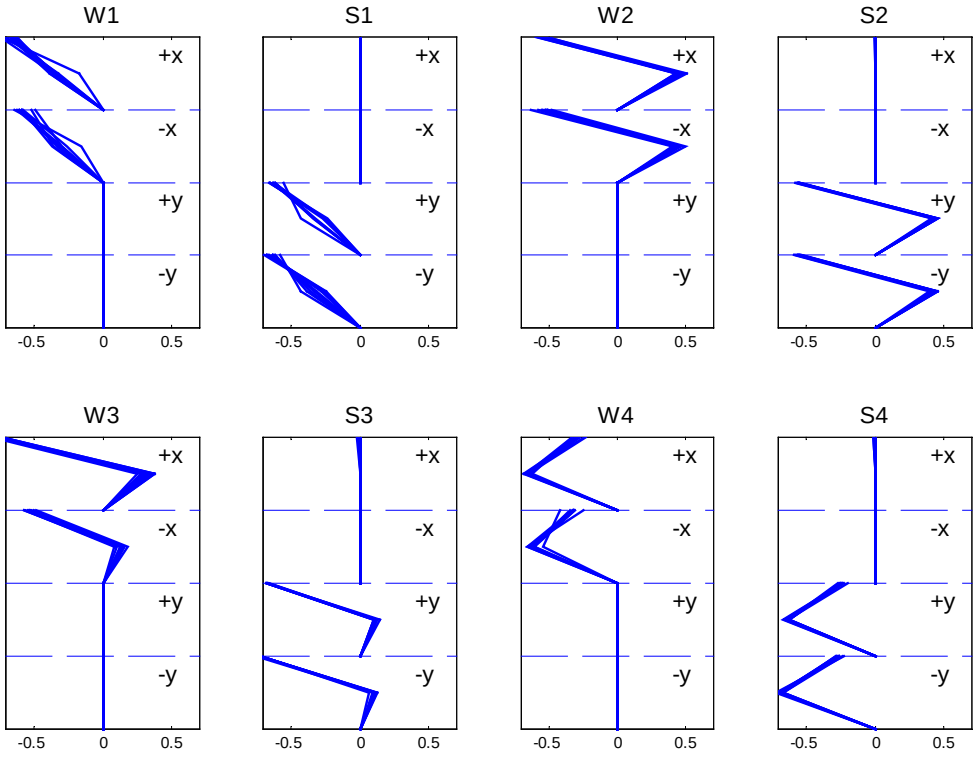

Figure 26. The experimental modeshape components of the structure for the DP1U.ps case.

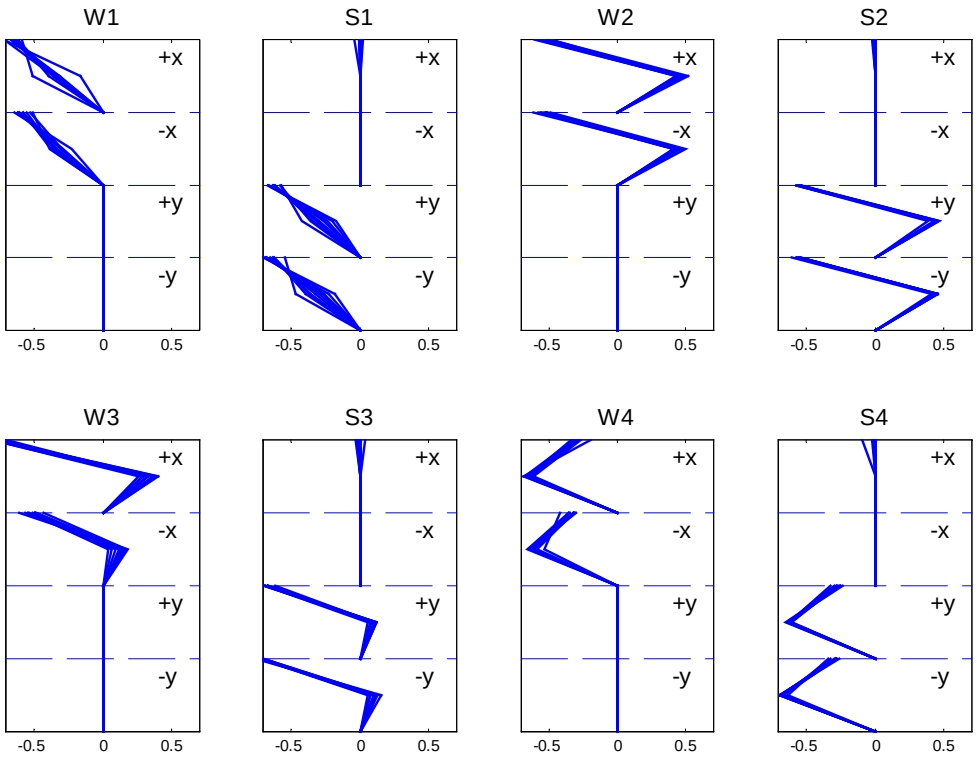

Figure 27. The experimental modeshape components of the structure for the DP2U.ps case.

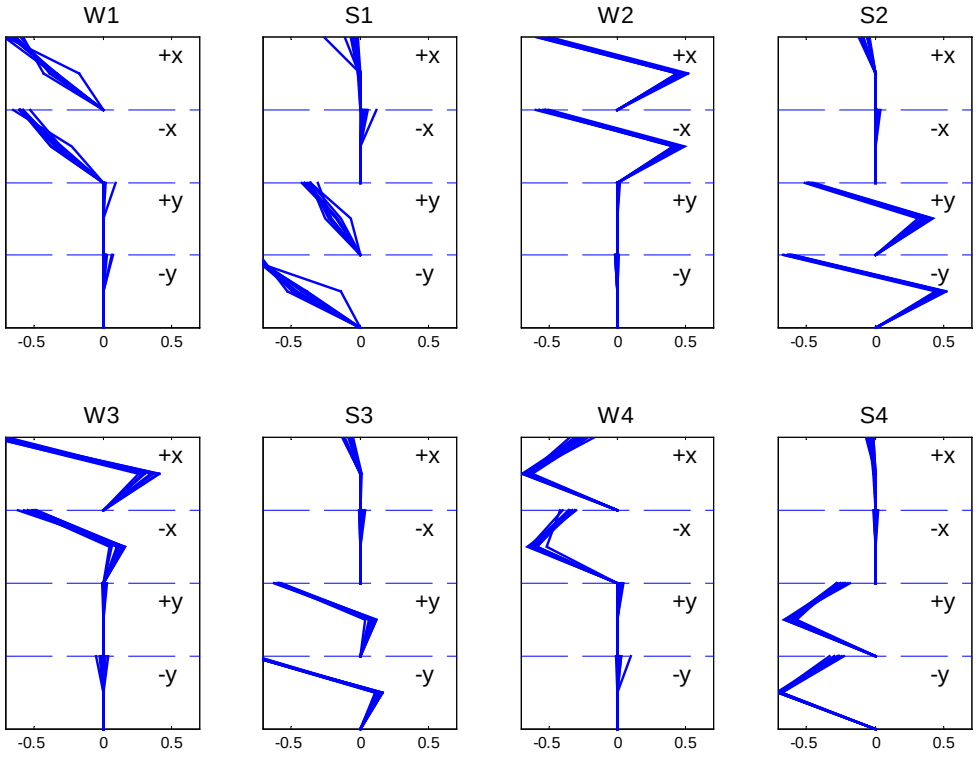

Figure 28. The experimental modeshape components of the structure for the DP1Uu.ps case.

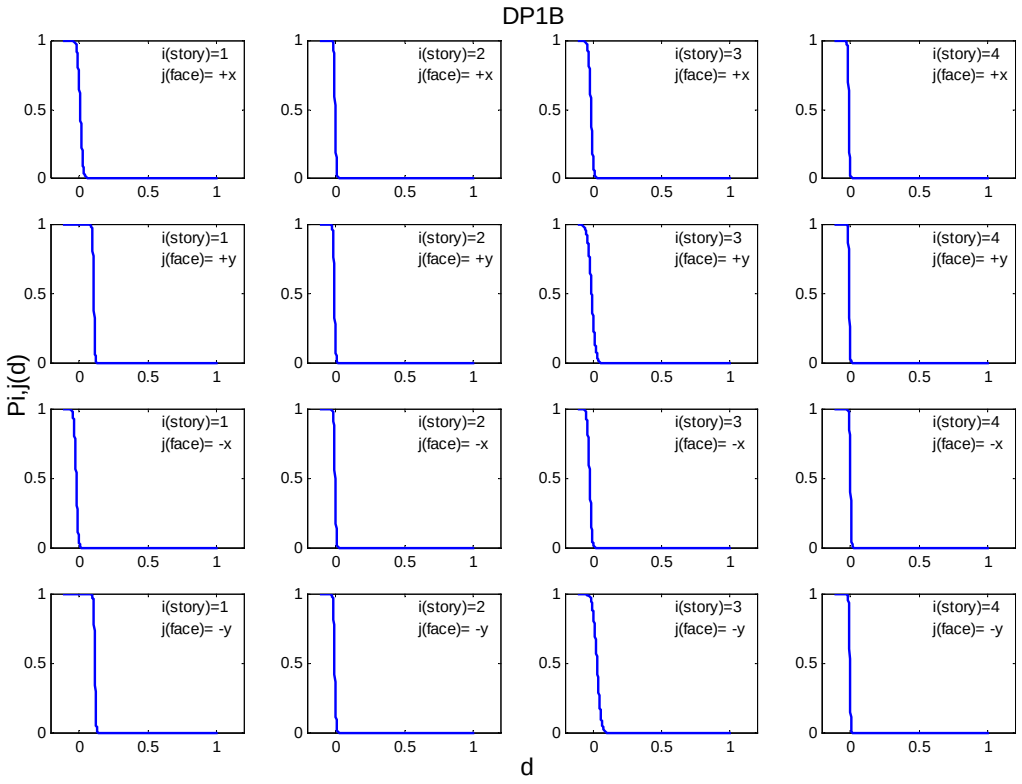

Figure 29. The probability $P_{ij}(d)$ of damage exceeding d in each substructure (DP1B.fs case).

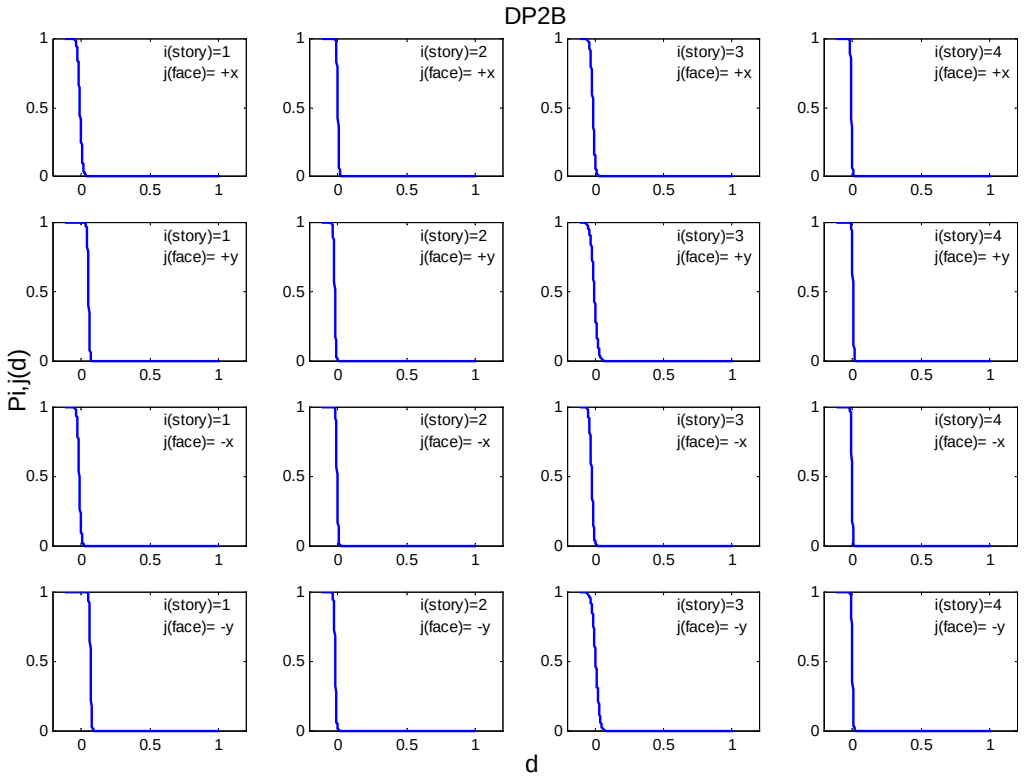

Figure 30. The probability $P_{ij}(d)$ of damage exceeding d in each substructure (DP2B.fs case).

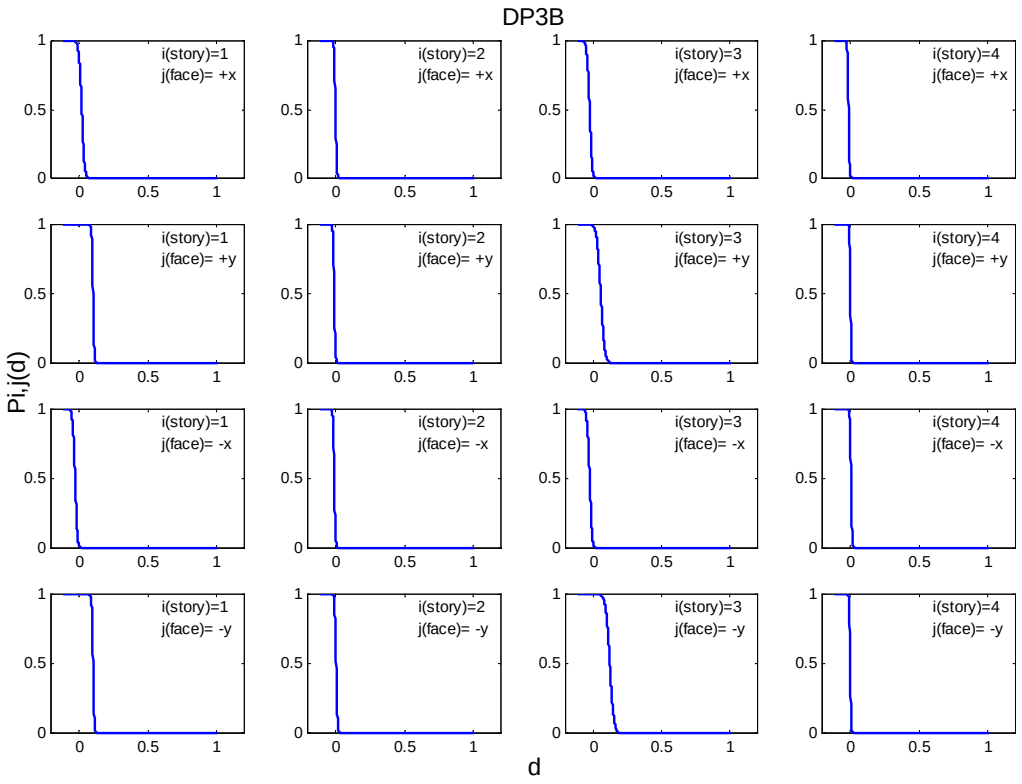

Figure 31. The probability $P_{ij}(d)$ of damage exceeding d in each substructure (DP3B.fs case).

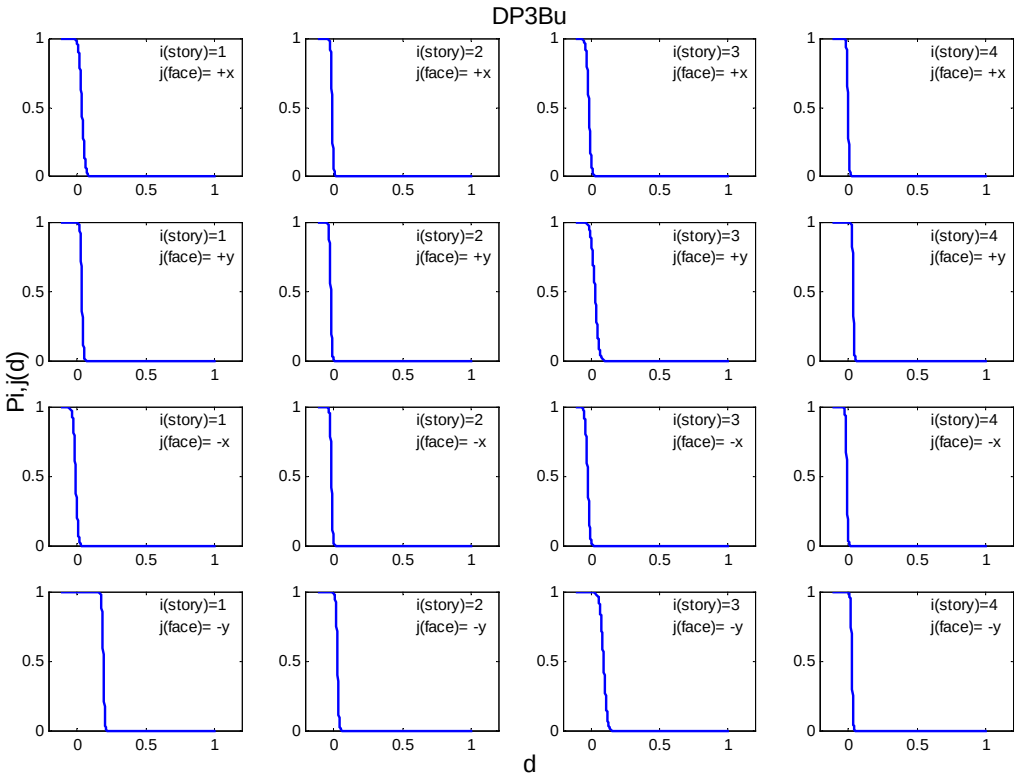

Figure 32. The probability $P_{ij}(d)$ of damage exceeding d in each substructure (DP3Bu.fs case).

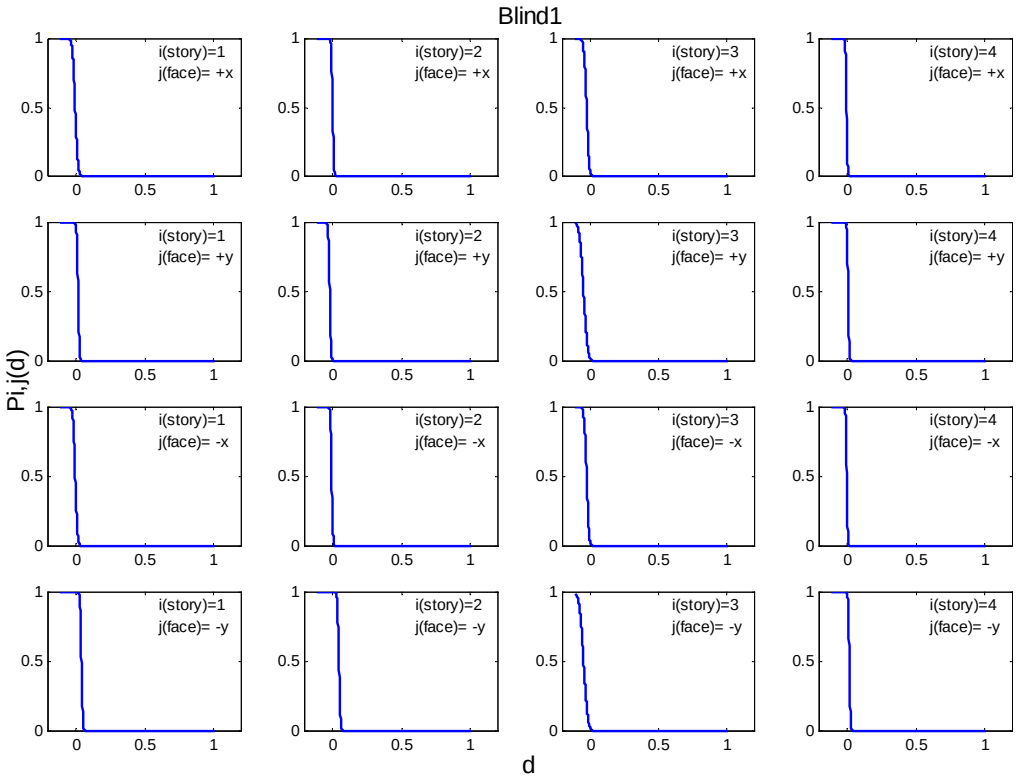

Figure 33. The probability $P_{ij}(d)$ of damage exceeding d in each substructure (Blind1.fs case).

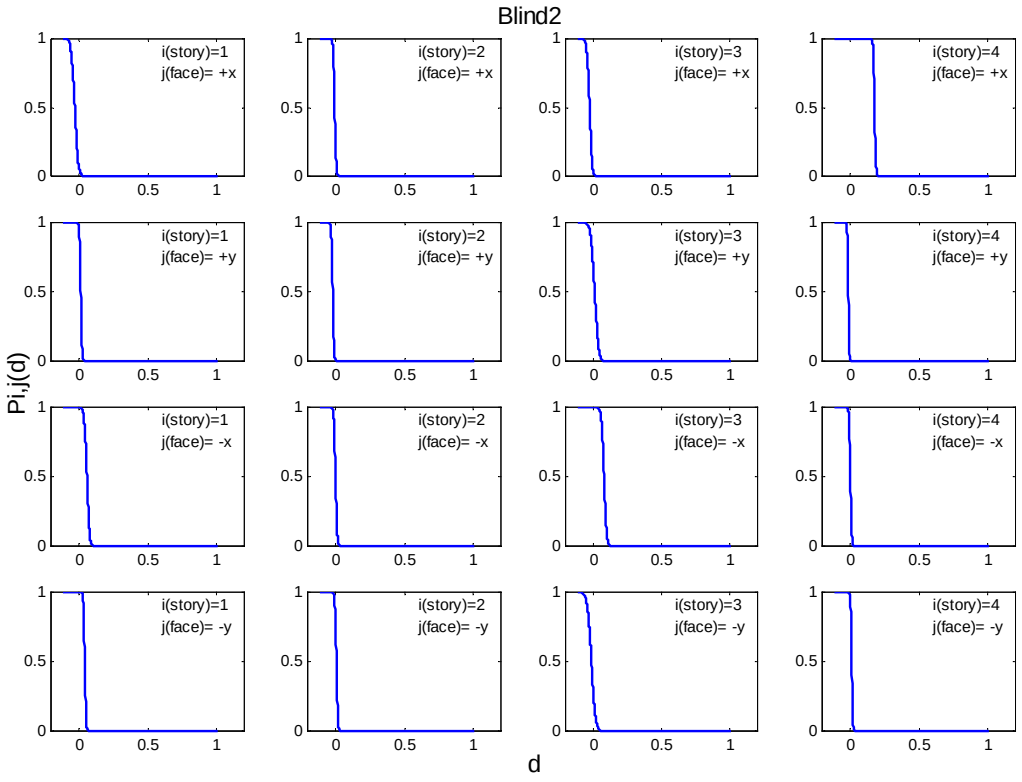

Figure 34. The probability $P_{ij}(d)$ of damage exceeding d in each substructure (Blind2.fs case).

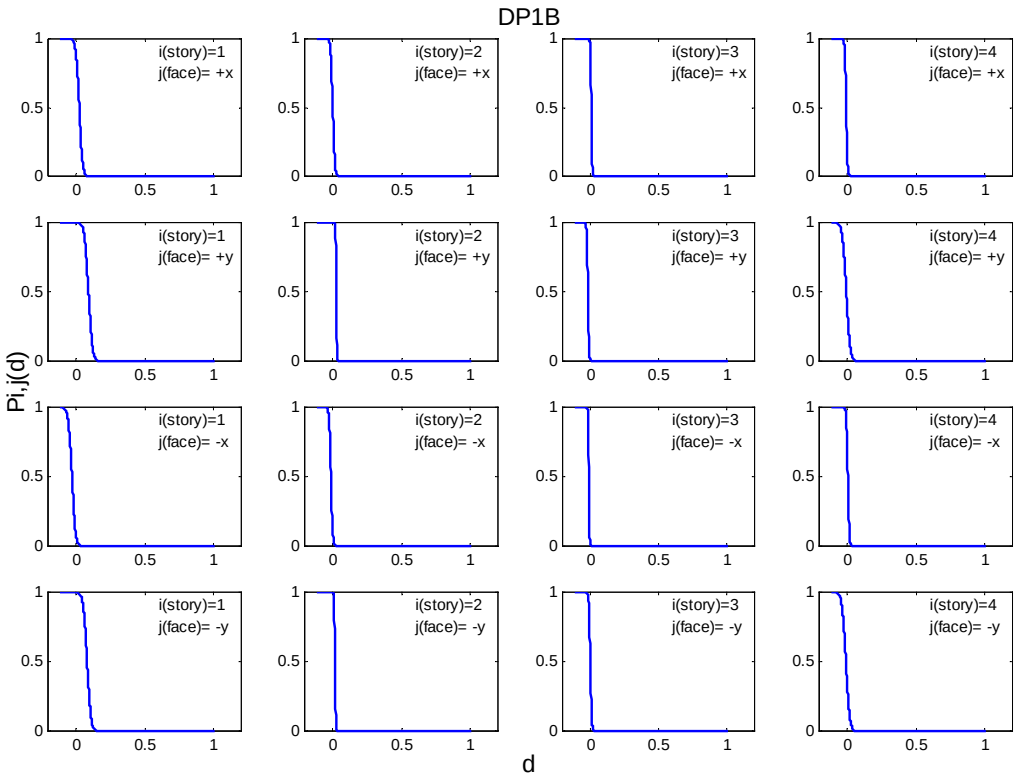

Figure 35. The probability $P_{ij}(d)$ of damage exceeding d in each substructure (DP1B.ps case).

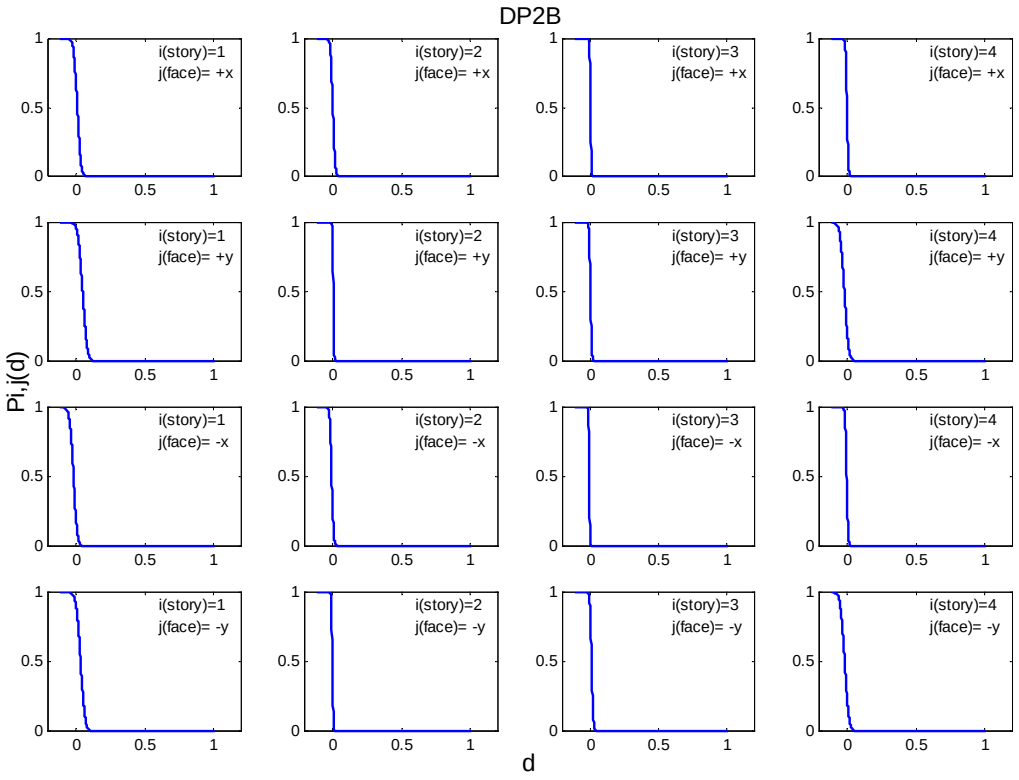

Figure 36. The probability $P_{ij}(d)$ of damage exceeding d in each substructure (DP2B.ps case).

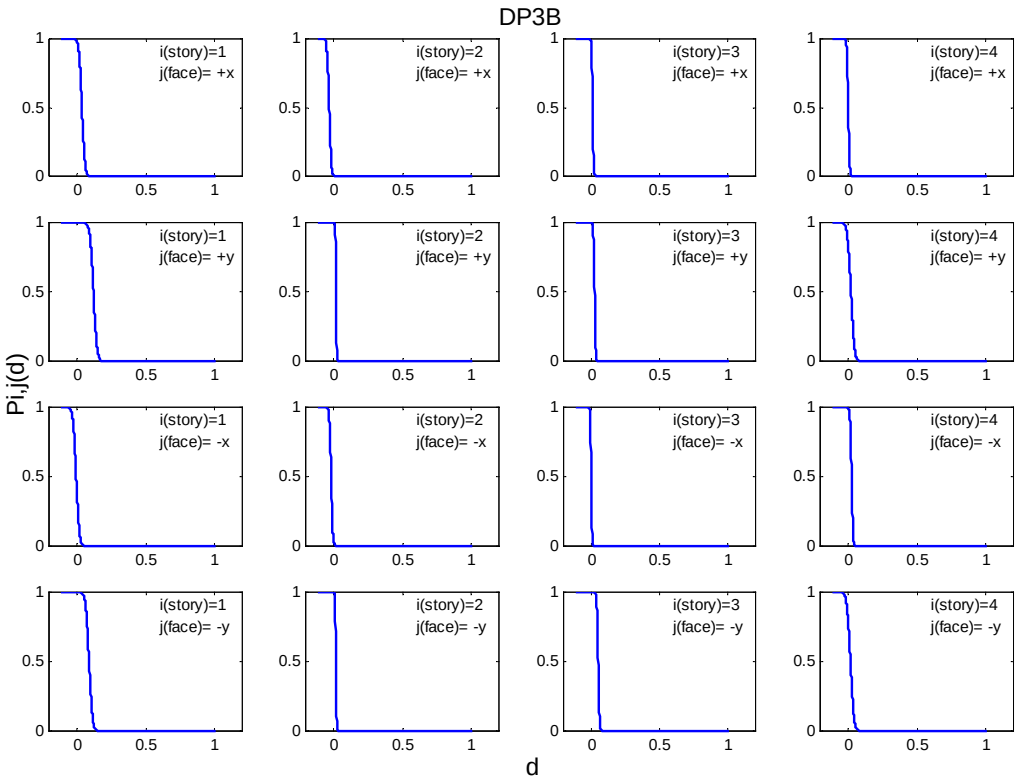

Figure 37. The probability $P_{ij}(d)$ of damage exceeding d in each substructure (DP3B.ps case).

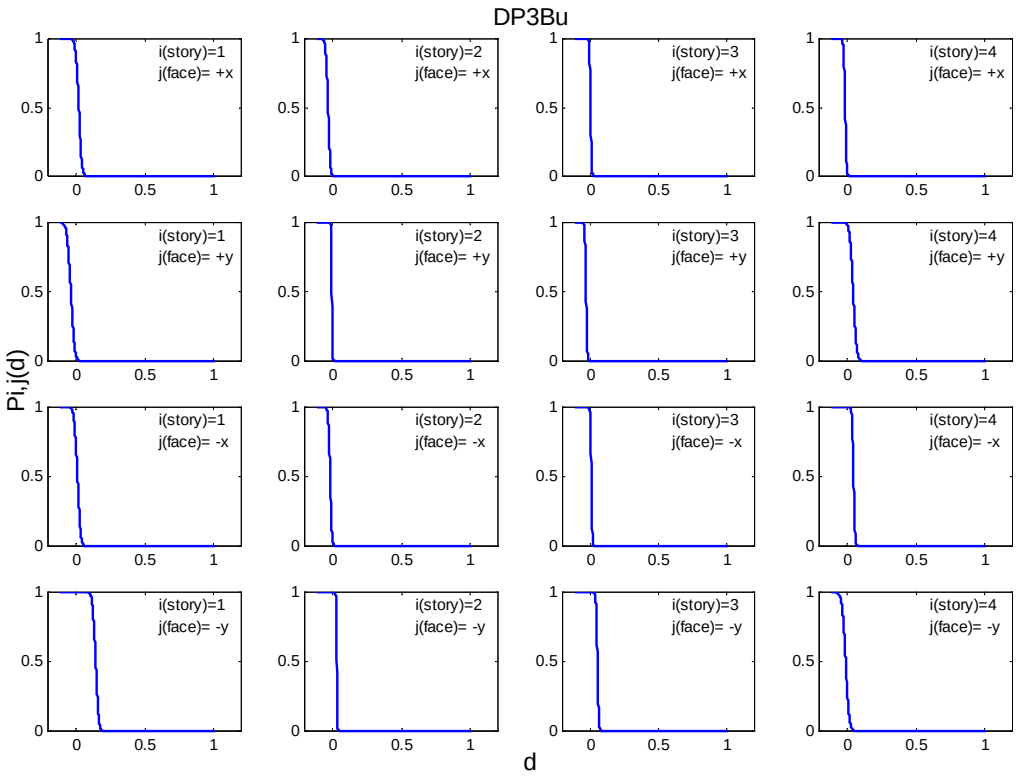

Figure 38. The probability $P_{ij}(d)$ of damage exceeding d in each substructure (DP3Bu.ps case).

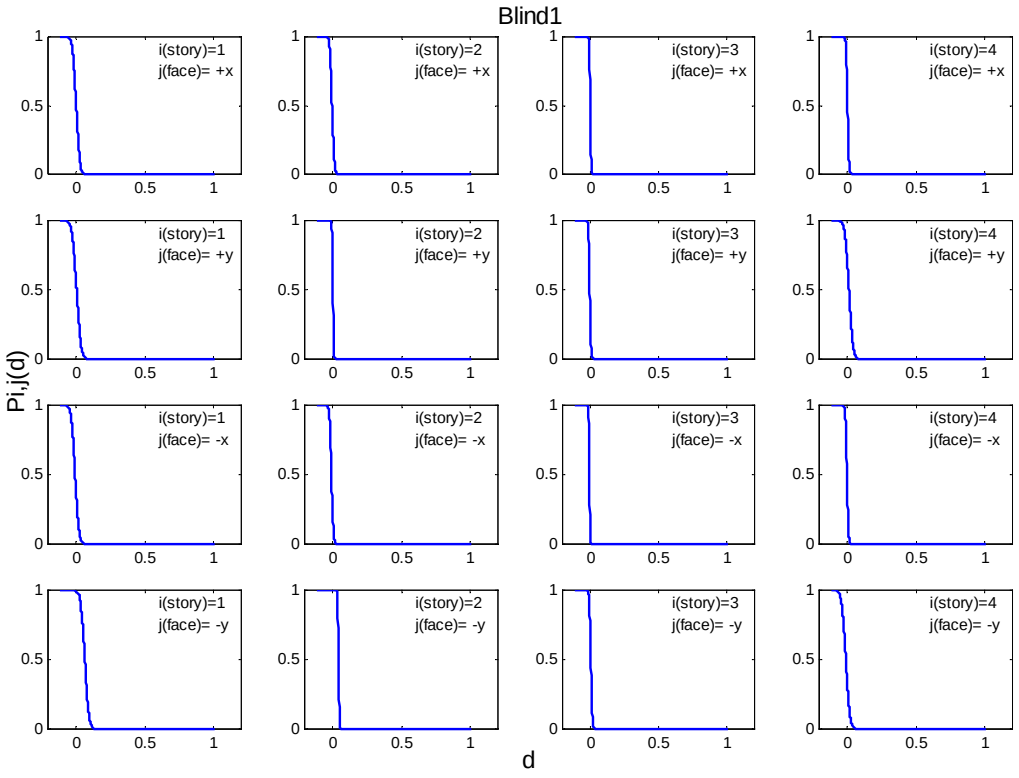

Figure 39. The probability $P_{ij}(d)$ of damage exceeding d in each substructure (Blind1.ps case).

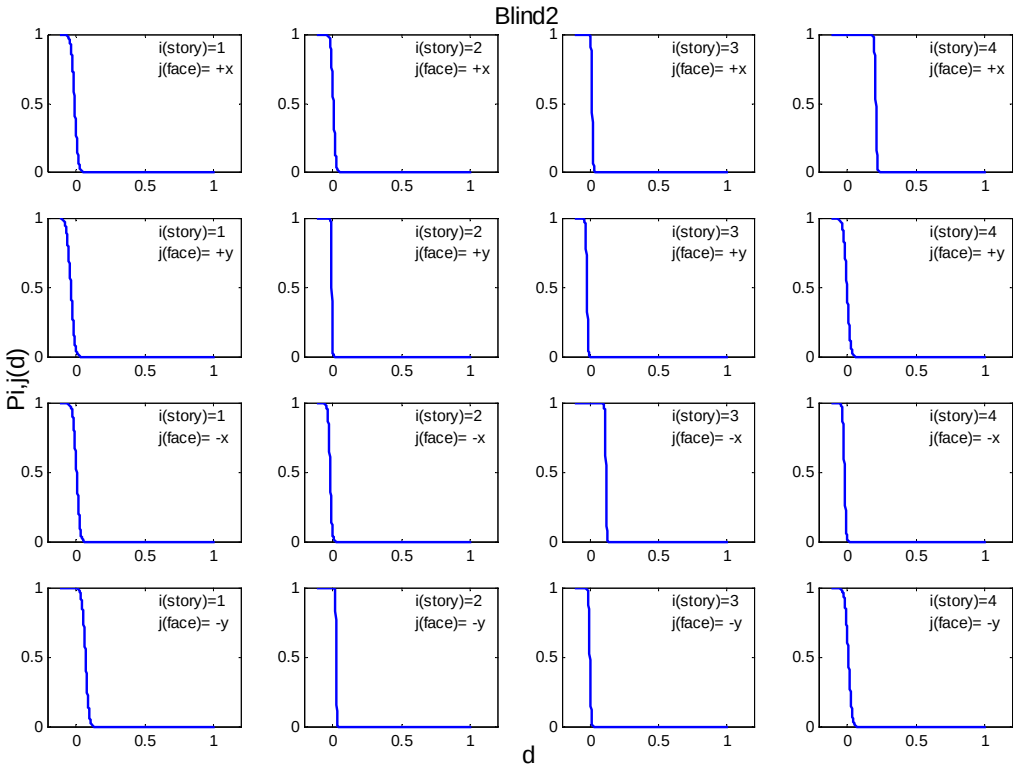

Figure 40. The probability $P_{ij}(d)$ of damage exceeding d in each substructure (Blind2.ps case).

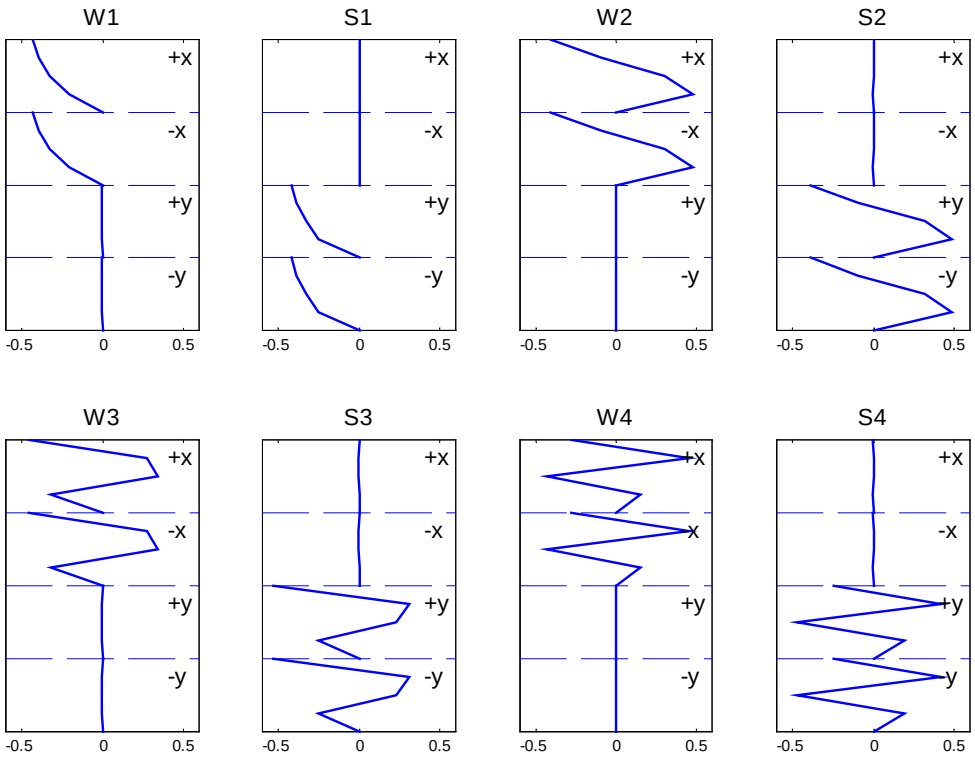

Figure 41. The identified system modeshape for the RB.ps case.

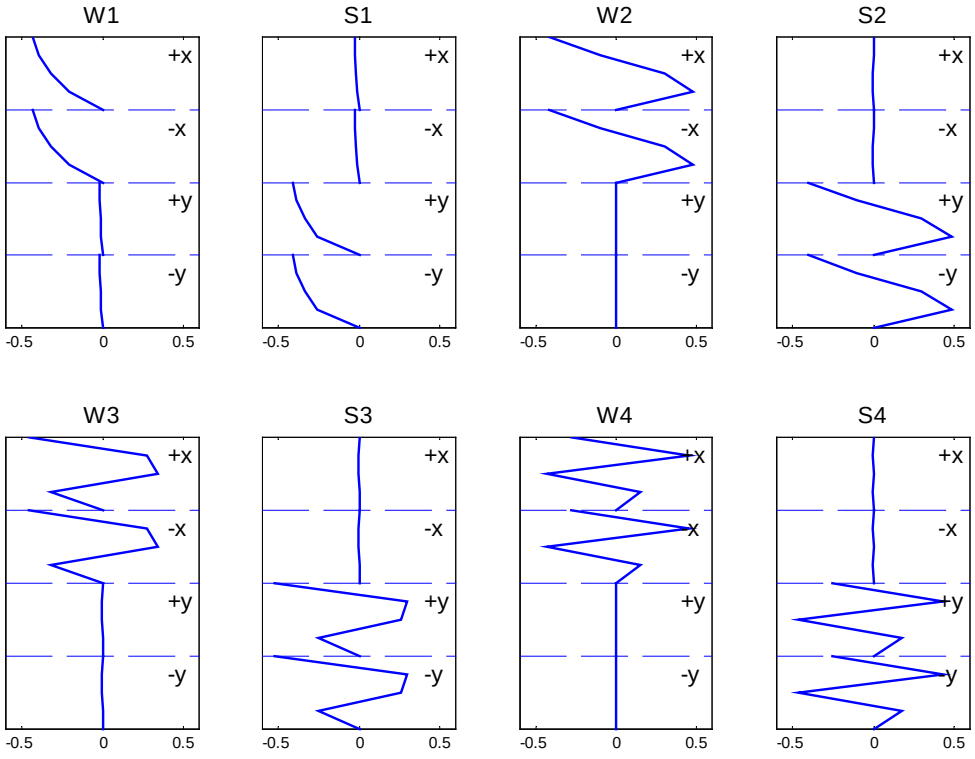

Figure 42. The identified system modeshape for the DP1B.ps case.

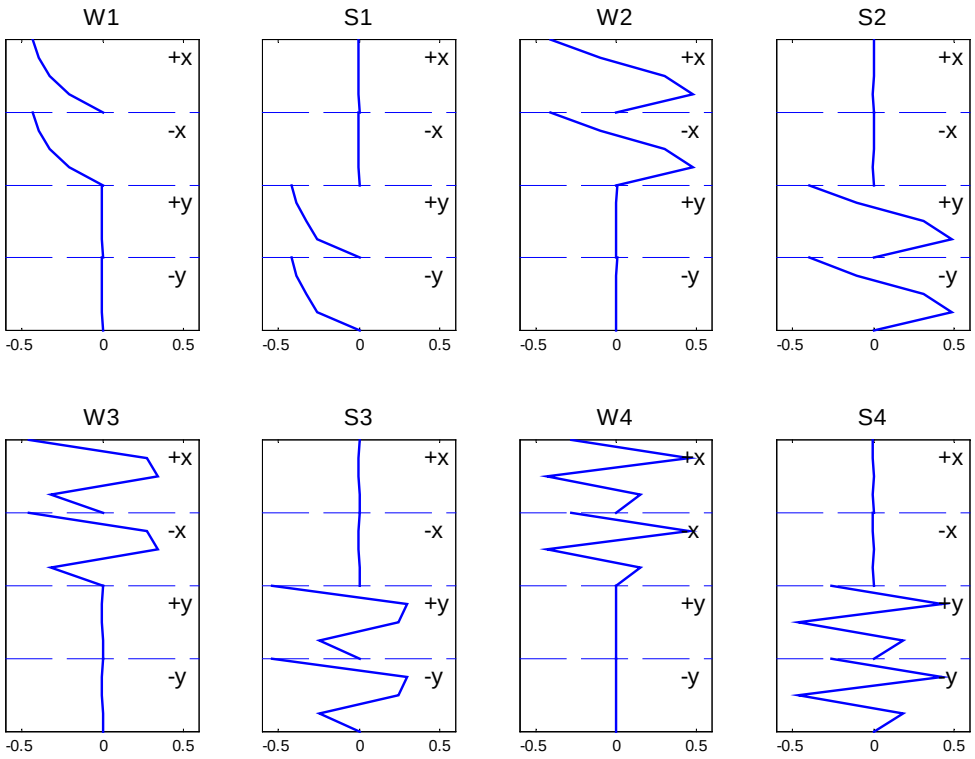

Figure 43. The identified system modeshape for the DP2B.ps case.

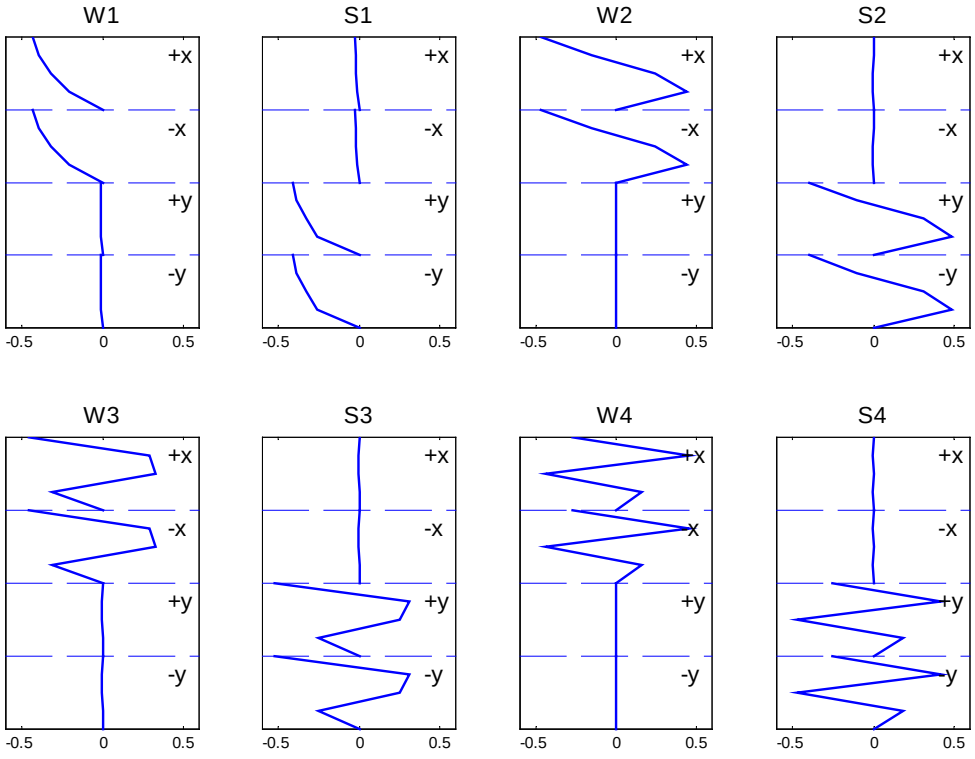

Figure 44. The identified system modeshape for the DP3B.ps case.

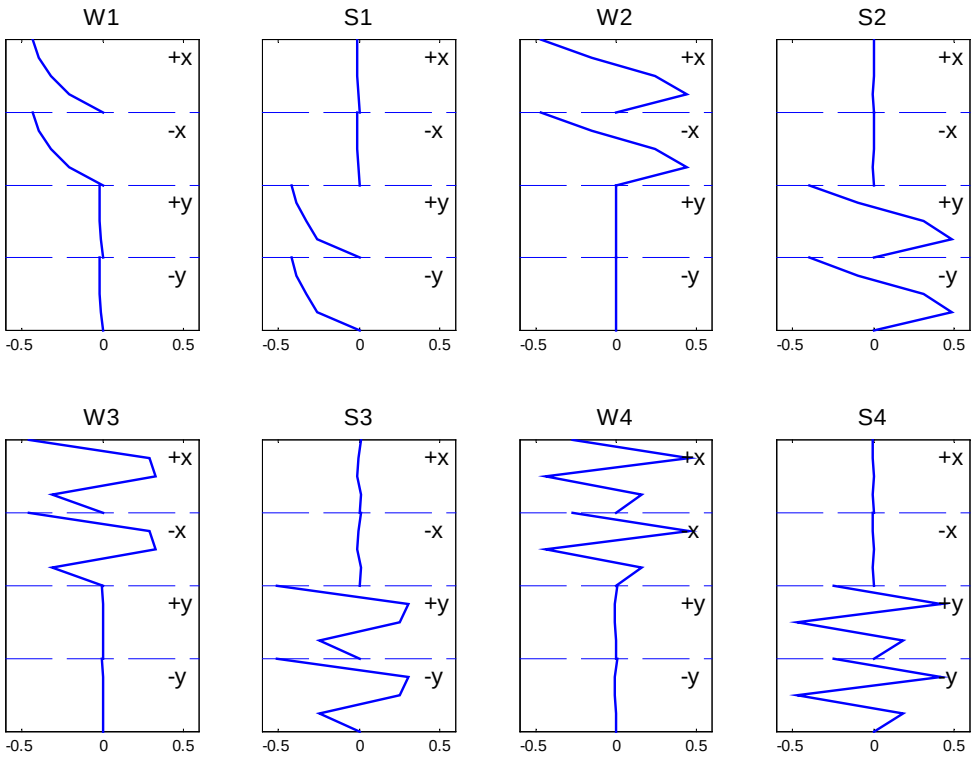

Figure 45. The identified system modeshape for the DP3Bu.ps case.

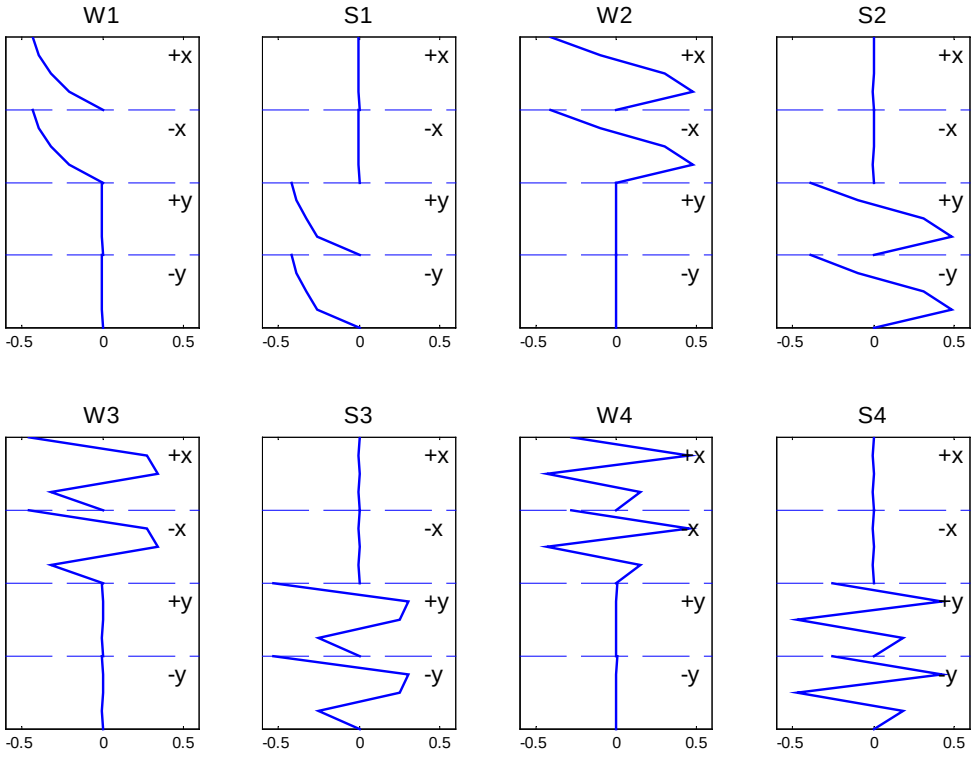

Figure 46. The identified system modeshape for the Blind1.ps case.

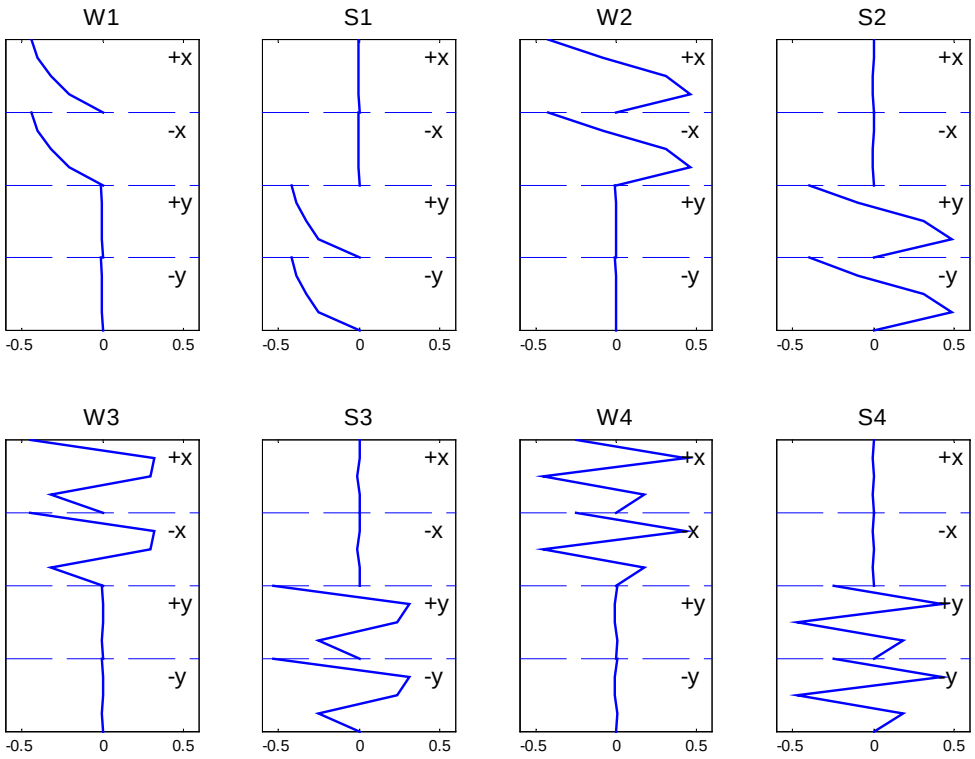

Figure 47. The identified system modeshape for the Blind2.ps case.

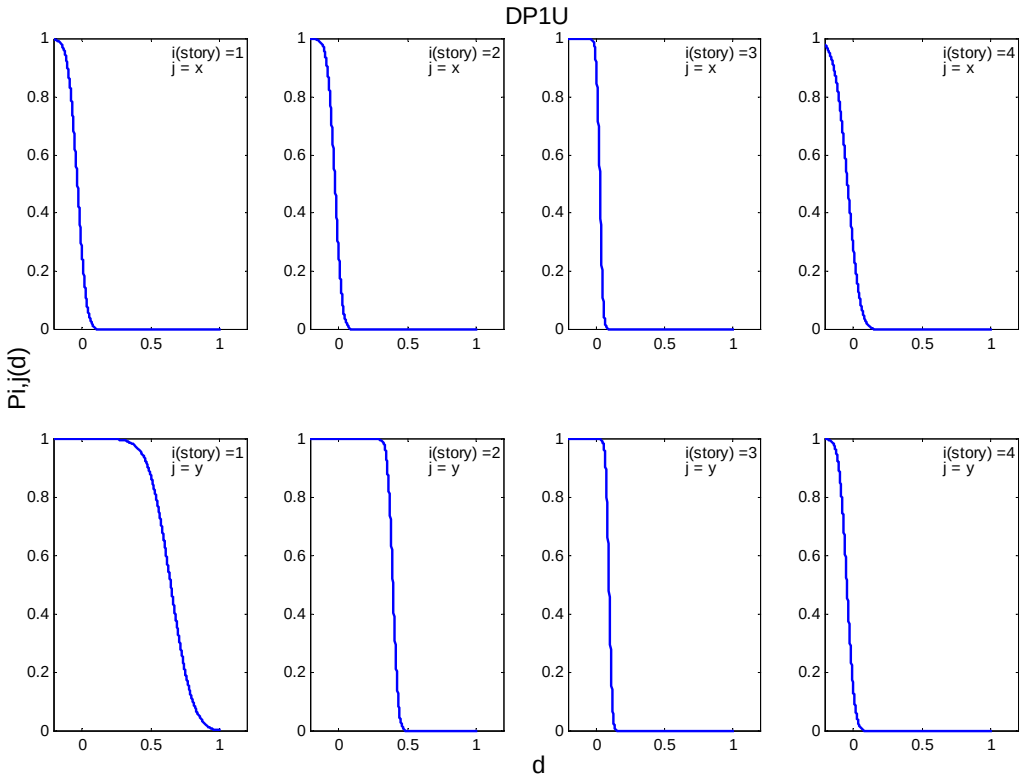

Figure 48. The probability $P_{ij}(d)$ of damage exceeding d in each substructure (DP1U.fs case).

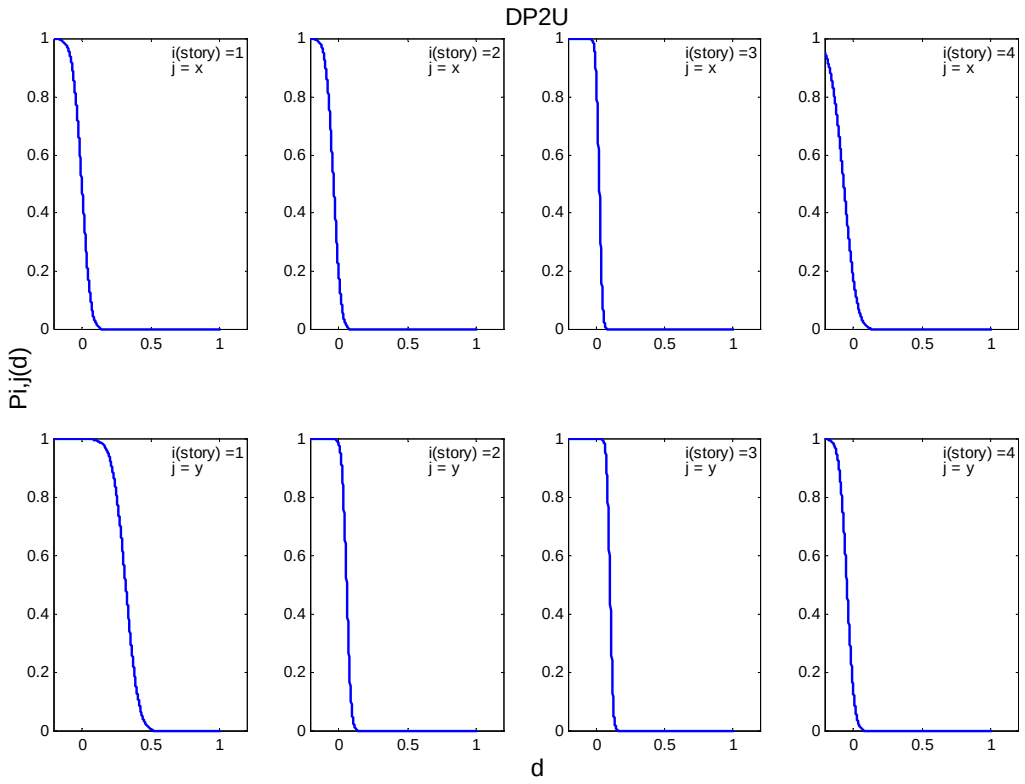

Figure 49. The probability $P_{ij}(d)$ of damage exceeding d in each substructure (DP2U.fs case).

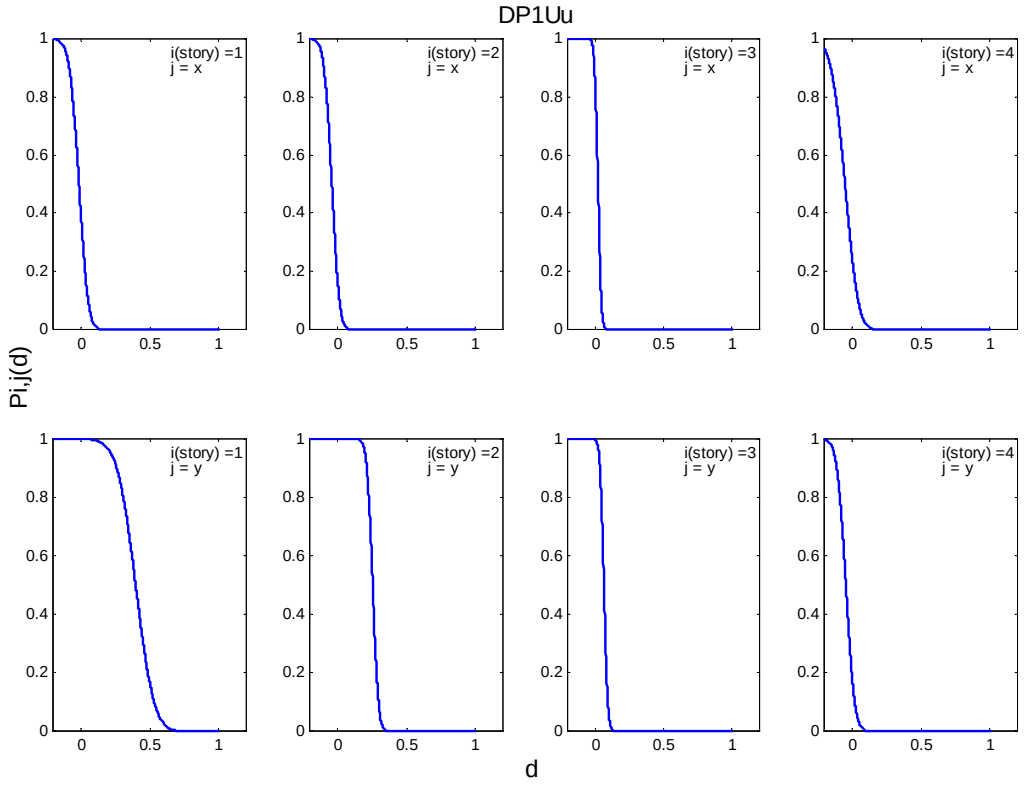

Figure 50. The probability $P_{ij}(d)$ of damage exceeding d in each substructure (DP1Uu.fs case).

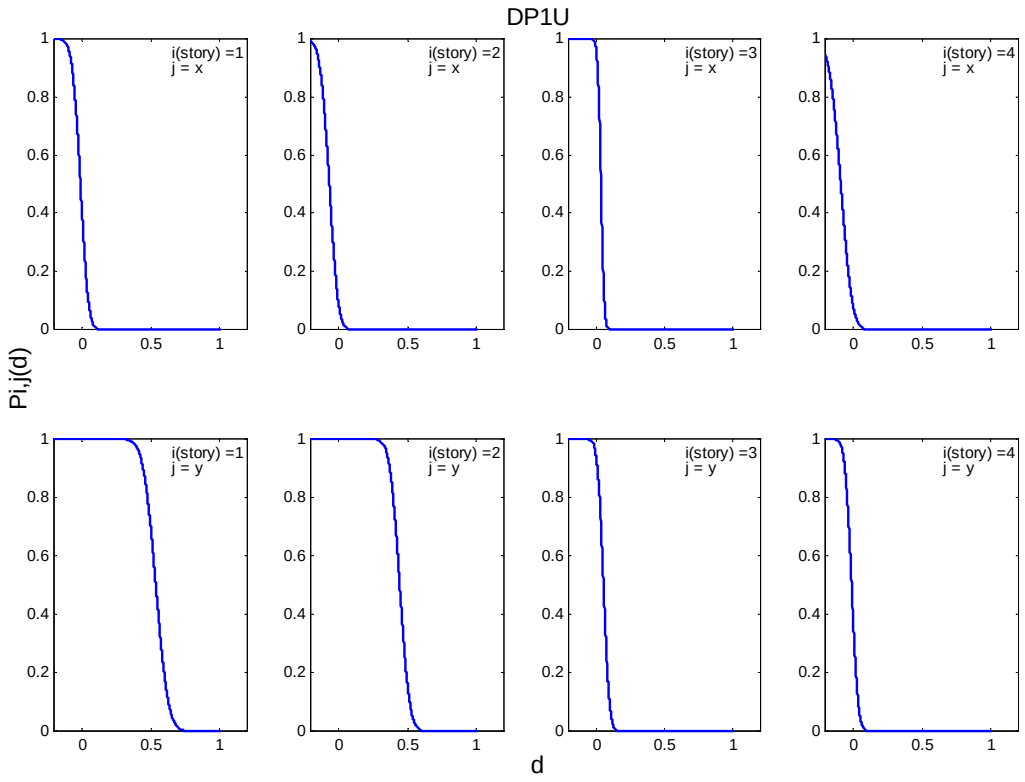

Figure 51. The probability $P_{ij}(d)$ of damage exceeding d in each substructure (DP1U.ps case).

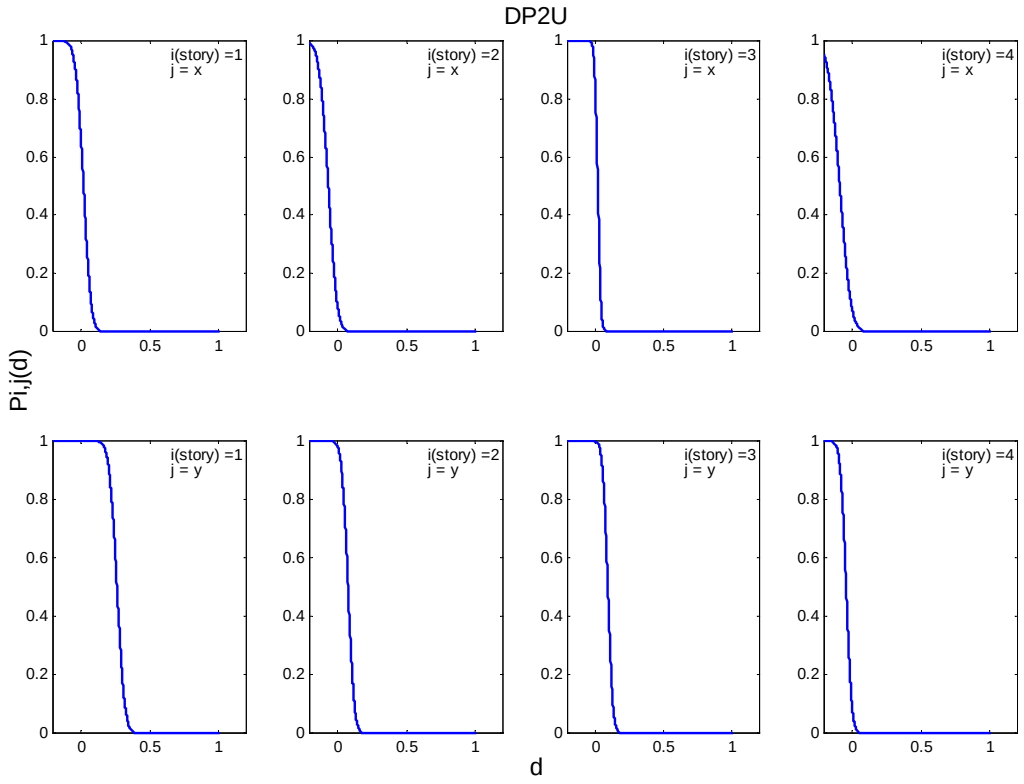

Figure 52. The probability $P_{ij}(d)$ of damage exceeding d in each substructure (DP2U.ps case).

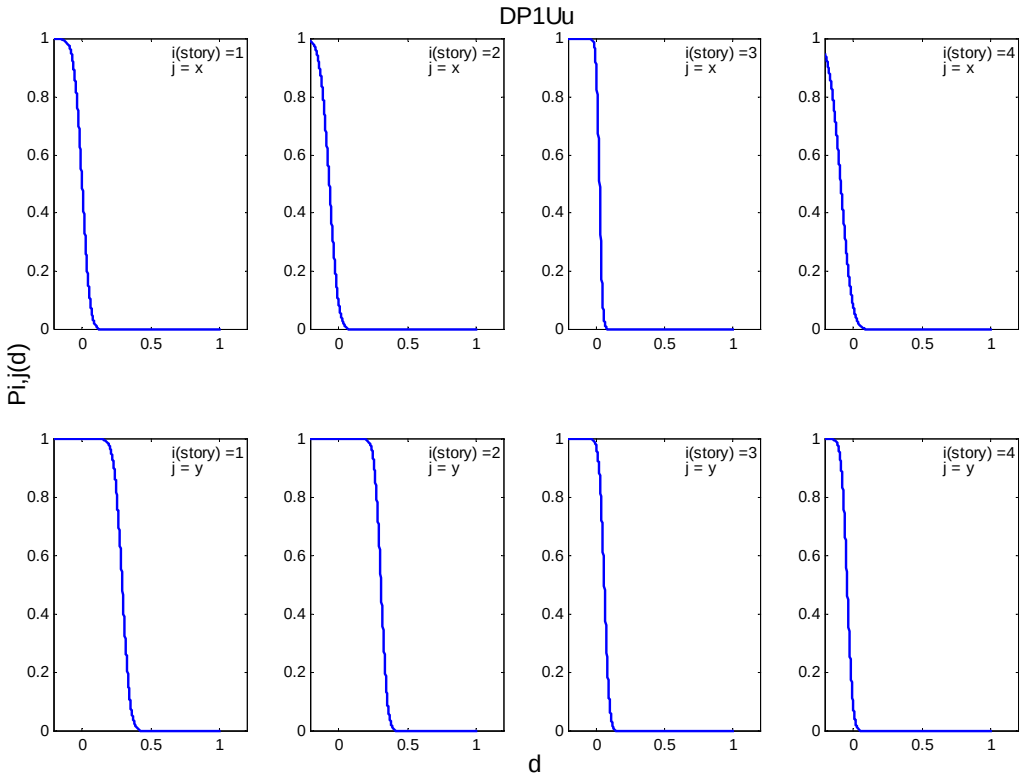

Figure 53. The probability $P_{ij}(d)$ of damage exceeding d in each substructure (DP1Uu.ps case).

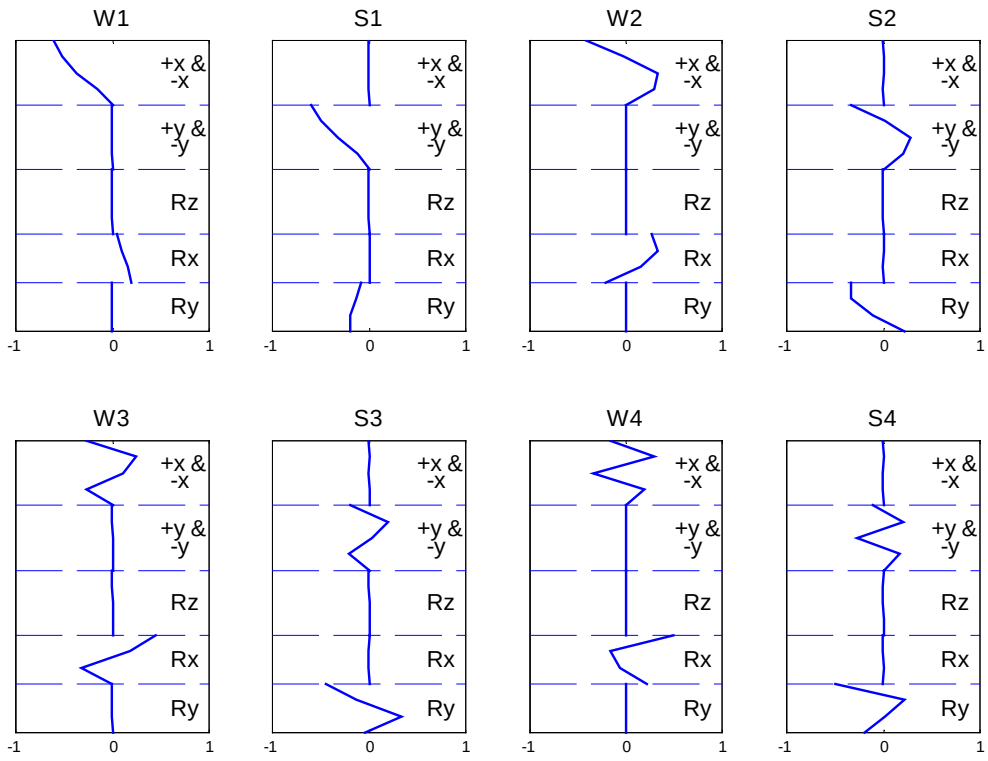

Figure 54. The identified system modeshape for the RU.fs case.

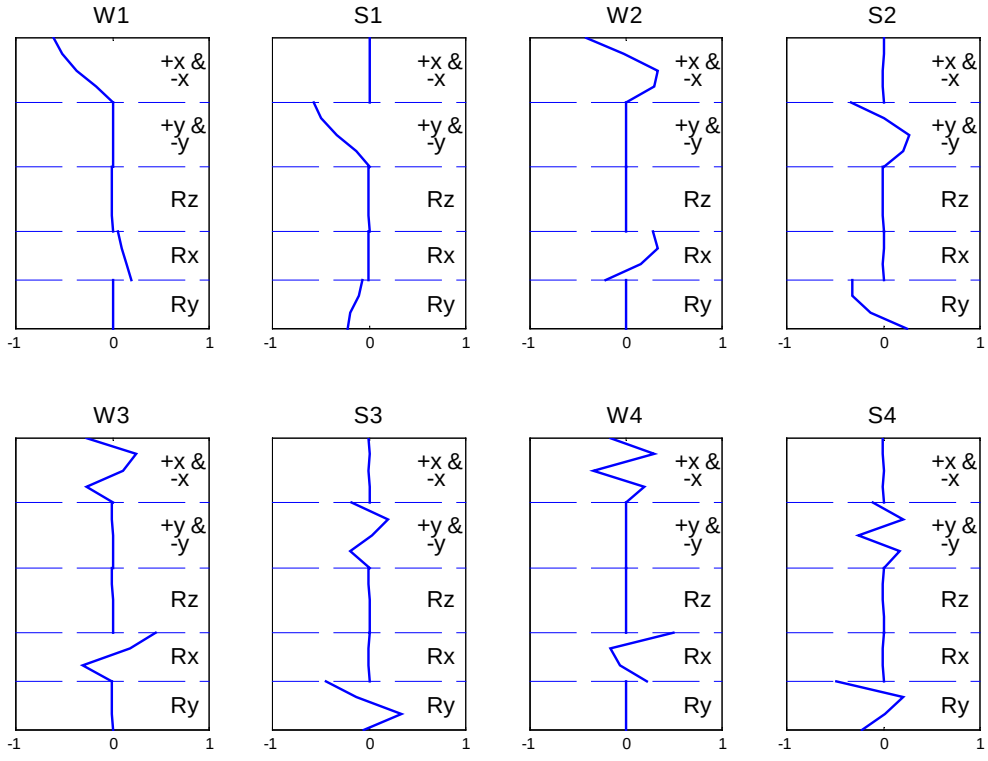

Figure 55. The identified system modeshape for the DP1U.fs case.

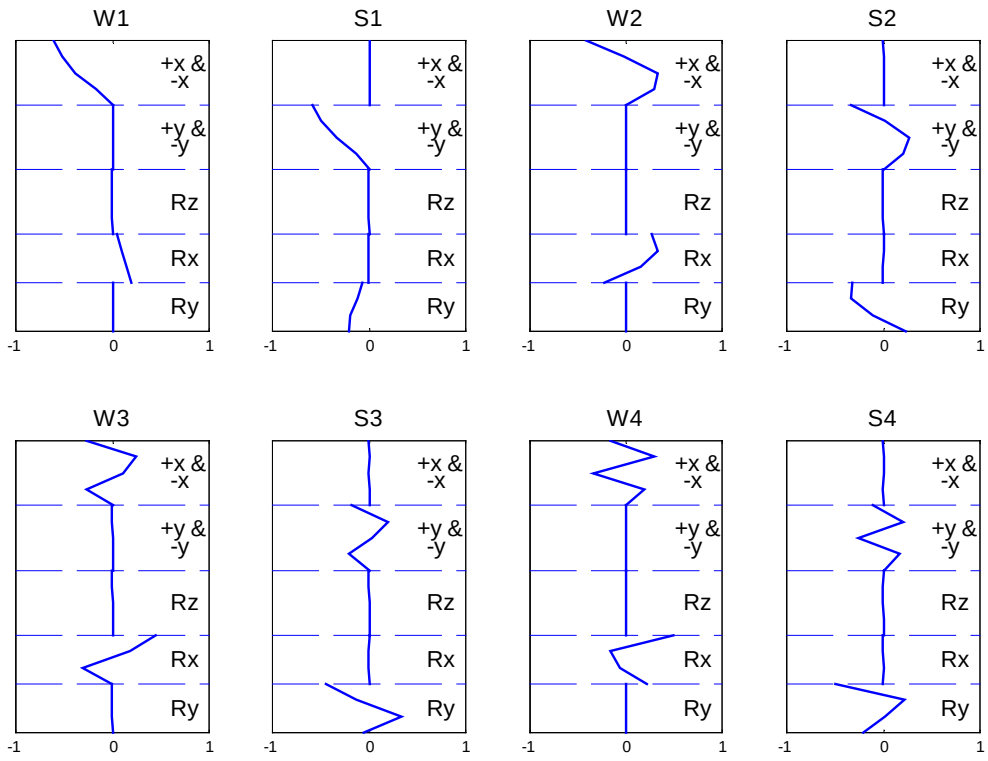

Figure 56. The identified system modeshape for the DP2U.fs case.

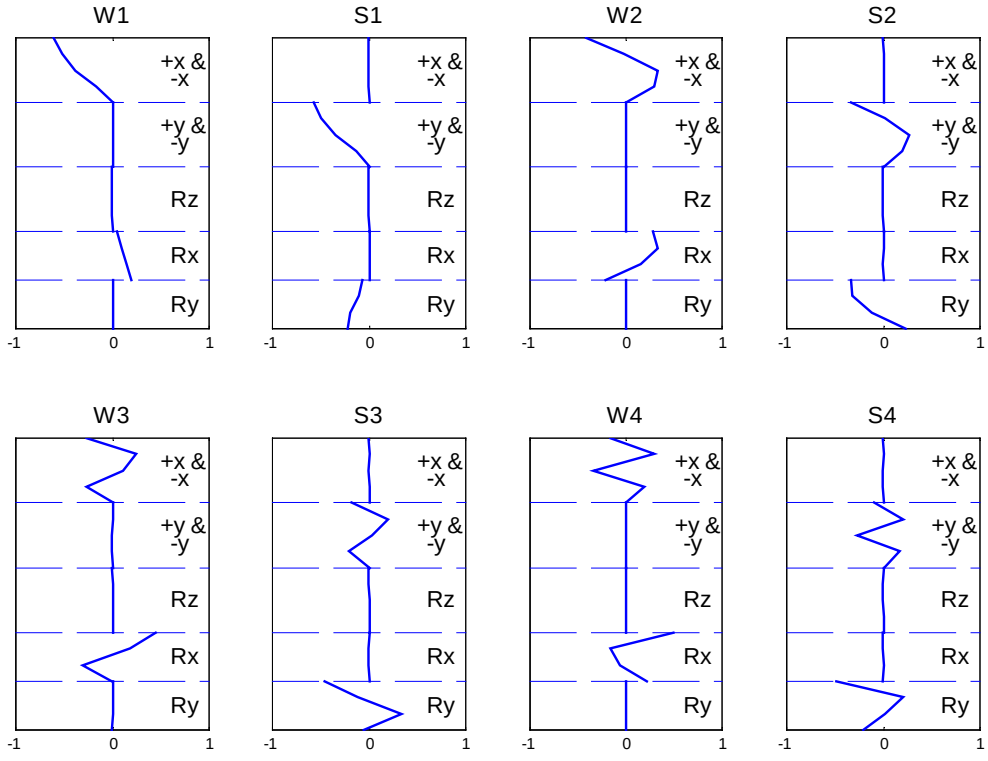

Figure 57. The identified system modeshape for the DP1Uu.fs case.

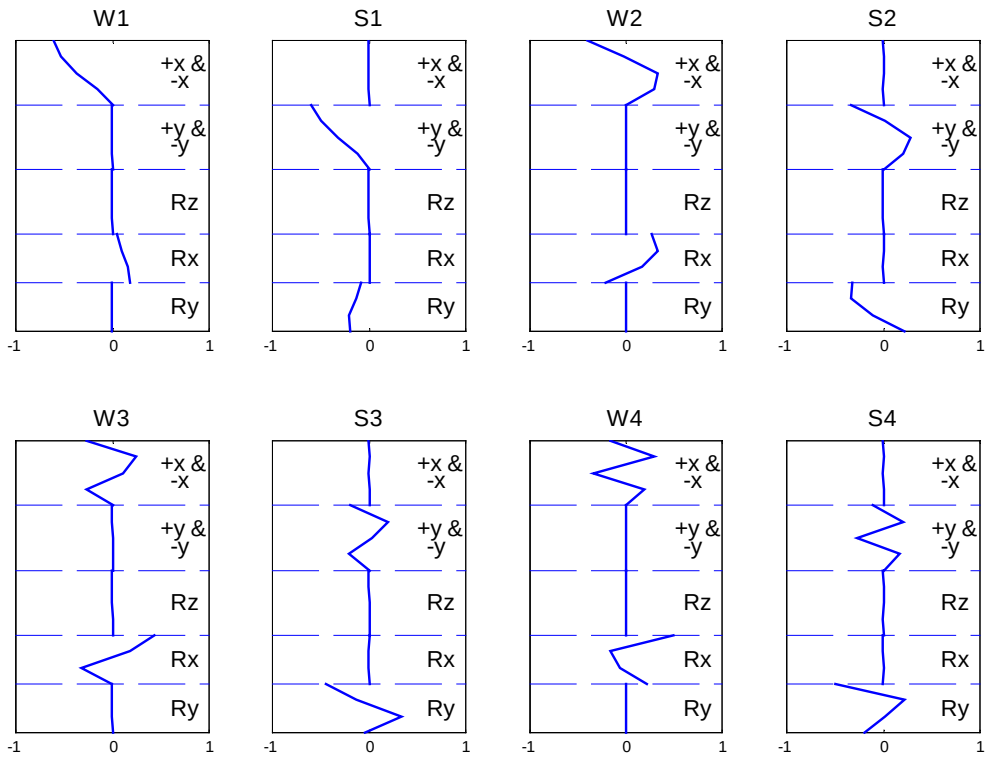

Figure 58. The identified system modeshape for the RU.ps case.

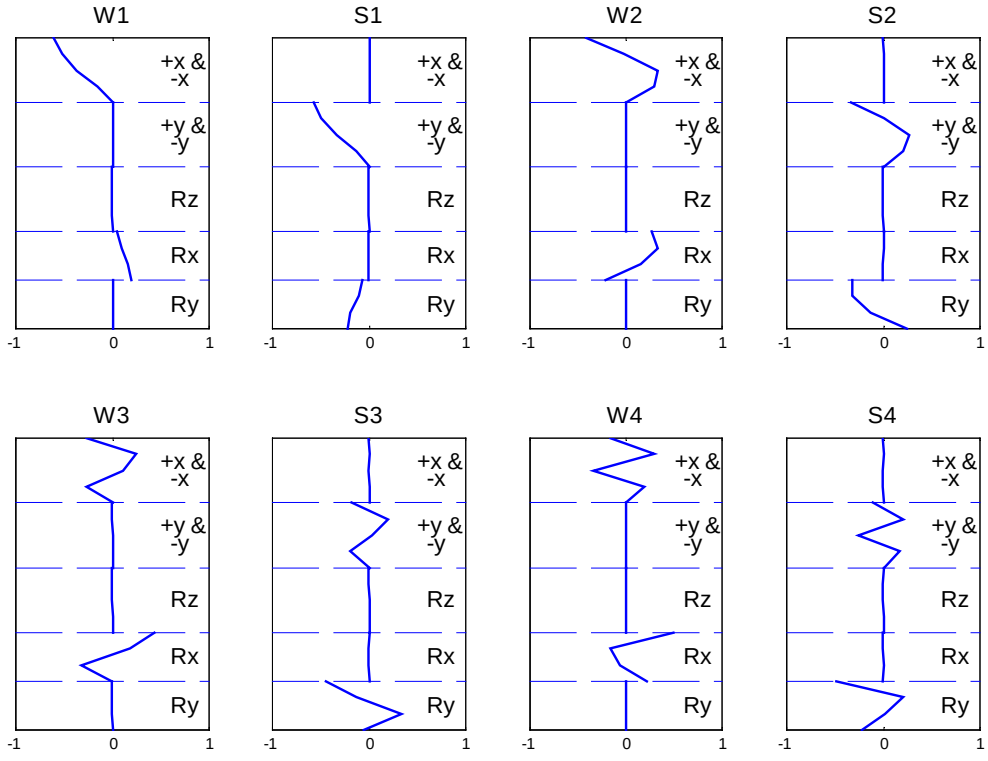

Figure 59. The identified system modeshape for the DP1U.ps case.

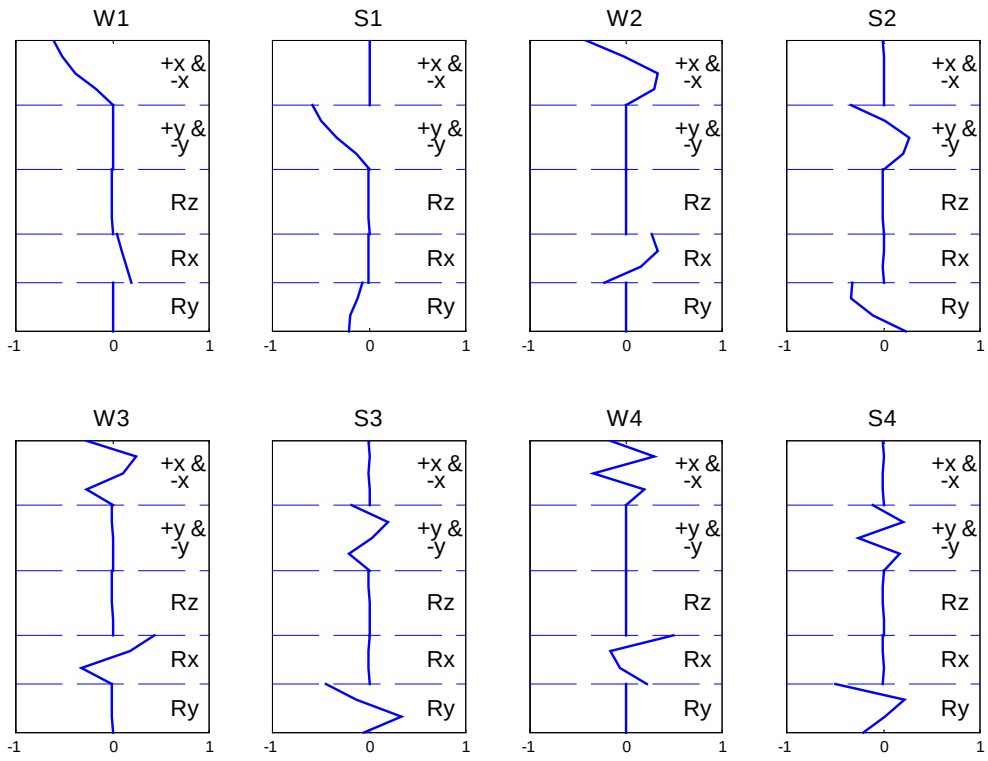

Figure 60. The identified system modeshape for the DP2U.ps case.

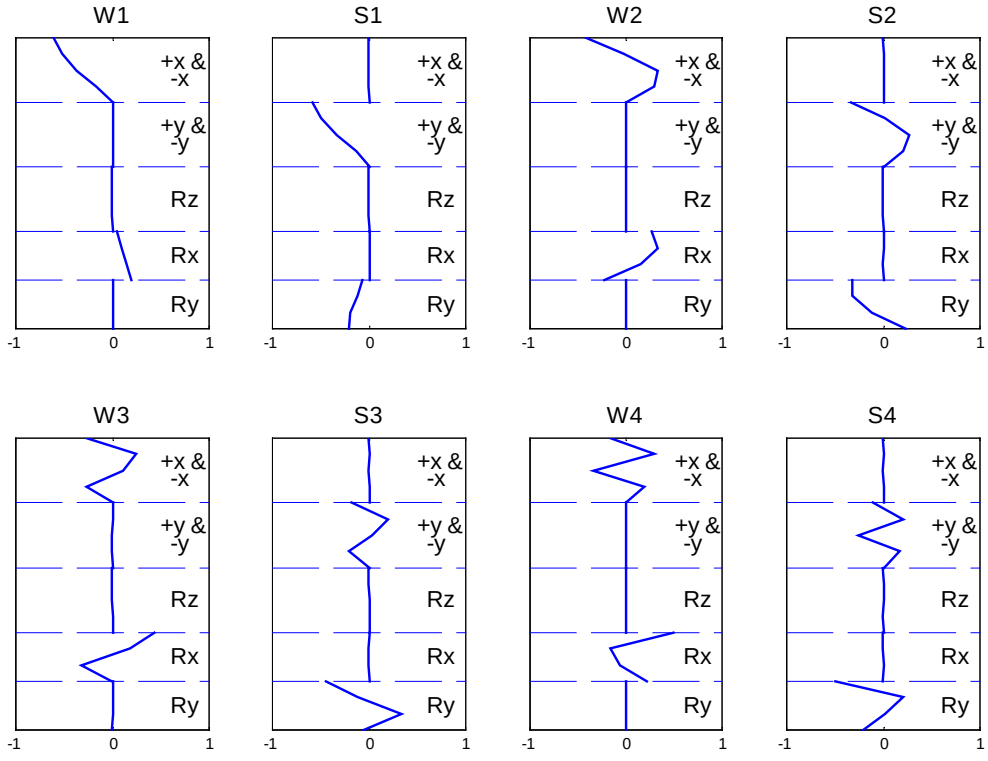

Figure 61. The identified system modeshape for the DP1Uu.ps case.

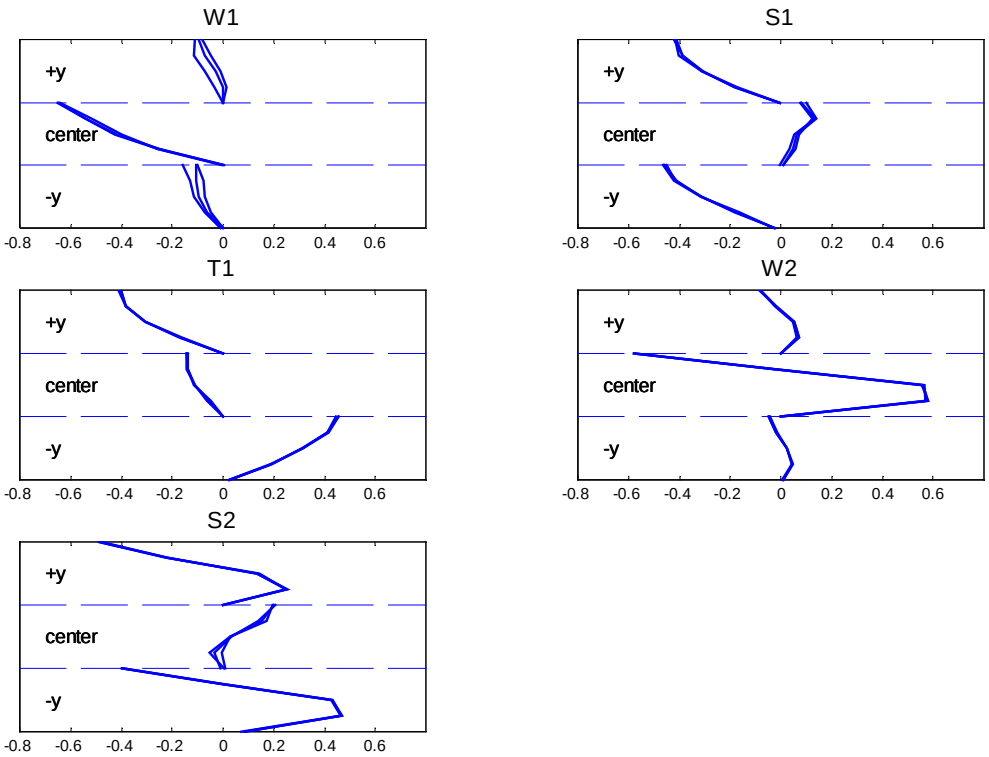

Figure 62. The experimental modeshape components for Config1.h.

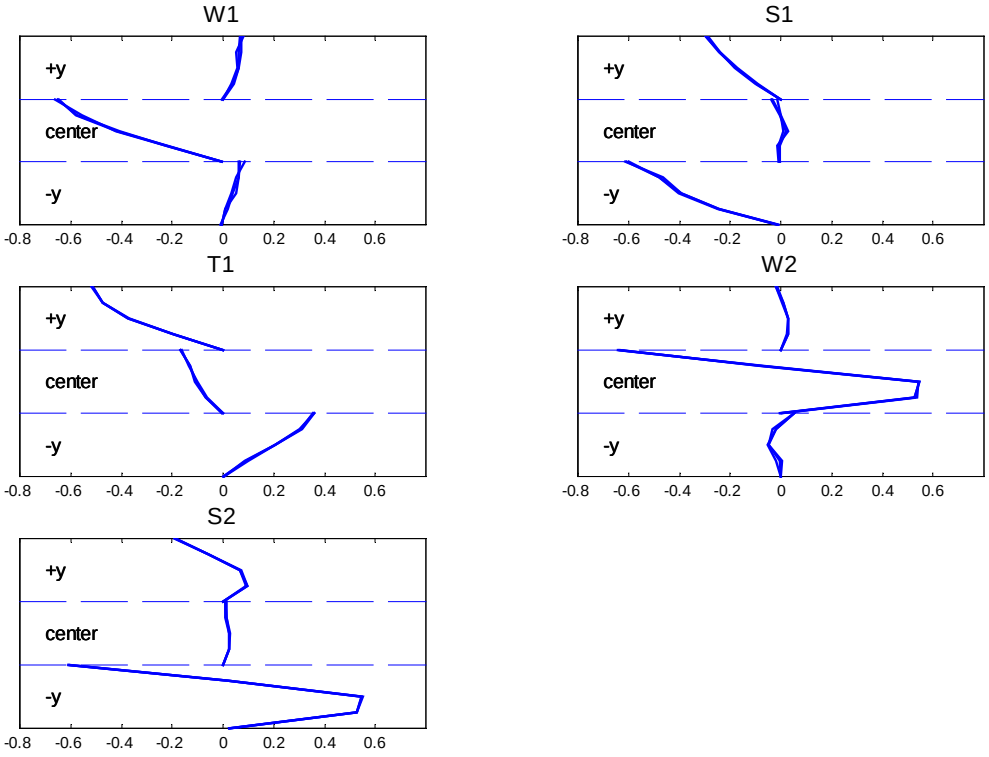

Figure 63. The experimental modeshape components for Config2.h.

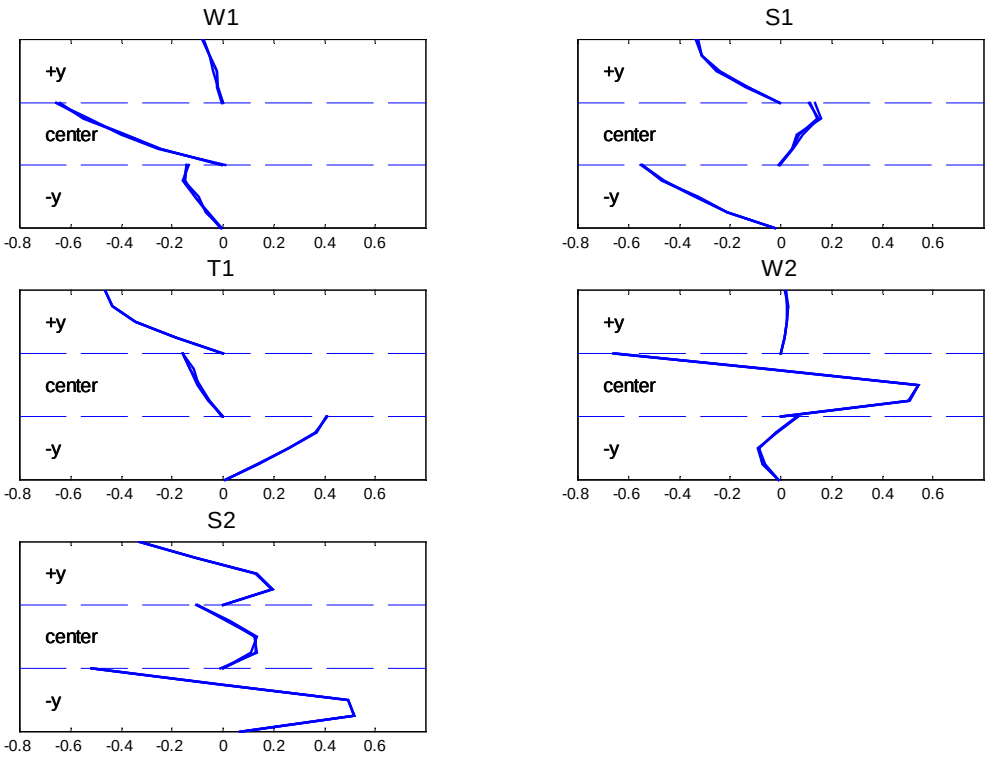

Figure 64. The experimental modeshape components for Config3.h.

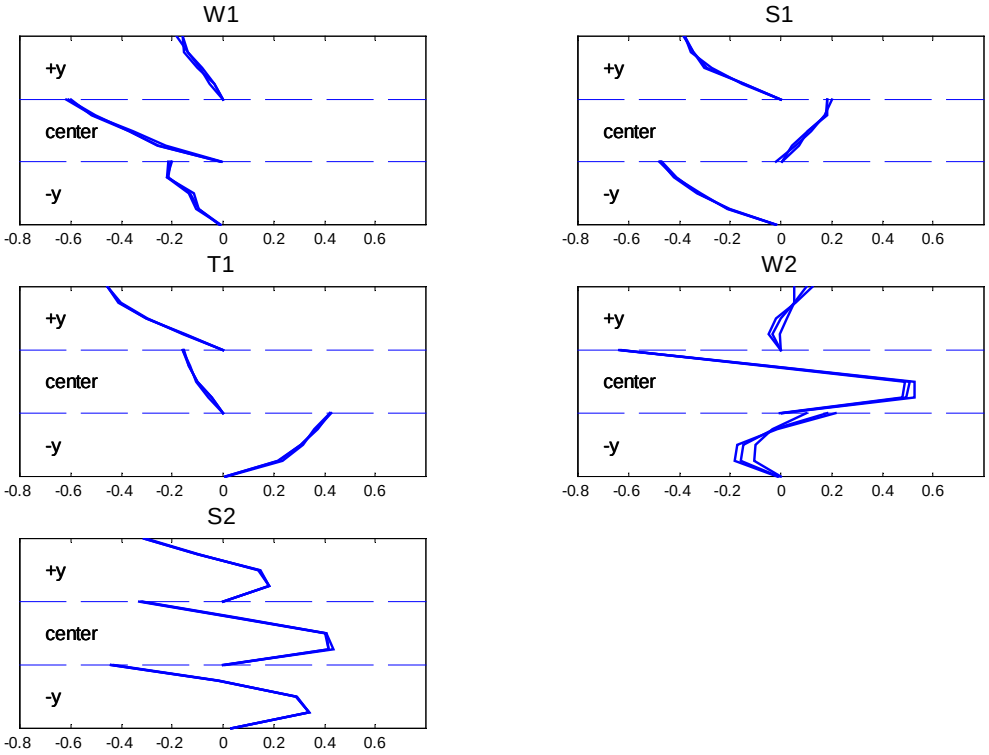

Figure 65. The experimental modeshape components for Config4.h.

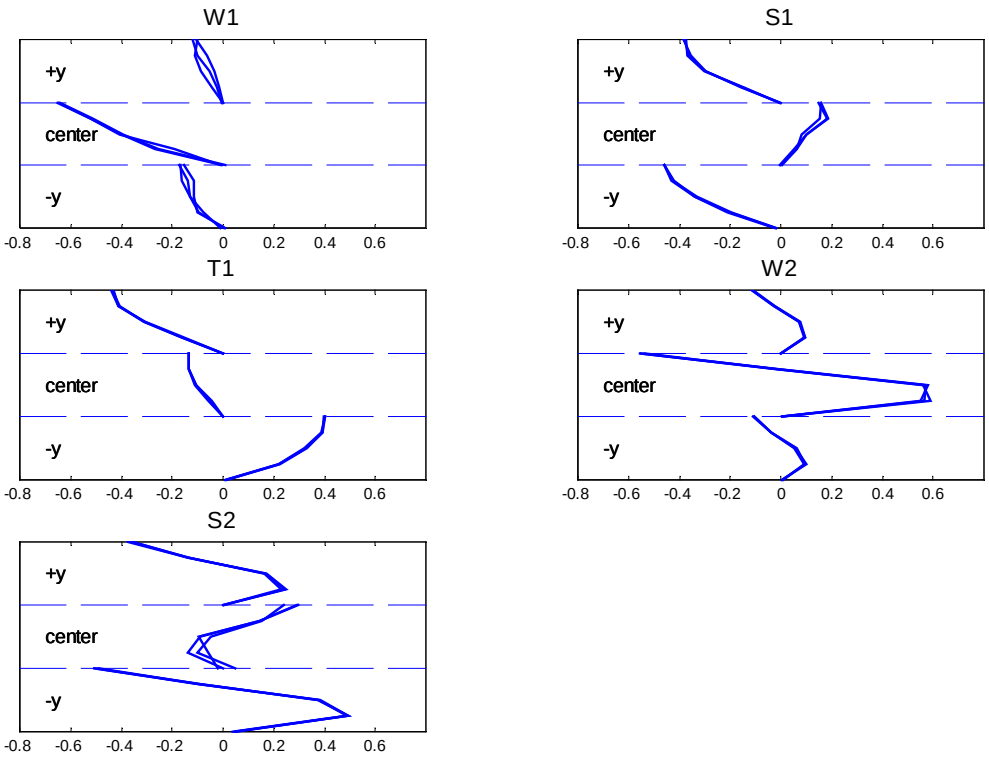

Figure 66. The experimental modeshape components for Config5.h.

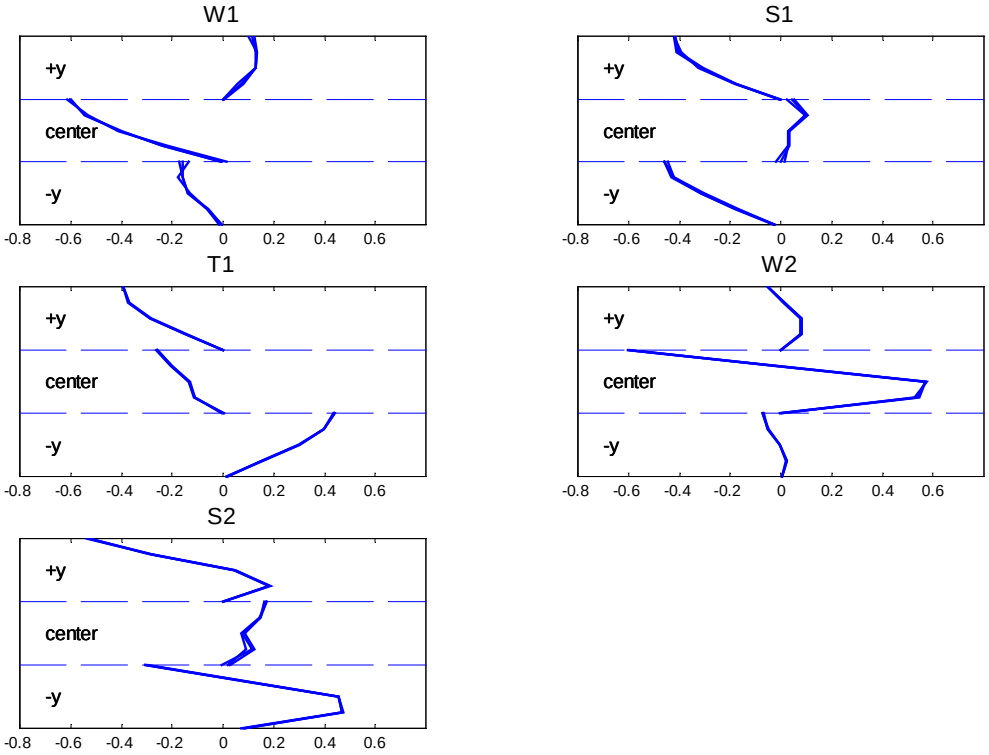

Figure 67. The experimental modeshape components for Config6.h.

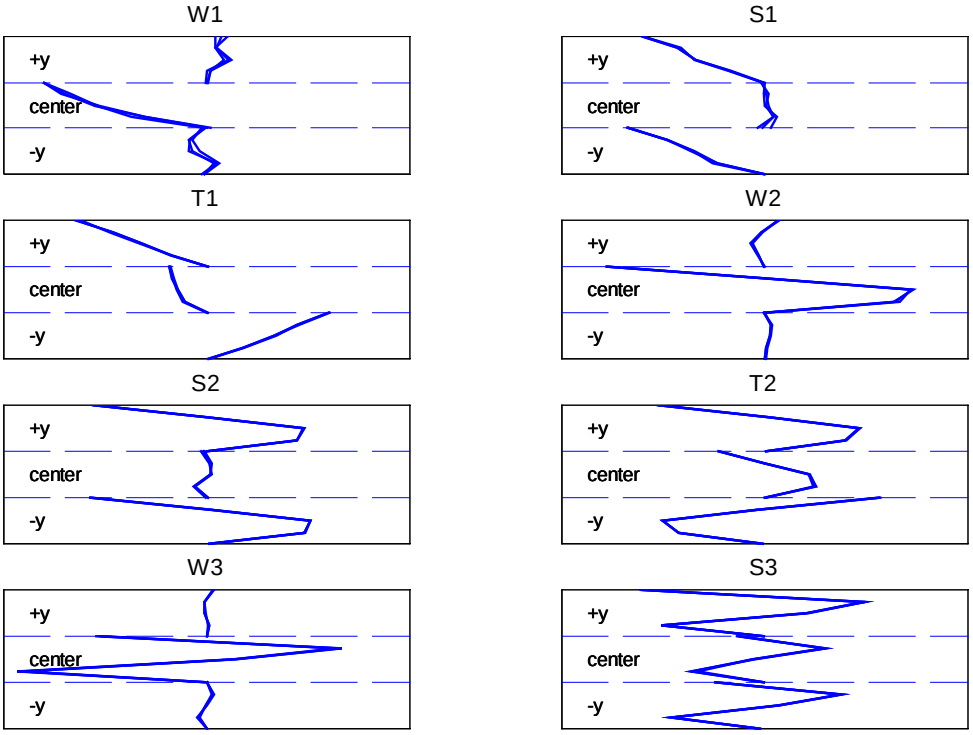

Figure 68. The experimental modeshape components for Config7.h.

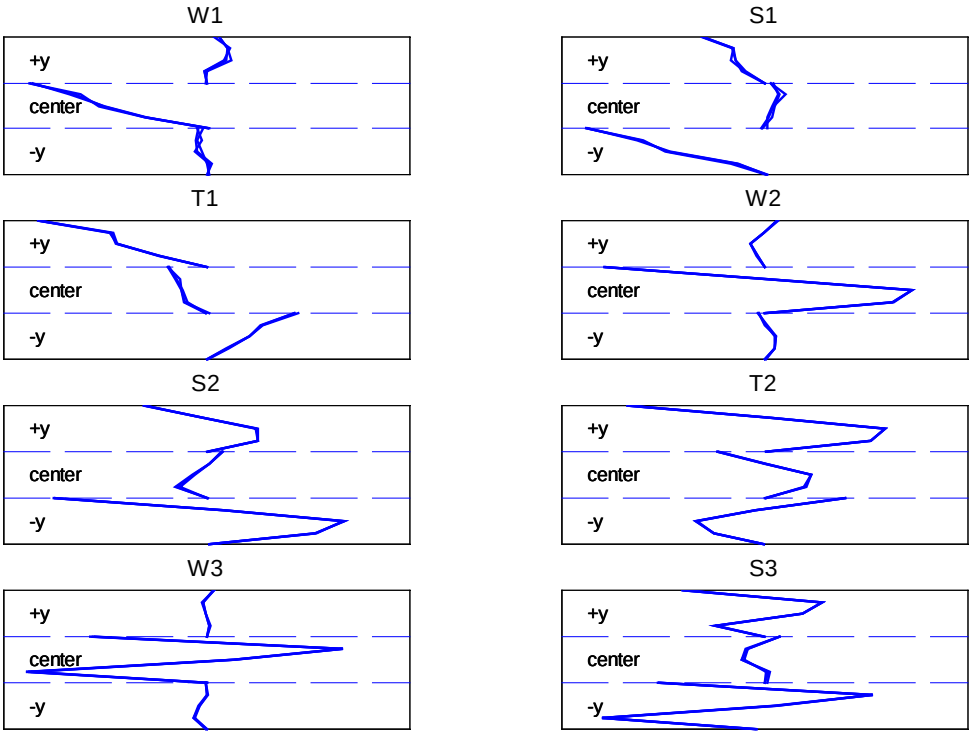

Figure 69. The experimental modeshape components for Config8.h.

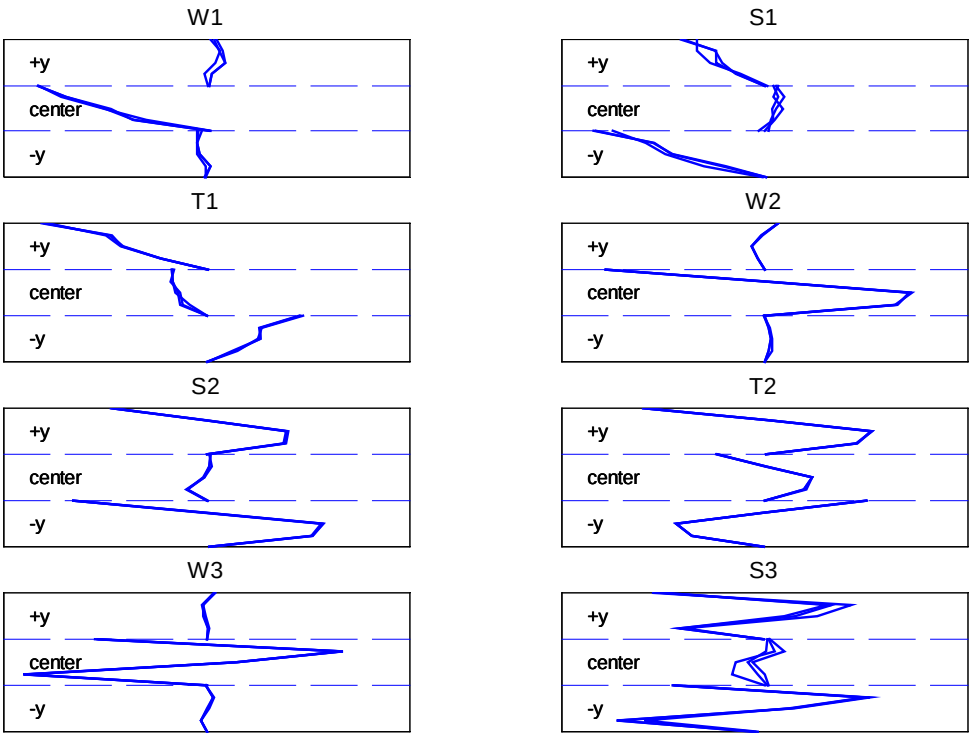

Figure 70. The experimental modeshape components for Config9.h.

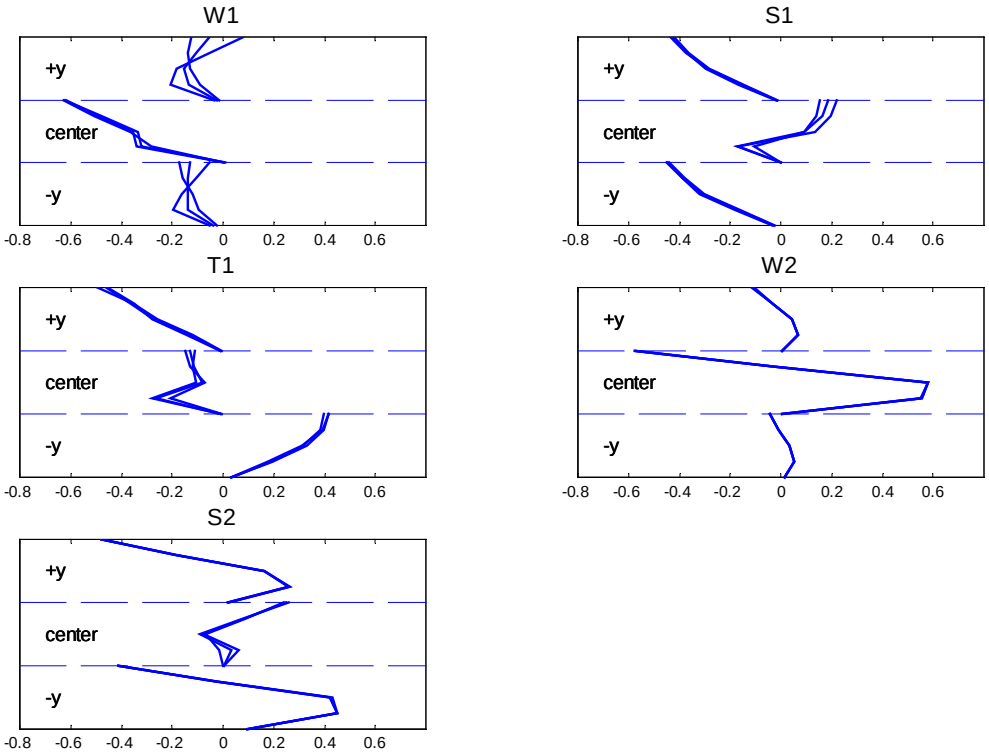

Figure 71. The experimental modeshape components for Config1.a.

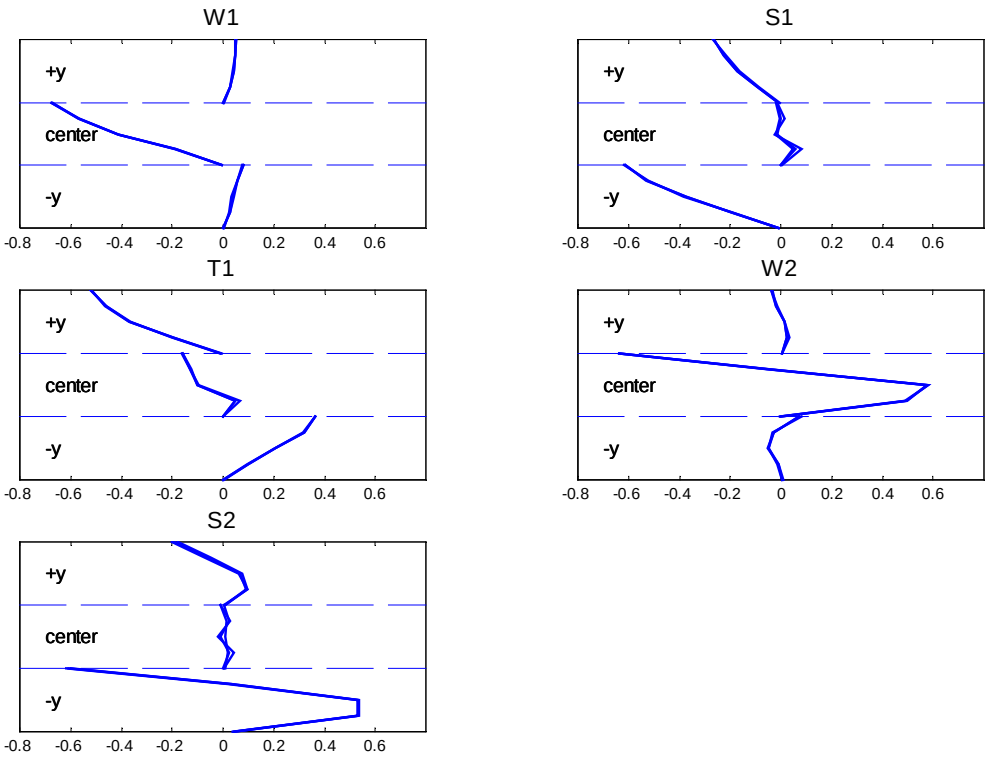

Figure 72. The experimental modeshape components for Config2.a.

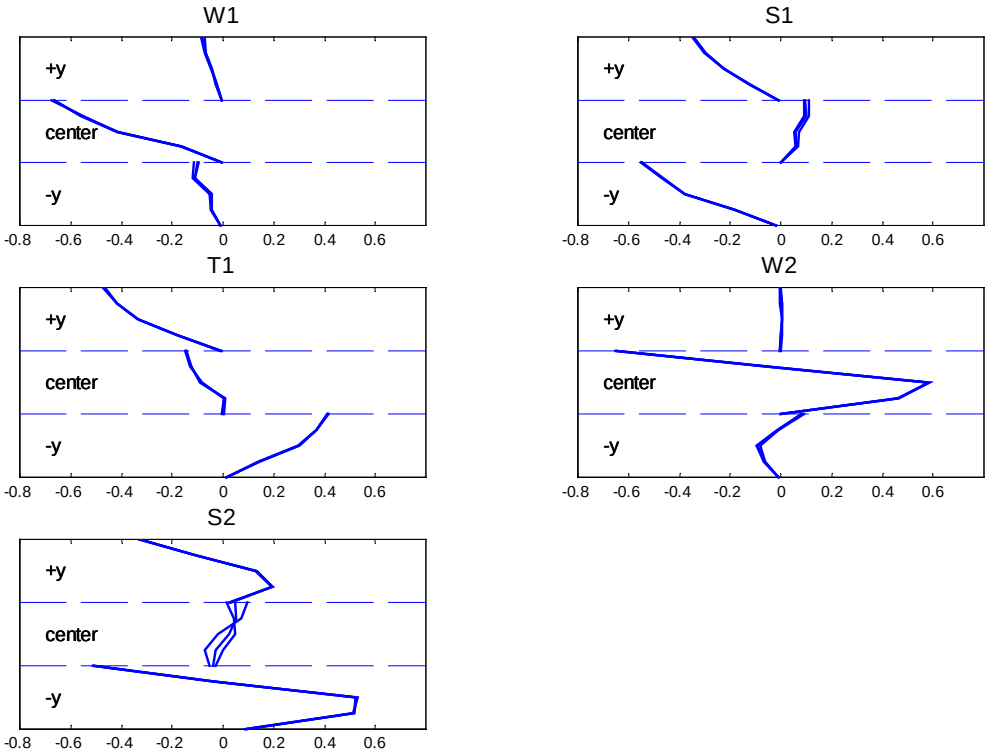

Figure 73. The experimental modeshape components for Config3.a.

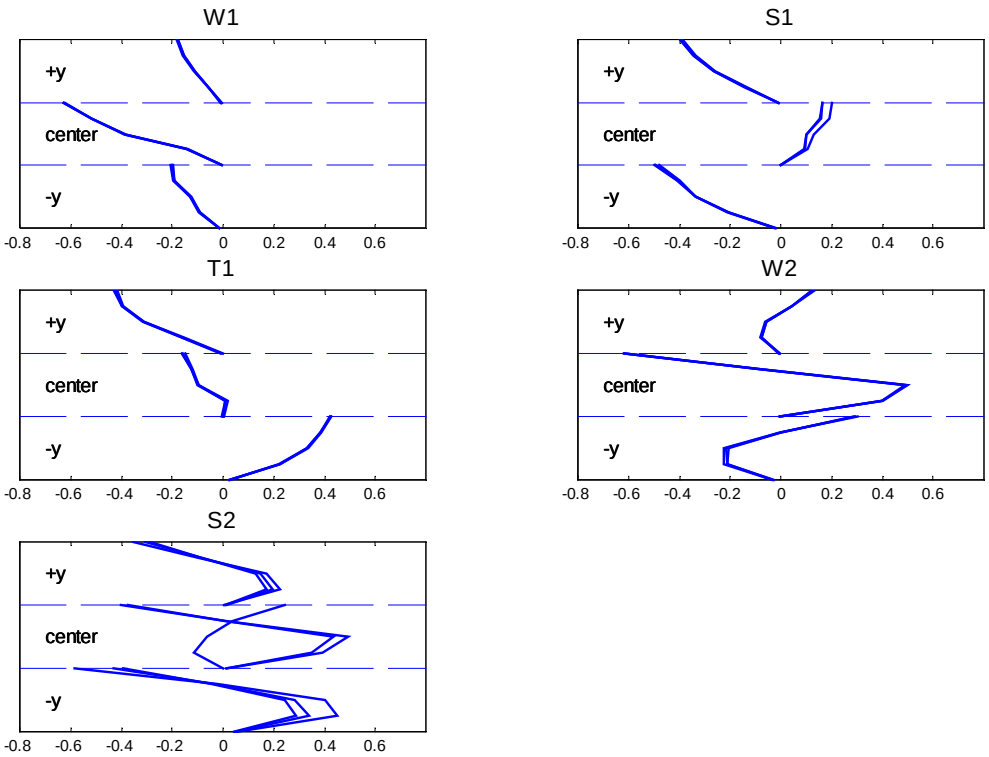

Figure 74. The experimental modeshape components for Config4.a.

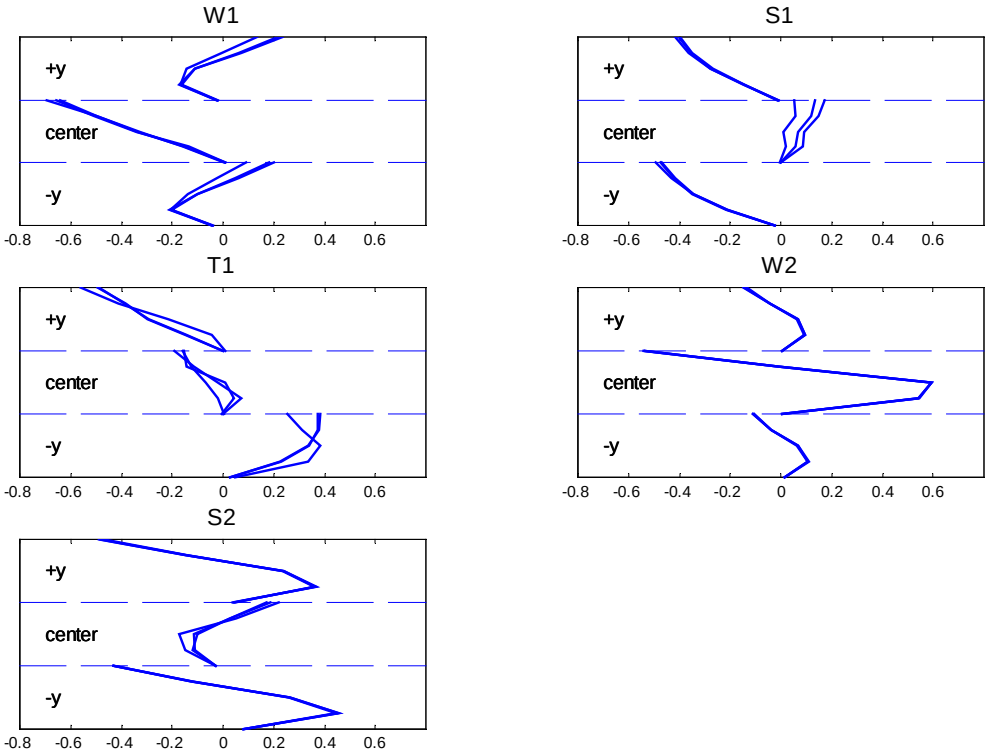

Figure 75. The experimental modeshape components for Config5.a.

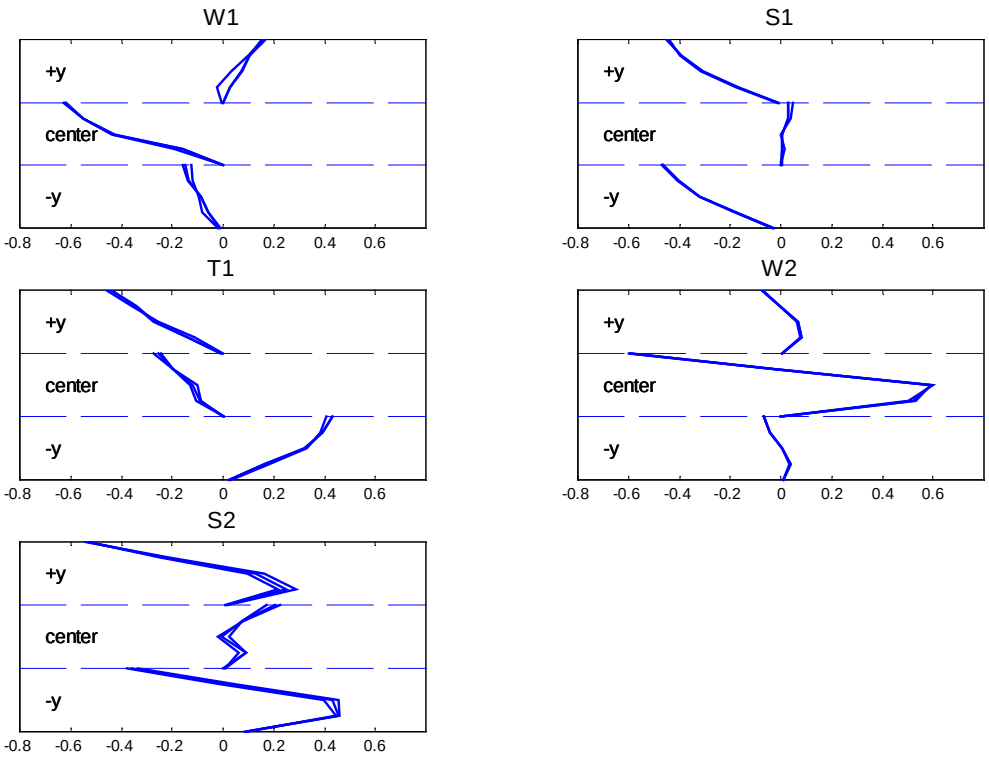

Figure 76. The experimental modeshape components for Config6.a.

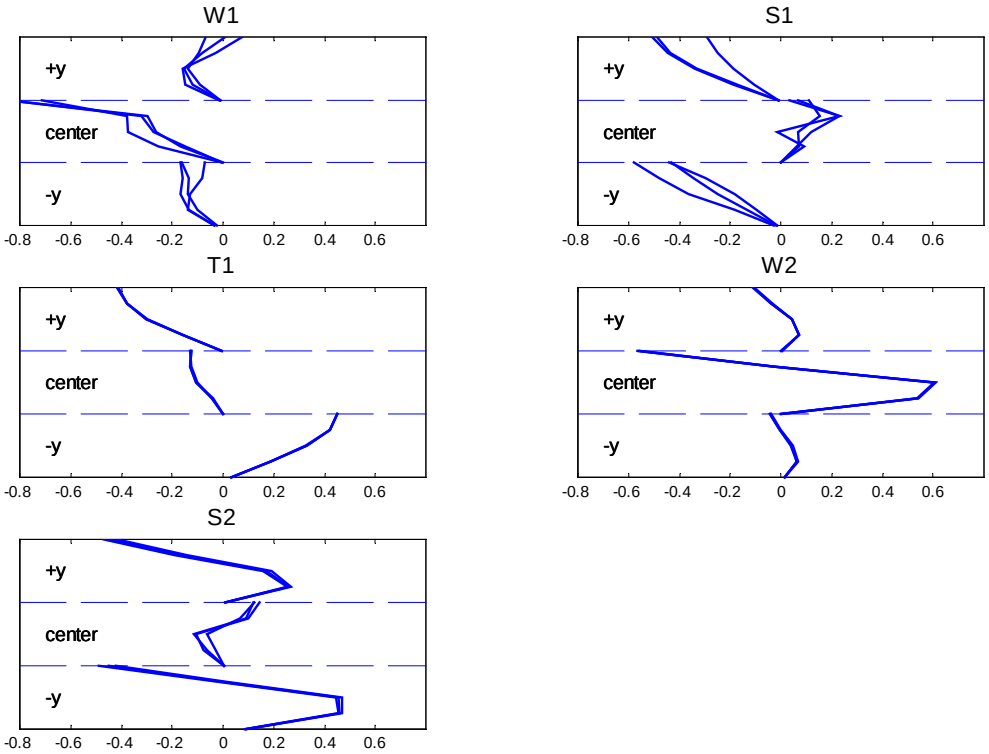

Figure 77. The experimental modeshape components for Config1.s.

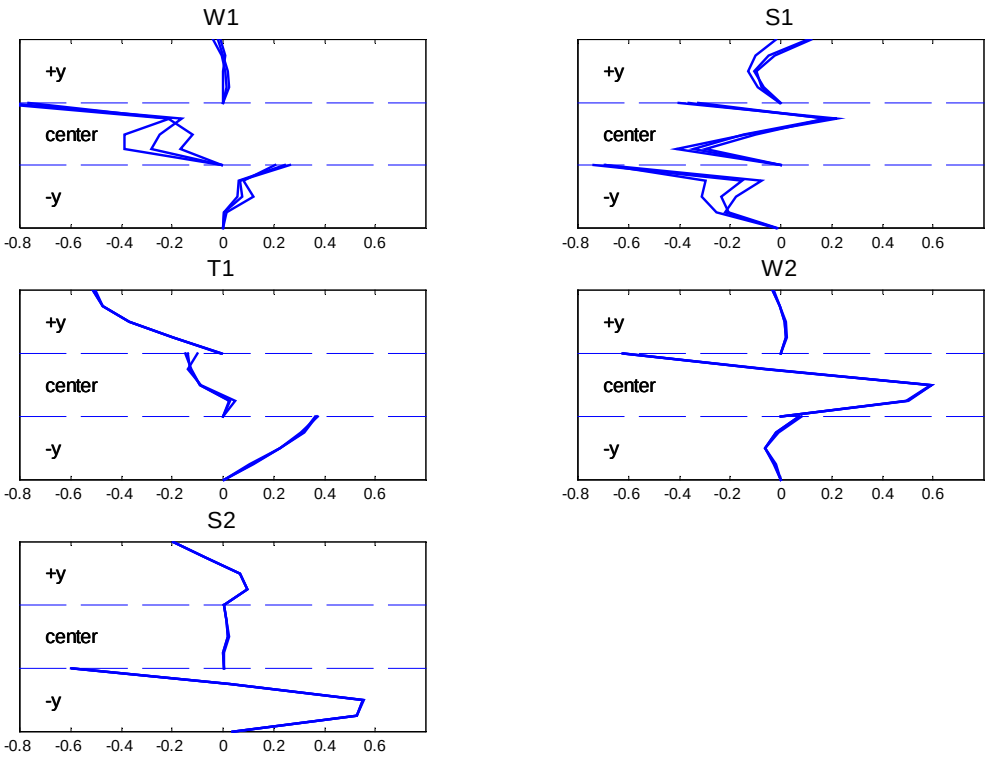

Figure 78. The experimental modeshape components for Config2.s.

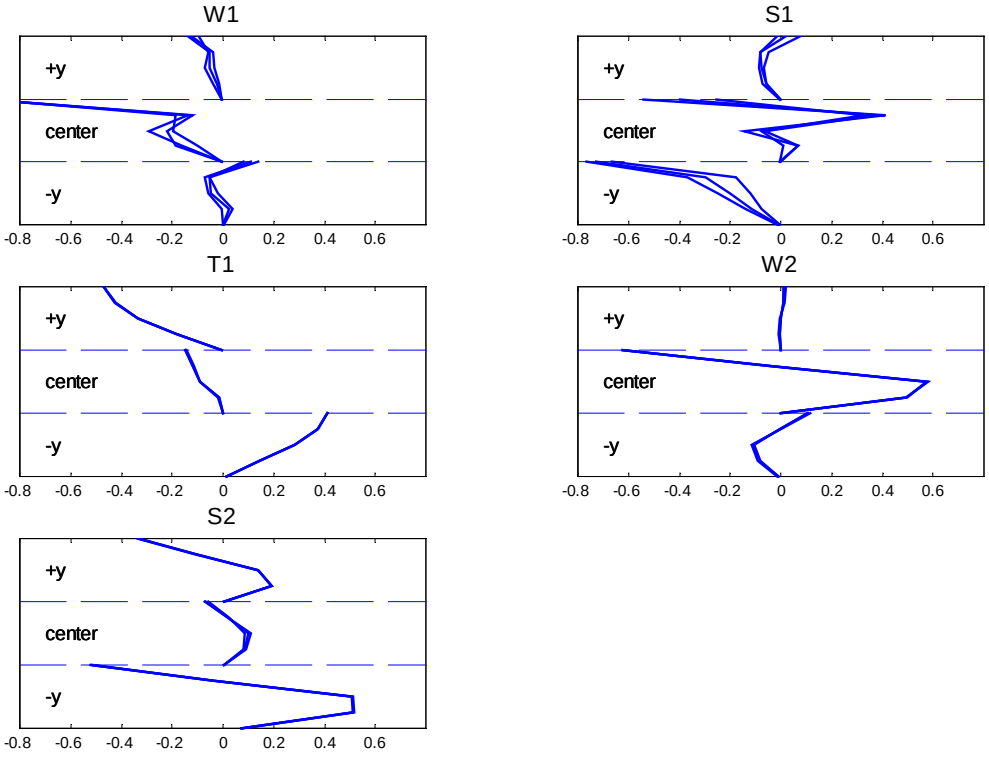

Figure 79. The experimental modeshape components for Config3.s.

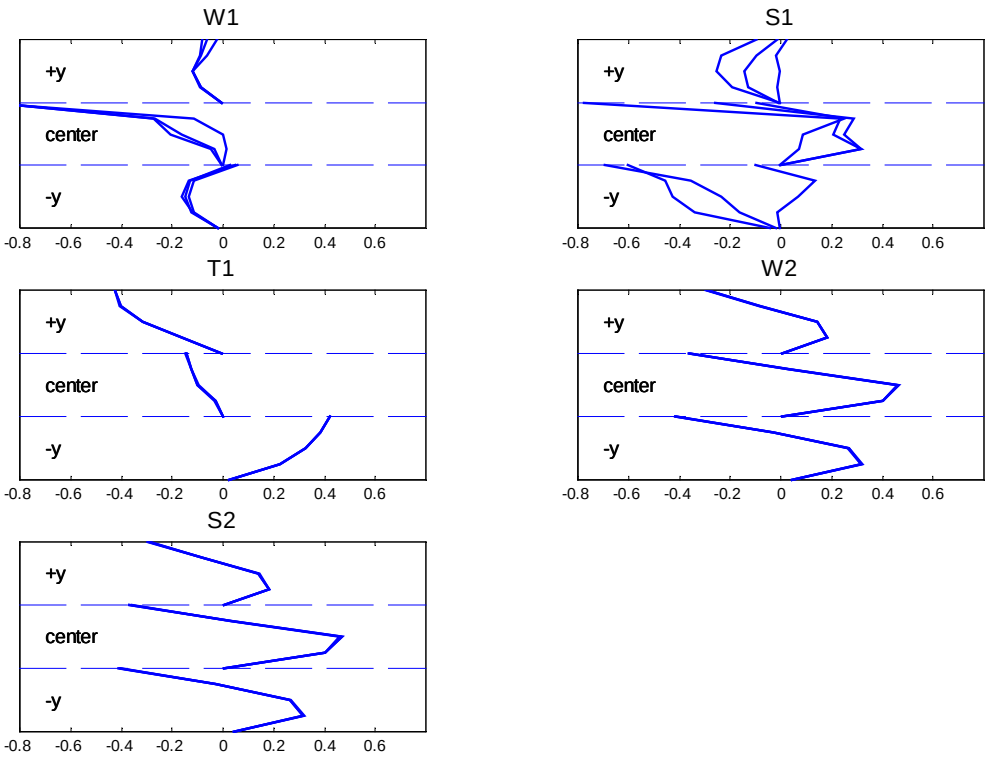

Figure 80. The experimental modeshape components for Config4.s.

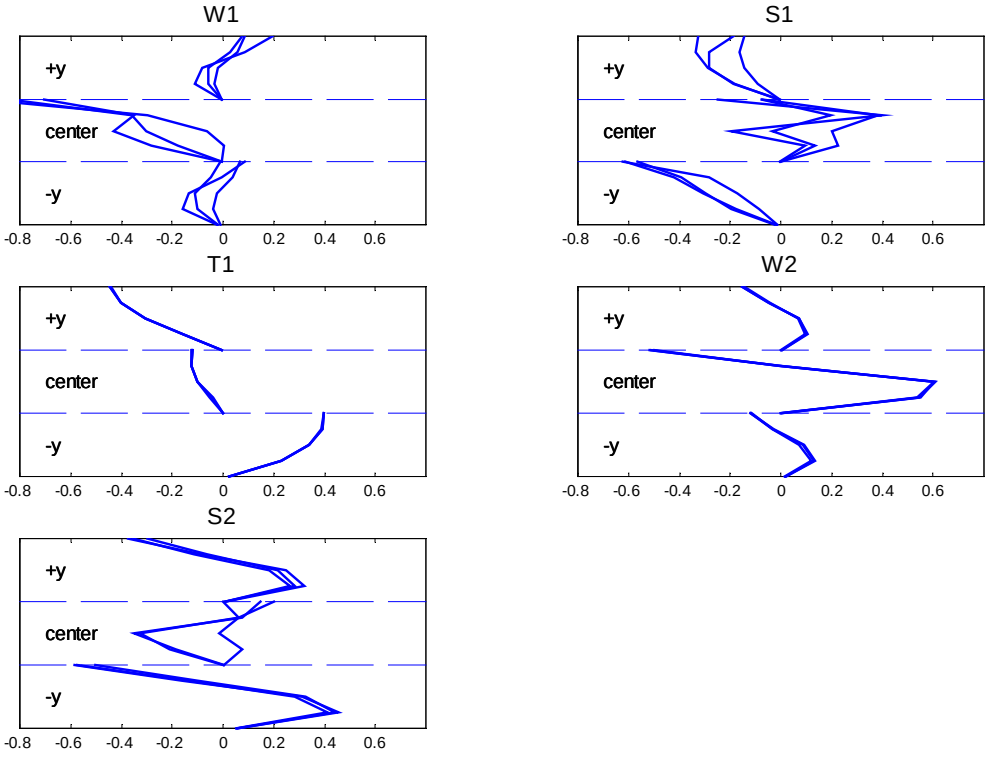

Figure 81. The experimental modeshape components for Config5.s.

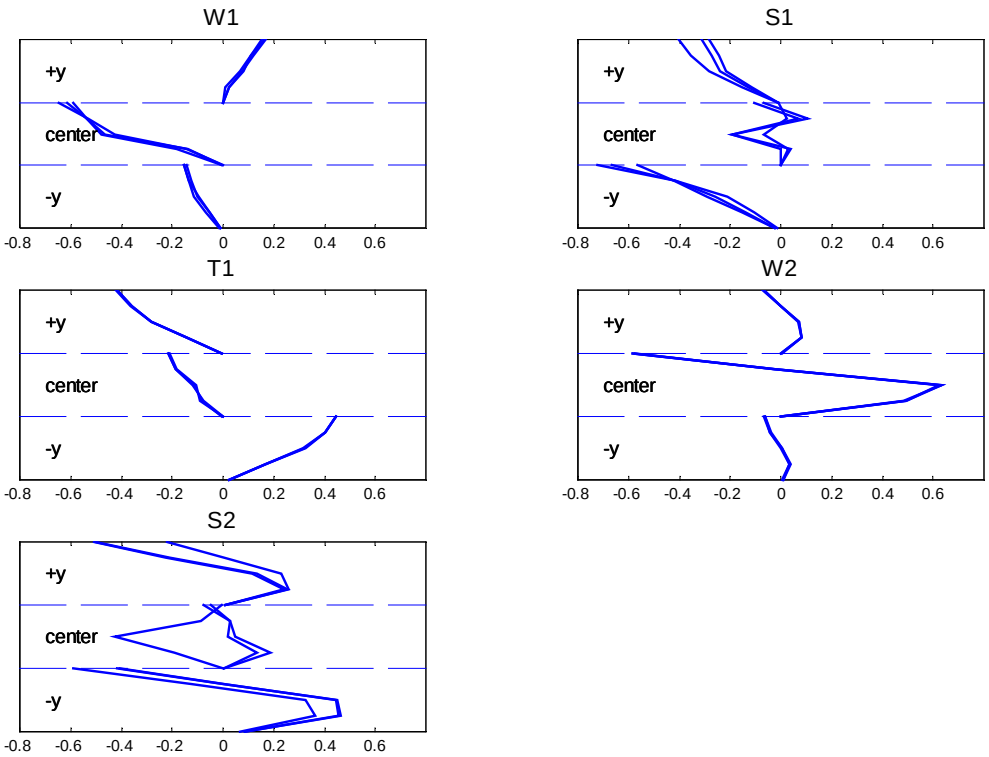

Figure 82. The experimental modeshape components for Config6.s.

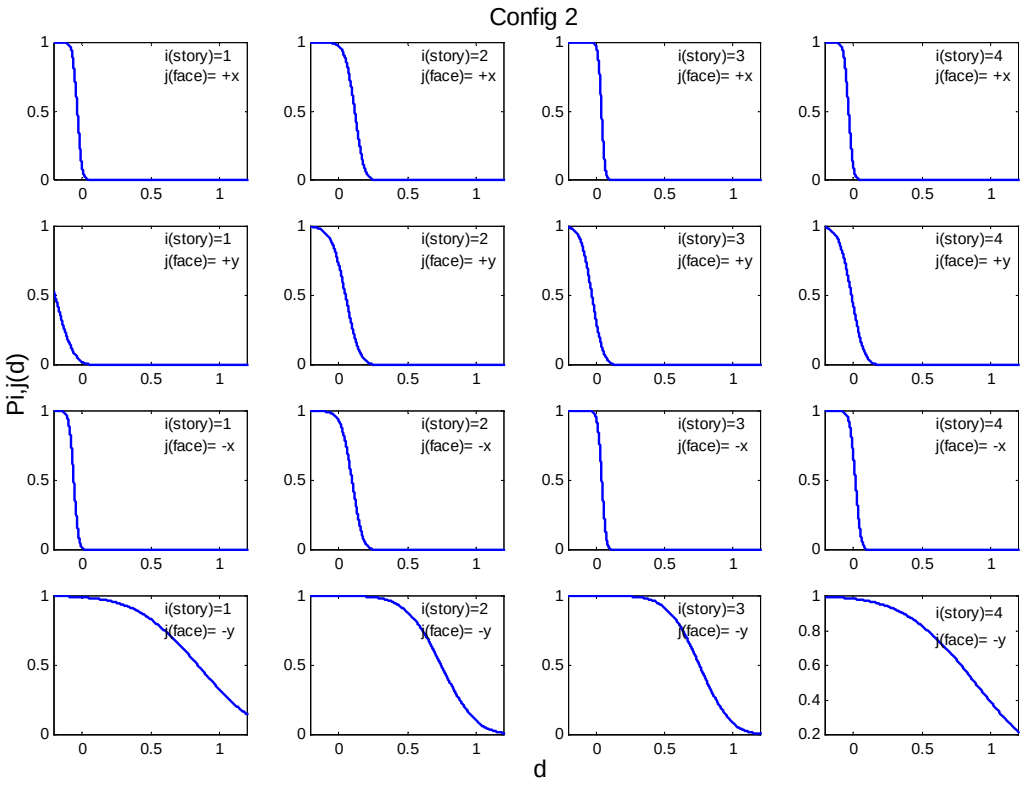

Figure 83. The probability $P_{ij}(d)$ of damage exceeding d in each substructure (Config2.h).

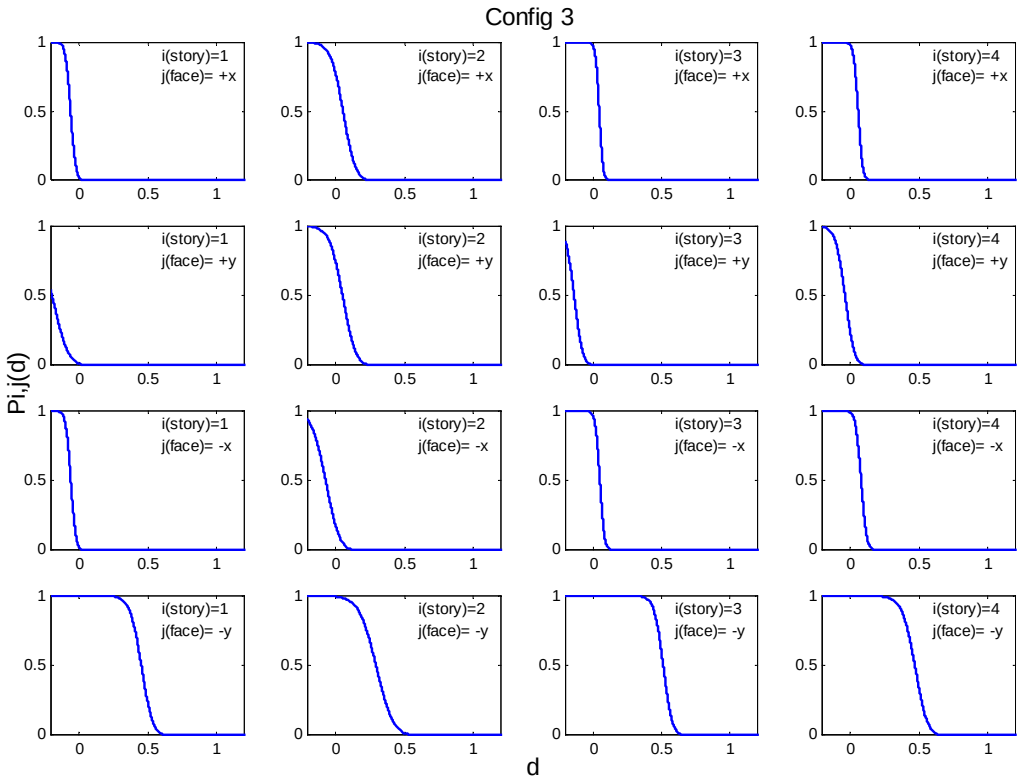

Figure 84. The probability $P_{ij}(d)$ of damage exceeding d in each substructure (Config3.h).

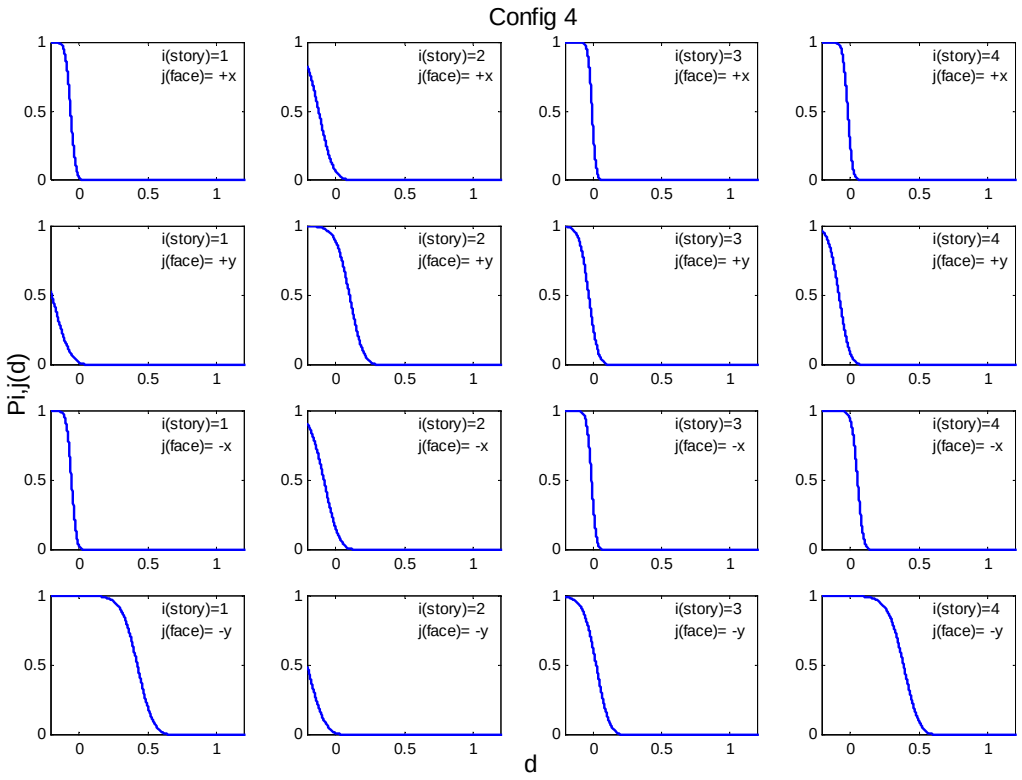

Figure 85. The probability $P_{ij}(d)$ of damage exceeding d in each substructure (Config4.h).

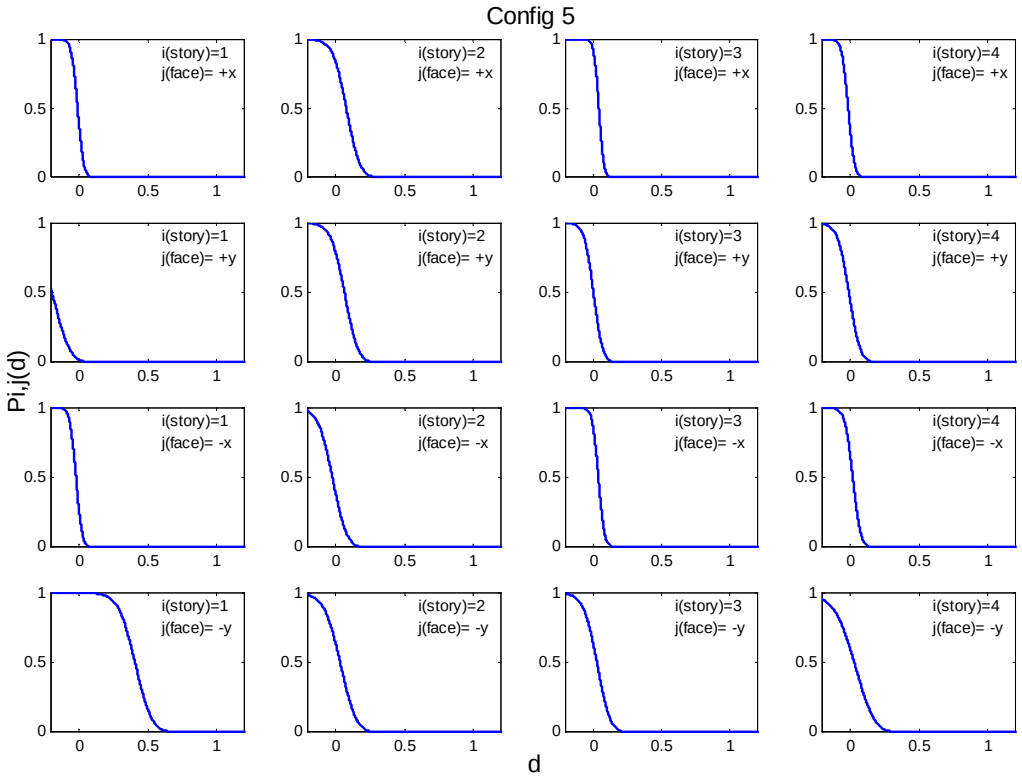

Figure 86. The probability $P_{ij}(d)$ of damage exceeding d in each substructure (Config5.h).

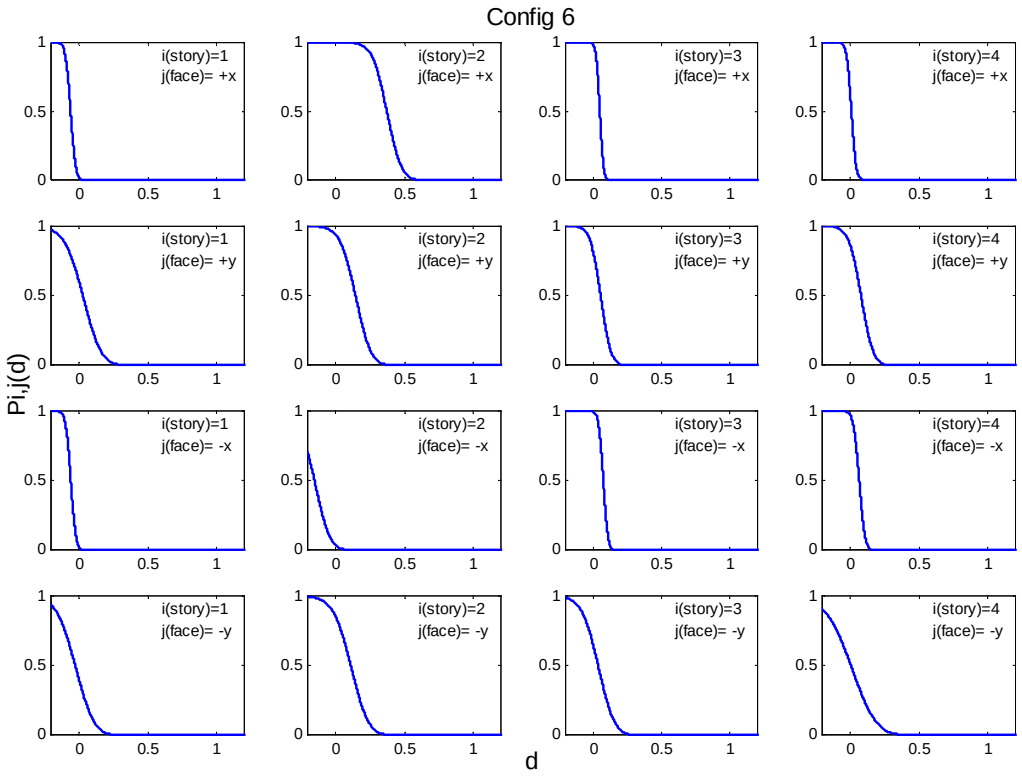

Figure 87. The probability $P_{ij}(d)$ of damage exceeding d in each substructure (Config6.h).

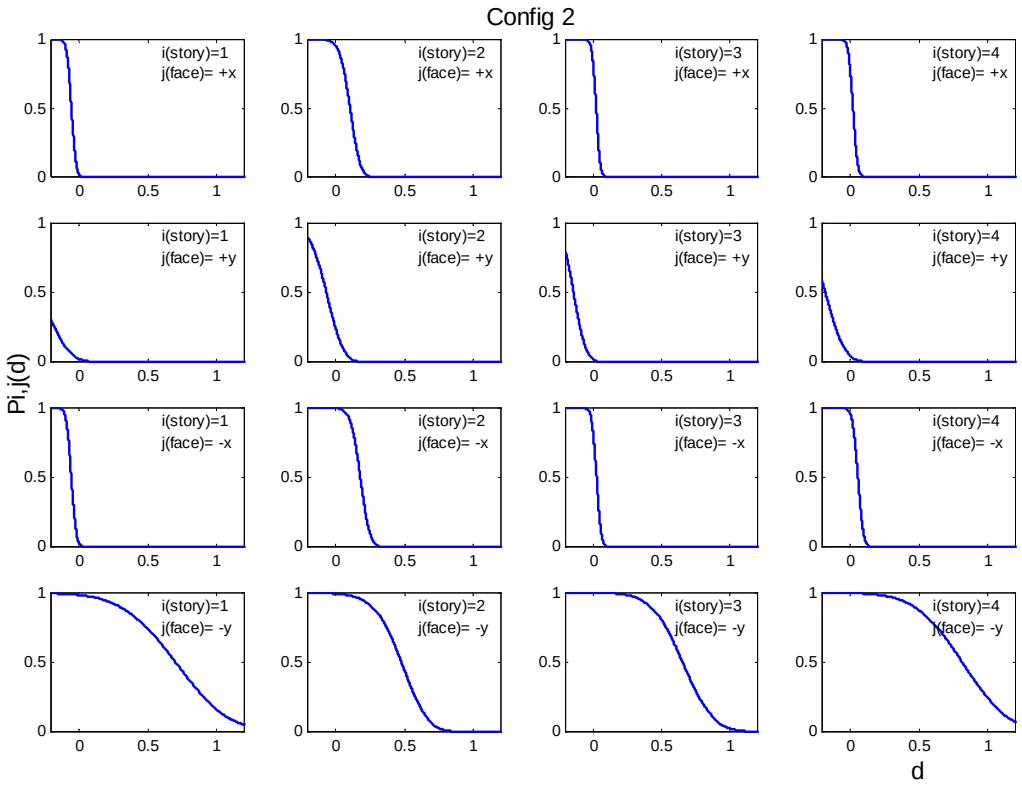

Figure 88. The probability $P_{ij}(d)$ of damage exceeding d in each substructure (Config2.a).

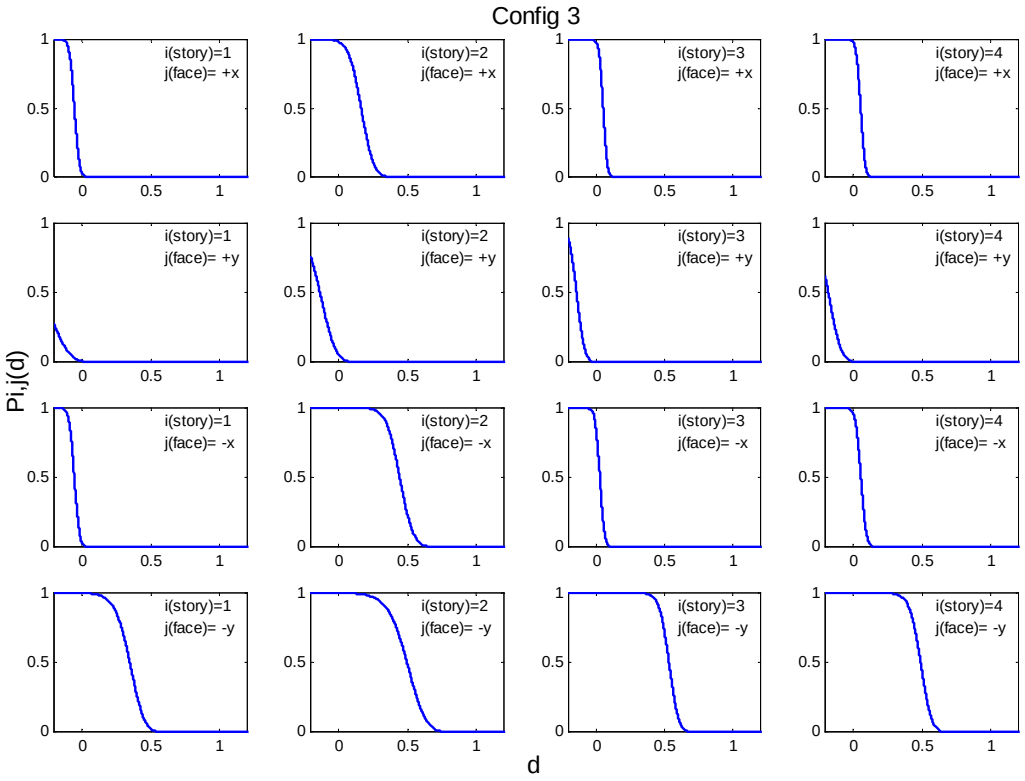

Figure 89. The probability $P_{ij}(d)$ of damage exceeding d in each substructure (Config3.a).

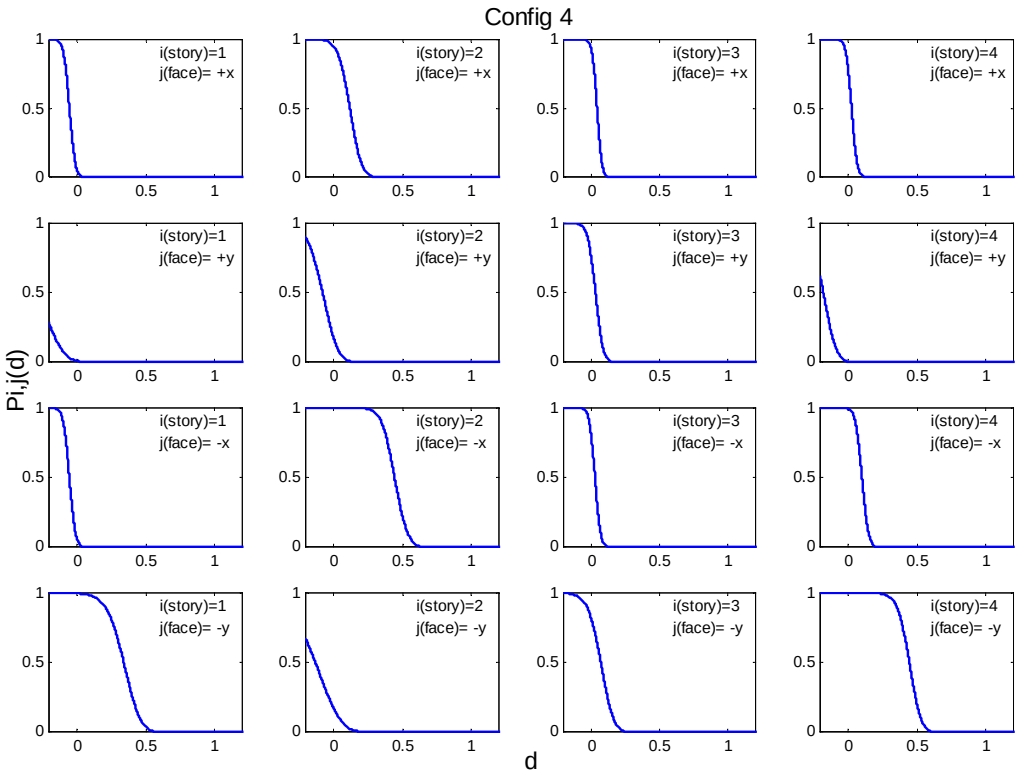

Figure 90. The probability $P_{ij}(d)$ of damage exceeding d in each substructure (Config4.a).

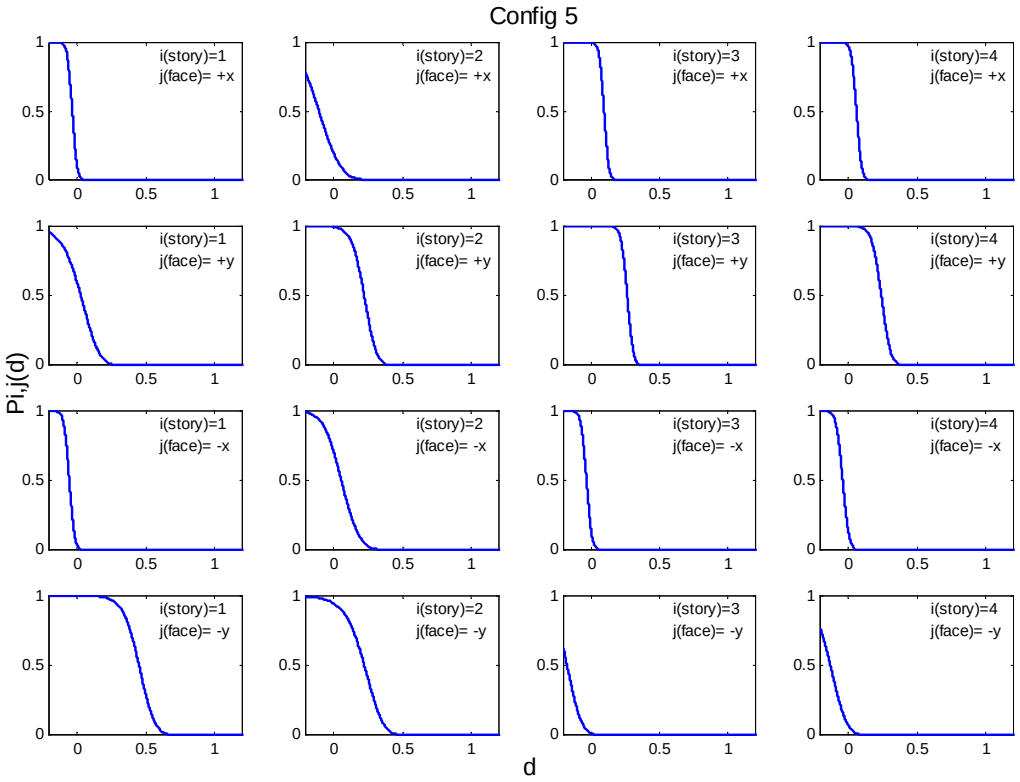

Figure 91. The probability $P_{ij}(d)$ of damage exceeding d in each substructure (Config5.a).

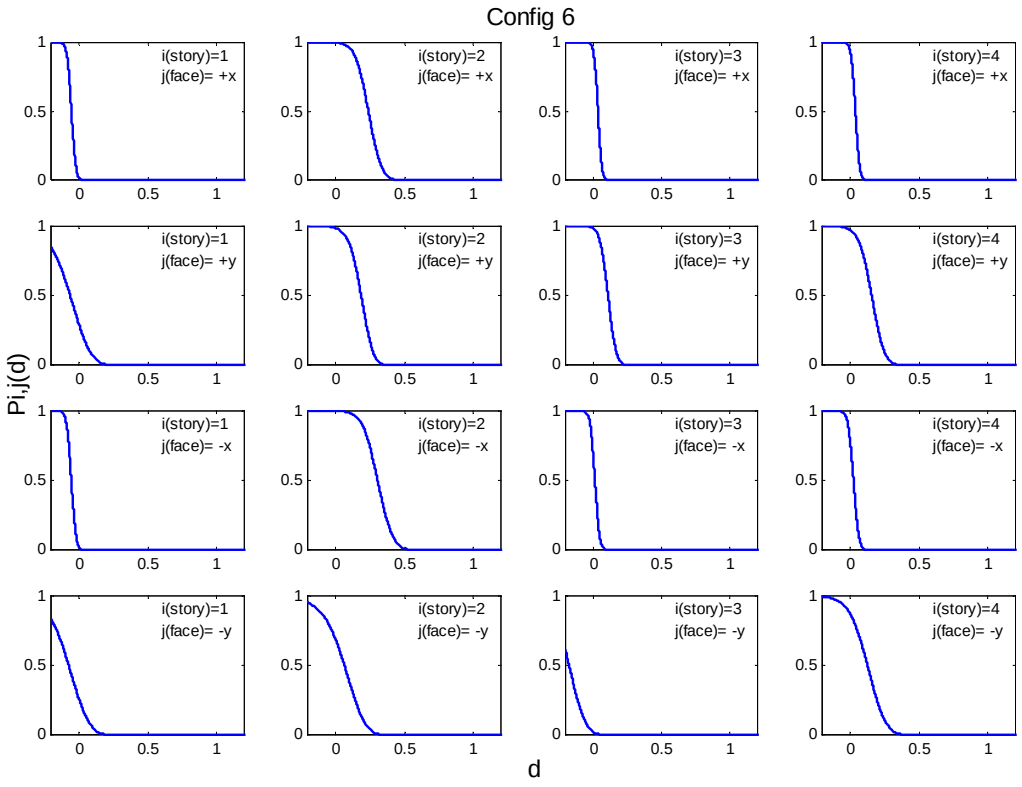

Figure 92. The probability $P_{ij}(d)$ of damage exceeding d in each substructure (Config6.a).